NASA TECHNICAL
MEMORANDUM

NASA TM X-1960

NASA TM X-1960

JET EFFECTS ON THE BOATTAIL AXIAL FORCE OF CONICAL AFTERBODIES AT SUBSONIC AND TRANSONIC SPEEDS

by William B. Compton III and Jack F. Runckel
Langley Research Center
Langley Station, Hampton, Va.

NATIONAL AERONAUTICS AND SPACE ADMINISTRATION • WASHINGTON, D. C. • FEBRUARY 1970

ERRATA

NASA Technical Memorandum X-1960

JET EFFECTS ON THE BOATTAIL AXIAL FORCE OF CONICAL AFTERBODIES AT SUBSONIC AND TRANSONIC SPEEDS

By William B. Compton III and Jack F. Runckel
February 1970

Page 71, figure 15(b): The $C_{A,\beta}$ scale for $l/d_m = 1.0$ (top plot) should be shifted so that the zero line will fall where the .04 line is indicated; that is, the range of the scale should be from -.04 to .16.

1. Report No.
NASA TM X-1960

2. Government Accession No.

3. Recipient's Catalog No.

4. Title and Subtitle
JET EFFECTS ON THE BOATTAIL AXIAL FORCE OF CONICAL AFTERBODIES AT SUBSONIC AND TRANSONIC SPEEDS

5. Report Date
February 1970

6. Performing Organization Code

7. Author(s)
William B. Compton III and Jack F. Runckel

8. Performing Organization Report No
L-6730

9. Performing Organization Name and Address
NASA Langley Research Center
Hampton, Va. 23365

10. Work Unit No.
720-03-11-02-23

11. Contract or Grant No.

12. Sponsoring Agency Name and Address
National Aeronautics and Space Administration
Washington, D.C. 20546

13. Type of Report and Period Covered
Technical Memorandum

14. Sponsoring Agency Code

15. Supplementary Notes

16. Abstract

A parametric investigation has been conducted to determine the jet effects on the boattail axial force of nozzles having truncated conical afterbodies. The boattail axial force for nozzle configurations having boattail angles of 3^{0}, 5^{0}, 10^{0}, and 15^{0} and having ratios of boattail length to maximum diameter of 1.0, 0.8, and 0.6 was compared for the jet-off condition and for a wide range of jet pressure ratios. A nozzle configuration with a boattail angle of 7.5^{0}, one with a boattail angle of 20^{0}, and one with a circular-arc boattail were tested also. The tests were run at an angle of attack of 0^{0} and through a Mach number range of 0.30 to 1.30.

17. Key Words Suggested by Author(s)

Jet interference
Boattail
Axial force
Drag
Conical afterbodies
Convergent-divergent nozzles
Subsonic speeds
Transonic speeds

18. Distribution Statement
Unclassified – Unlimited

19. Security Classif. (of this report)
Unclassified

20. Security Classif. (of this page)
Unclassified

21. No. of Pages
108

22. Price*
$3.00

*For sale by the Clearinghouse for Federal Scientific and Technical Information
Springfield, Virginia 22151

JET EFFECTS ON THE BOATTAIL AXIAL FORCE OF CONICAL AFTERBODIES AT SUBSONIC AND TRANSONIC SPEEDS

By William B. Compton III and Jack F. Runckel
Langley Research Center

SUMMARY

A parametric investigation has been conducted to determine the jet effects on the boattail axial force of nozzles having truncated conical afterbodies. The boattail axial force for nozzle configurations having boattail angles of 3°, 5°, 10°, and 15° and having ratios of boattail length to maximum diameter of 1.0, 0.8, and 0.6 was compared for the jet-off condition and for a wide range of jet pressure ratios. The different nozzle configurations represented various positions of three variable-flap convergent-divergent nozzles of different lengths. A nozzle configuration with a boattail angle of 7.5°, one with a boattail angle of 20°, and one with a circular-arc boattail were tested also. The tests were run at an angle of attack of 0° and through a Mach number range of 0.30 to 1.30. Reynolds number based on model length was in the range of 8×10^6 to 16×10^6 depending on the Mach number.

Results indicate that, in general, boattail axial force continually declined with increasing jet pressure ratio above an exit-pressure ratio of 1.0. For the same jet exit-pressure ratio, or equal jet pluming, the configurations with the larger boattail angles generally received more favorable jet interference, compared with the jet-off conditions, than those with the smaller boattail angles. With the jet operating, shortening the boattail length at conditions in which the boattail pressures have recovered to greater than free-stream value can cause a decrease in axial force.

INTRODUCTION

Aircraft which have operational capabilities at subsonic, transonic, and supersonic speeds require variable-geometry exhaust nozzles for which both the internal-expansion ratio and the external boattail angle must change with Mach number and altitude for optimum performance (ref. 1). The wide range of external geometric variations that is possible with engines proposed for multimission aircraft have made prediction of the nozzle boattail drag difficult. Many of the available prediction methods are based on theoretical or experimental models which do not account for flow exhausting from the boattail base. For supersonic speeds, theoretical calculations of boattail drag have been used for axisymmetric boattailed afterbodies with cylindrical forebodies (for example, refs. 2 to 6). Experimental results at supersonic speeds on conical boattails are presented in references 4 and 7. In the subsonic and transonic speed range, however, experimental data have been the basic source of information (ref. 8, for example). Recently some progress in theoretical analysis at subsonic speeds has been accomplished by using potential-flow theory and by accounting for compressibility and viscous effects (ref. 9). This analysis, however, has not been applied to conical boattails with sharp corners and does not include jet interference effects.

Unless the jet interference effects on boattail pressures can be predicted, the jet-off pressure drag of conical boattails in external flow is of little value in determining exhaust-nozzle thrust-minus-boattail-drag performance. These effects can be large, particularly at subsonic speeds with the jet operating underexpanded. Examples of jet effects on conical-boattail drag are given in references 10 to 19. One of the few attempts to provide data for a systematic variation in conical-boattail geometric parameters, with jet interference effects included, is reported in reference 12. This information, however, has limited application for current conical-boattail exhaust nozzles because (1) a sonic jet at the exit of the boattail was used and (2) models with large bases and generally much larger boattail angles than those proposed for current aircraft engine nozzles were investigated.

The present investigation was conducted in the Langley 16-foot transonic tunnel to provide parametric information on the variable-flap-type convergent-divergent nozzle. The primary variables selected were conical-boattail angle and length of the variable external flap. A nacelle model with a 15.24-cm diameter was tested with a series of fixed conical-boattail convergent-divergent nozzles using airflow for jet simulation. Data were obtained over a wide range of jet pressure ratio in order to operate each fixed nozzle in both overexpanded and underexpanded conditions. The model configurations were investigated at Mach numbers ranging from 0.30 to 1.30 and at an angle of attack of 0°. For the Mach number range and the nozzle expansion ratios of the configurations of the present investigation, the jet interference effects on boattail axial force should be similar to those for air-breathing turbine engines.

Information on a reference nozzle with a circular-arc boattail is given in appendix A.

SYMBOLS

A	area, m^2
C_A	axial-force coefficient, $\frac{F_A}{qA_m}$

C_p	pressure coefficient, $\frac{p_l - p_\infty}{q}$
c	length of convergent section of nozzle (see fig. 4), m
d	diameter, m
F_A	axial force, N
f	axial distance from nozzle throat, positive aft (see fig. 4), m
i,n	integers
L	boattail length in axial direction (see fig. 4), m
l	length of boattail flap parallel to boattail surface (see fig. 4), m
M	free-stream Mach number
M_l	local Mach number
p	pressure, N/m^2
q	free-stream dynamic pressure, N/m^2
R_m	maximum radius of model, m
r	radial distance from center line of model, m
s	spacing between nozzle throat and exit (see fig. 4), m
V_l	local velocity, m/s
V_δ	velocity at edge of boundary layer, m/s
x	axial distance from boattail corner, positive aft (see fig. 4), m
x_n	axial distance from nose of model, m
y	radial distance from model surface, m

α	nozzle divergence half-angle (see fig. 4), deg
β	boattail angle, angle between axis of symmetry and generatrix of model afterbody (see fig. 4), deg
δ	boundary-layer thickness, m
ϵ_e	nozzle internal-expansion ratio, A_e/A_{th}
θ	nozzle convergence half-angle (see fig. 4), deg
ϕ	angular location measured from, and in a plane perpendicular to, axis of symmetry of model, clockwise direction positive when viewed from rear, 0° at top of model (see fig. 4), deg

Subscripts:

a	afterbody
av	average
b	base
bal	balance
des	design
dw	divergent wall
e	exit
f	friction
j	jet
l	local
m	maximum

t	total
th	throat
β	boattail
∞	free stream

APPARATUS AND PROCEDURE

Wind Tunnel

This investigation was conducted in the Langley 16-foot transonic tunnel, which is a single-return, continuous tunnel with an octagonal slotted test section measuring 4.73 meters across the flats. By pumping low-energy air from the plenum which surrounds the slotted test section, a Mach number of 1.3 can be attained. For cooling, the tunnel is equipped with an air-exchange tower which continuously exchanges air with the atmosphere, the result being that the tunnel stagnation pressure is approximately equal to atmospheric pressure.

Model

General.- The basic model to which the different nozzle configurations tested in this investigation were attached was an air-powered cone-cylinder nacelle with a rounded shoulder at the junction of the nose and the cylindrical section (see fig. 1). A continuous flow of dry high-pressure air at a total temperature of approximately 270° K to 300° K was used for the jet exhaust. Boundary-layer transition was fixed at 5.08 cm from the nose of the model by a strip of No. 100 grit approximately 5 mm wide. The model was supported from the tunnel floor by a 5-percent-thick strut swept back with respect to the model and having a leading-edge sweep of 45°.

The details of the model including the air introduction and balance arrangements are shown in figure 2 in which the portion of the model supported by the balance is indicated by fine hatching and dots, and in which the path of the air is indicated by arrows. The air is introduced perpendicularly to the model axis into the section of the model supported by the balance through eight sonic nozzles equally spaced radially around a center core. The eight radial nozzles are not supported by the balance; therefore, the balance measures the true thrust due to the acceleration of the air rearward. Two flexible metal bellows, arranged so that one is ahead and one is behind their respective points of attachment to the fixed portion of the model, seal the forward portion of the air chamber, an arrangement which prevents the pressurizing of the bellows from loading the balance.

The flow-smoothing screens were made of 0.635-mesh 0.0635-cm-diameter wire cloth backed by four support vanes. The total pressure and temperature behind the screens were measured by single pressure and temperature probes to minimize flow distortion. The measurement of average total pressure by using only one probe was found to be acceptable by rake surveys which indicated that the total-pressure profile in this region was essentially flat for all the sizes of nozzles used in this investigation.

Nozzle configurations.- The different configurations tested in this investigation were intended to simulate various positions of each of three variable-flap convergent-divergent nozzles. The configuration series was formulated by assuming that a variable-flap convergent-divergent nozzle having a ratio of basic flap length to maximum diameter of 1.0 would have a 0° boattail at a design jet total-pressure ratio of 34. Configuration external geometry was varied only aft of axial station 104.14, the location of the theoretical hinge point for the nozzle flaps. The selected fixed boattail angles β were 0°, 3°, 5°, 10°, and 15° for each of the three nozzles having respective ratios of flap length to maximum nacelle diameter of 1.0, 0.8, and 0.6. The extent of the boattail geometric variations is indicated graphically in figure 3 in which the symbols represent the configurations investigated. Three other nozzles, one with a boattail angle of 7.5°, one with a boattail angle of 20°, and one with a ratio of boattail length to maximum diameter of 0.638, are also indicated in the figure. The top portion of the figure shows the variation of the ratio of base diameter to maximum diameter with boattail angle whereas the bottom portion represents the variation of boattail fineness ratio L/d_m with the ratio of base area to maximum area. The corner insert sketch illustrates how the boattail angle varies for a flap hinge point which is located at station 104.14.

A sketch of a typical variable-flap nozzle configuration is presented in figure 4 and pertinent geometric parameters are listed for all test configurations along with the configuration numbers. At the theoretical hinge point of the nozzle flaps, all nozzles had a cross-sectional area of 182.4 cm^2. The junction of the cylindrical section and the boattail was machined as a sharp corner and was at the same station for all the variable-flap nozzle configurations. In keeping with the variable-flap design, the difference between the exit and base diameters was kept small (see fig. 4).

The nozzle internal geometry was chosen to represent two types of flight operation, acceleration with maximum augmentation (large throat area) and cruise at unaugmented power (small throat area). Nozzles representing augmented-power configurations included those with 3°, 5°, and 10° boattails (see fig. 4). Also, some of the nozzles with 0° boattails represented augmented-power configurations. A ratio of throat area to maximum cross-sectional area of about 0.45 was maintained for these configurations except configuration 5 for which model geometric constraints altered the design.

The subsonic-cruise nozzles, $\beta = 20^{\circ}$, 15°, and 7.5°, are represented by configurations 6, 12, and 18 to 21. Consistent internal geometry for the highly boattailed subsonic configurations could not be maintained for the short-length boattails. A nozzle with an l/d_m of 0.6, a β of 7.5°, and a base annulus (configuration 19) was constructed with the same internal-expansion ratio as that of the nozzle with an l/d_m of 0.6 and a β of 15° (configuration 18) to evaluate the trade-off between boattail angle and base area. Configuration 21 was included for a comparison with a similar configuration reported in reference 20.

Instrumentation and Tests

Static pressures were measured on the boattail surface, in the divergent part of the nozzles, on the cylindrical portion of the model, in the model-shell gap, and, when applicable, on the model base with strain-gage pressure transducers remotely located from the model. The locations of the static-pressure orifices are given in tables I and II. The stagnation temperature and pressure in the stream of the jet ahead of the nozzle throat were measured with a thermocouple and total pressure probe. The forces and moments on that portion of the model aft of the gap at axial station 52.07 (fig. 2) were measured simultaneously with the pressure measurements by a three-component strain-gage balance.

The tests were conducted at 0° angle of attack and through a Mach number range of 0.30 to 1.30. The ratio of jet total pressure to free-stream static pressure ranged from jet off up to a maximum value of about 13. For each jet-on tunnel run, as each Mach number was held constant, a sweep of the desired range of jet total-pressure ratios was made. Generally the sweep was from the high pressure ratio to the low one in discrete steps; repeat points were taken as pressure ratio was increased. Both Mach number and jet pressure ratio were held constant as each point of data was taken. A jet-off point was taken at the beginning and end of every sweep. In addition to the jet-on tunnel runs, jet-off tunnel runs were made for all the configurations. For each jet-off run, data were taken at specific Mach numbers as Mach number was increased, and repeat points were taken as Mach number was decreased. For each data point, approximately five frames of data were recorded within 1 second and the average was used to compute the values of force, pressure, and so forth.

Data Reduction

The boattail axial-force coefficient $C_{A,\beta}$ is the coefficient of the nozzle external-pressure drag on the axially projected area from A_m to A_b. No attempt was made to include the forces on the small rim at the nozzle exit between d_b and d_e. (See fig. 4.)

The axial-force coefficients are equivalent to drag coefficients since the angle of attack was zero for all configurations. The coefficient is based on the maximum cross-sectional area of the model and was obtained from pressure data either by assigning an incremental area to each pressure orifice at $\phi = 0^{\circ}$ and computing it from the equation

$$C_{A,\beta} = \frac{1}{qA_m} \sum_{i=1}^{n} (p_{\infty} - p_i) A_{\beta,i}$$

or by plotting the values of C_p for each orifice at $\phi = 0^{\circ}$ as a function of $\left(\frac{r}{R_m}\right)^2$ and integrating with a planimeter. Skin friction is not included. The planimeter method of determining the boattail axial-force coefficient was used for the configurations with large boattail angles because it was determined that the pressure-area summation method gave erroneous results when there were large pressure gradients. To get answers of sufficient accuracy by the summation method at such conditions would require a closer axial spacing and greater number of pressure orifices than were installed in the nozzles in this investigation. For all conditions in which there was doubt about the accuracy of the pressure-area summation method, the planimeter integration method of computing the boattail axial-force coefficient was used.

Configuration 19 with a boattail angle of 7.5° had a larger base annulus than all the other configurations; therefore, both the boattail axial-force coefficient and the boattail-plus-base-annulus axial-force coefficient are presented. The boattail-plus-base-annulus axial-force coefficient was calculated as follows:

$$C_{A,a} = C_{A,\beta} - C_{p,b}\left(\frac{d_b^2 - d_e^2}{d_m^2}\right)$$

Here the pressure orifice on the base annulus was located at $\phi = 90^{\circ}$.

A comparison was made between the force data and pressure data for the jet-off conditions. To perform this comparison, all the rows of pressure orifices were used to compute a boattail axial force and a coefficient of this axial force was obtained based on qA_m. Since the balance measured the total force on the model from the gap aft, the afterbody axial-force coefficient obtained from the balance measurement was corrected for gap force and skin-friction drag between the gap and the base of the model. The skin-friction-drag calculation was based on turbulent-boundary-layer theory. The afterbody axial-force coefficient was calculated from the balance as follows:

$$C_{A,bal} = \frac{1}{qA_m}\left[F_{A,bal} - \sum_{i=1}^{n} (p_{i,gap} - p_{\infty}) A_{i,gap} - F_{A,f}\right]$$

In this equation, $F_{A,f}$ is the computed skin-friction force between the gap and the base of the model. The base axial-force coefficient used in the correlation of the force and pressure data was obtained by using the equation

$$C_{A,b} = \frac{1}{qA_m}\left[\frac{\sum_{i=1}^{n}\left(p_\infty - p_{dw,i}\right)}{n}\right]A_b$$

where the $p_{dw,i}$ are the pressures on the wall of the divergent portion of the nozzle and where A_b is calculated by using d_b (see fig. 4). In calculating $C_{A,b}$ by this method, it is assumed that the average divergent-wall pressure exists over the throat during the jet-off runs.

PRESENTATION OF RESULTS

Jet-Off Data

Figure
Typical boattail pressure-coefficient distributions 5
Effect of boattail angle on boattail pressure-coefficient distributions 6
Variation of boattail axial-force coefficient with free-stream Mach number 7
Variation of boattail axial-force coefficient with ratio of boattail flap length to maximum diameter 8
Variation of boattail axial-force coefficient with boattail angle 9
Comparison of boattail axial-force coefficients with those computed by method of characteristics 10
Comparison of pressure and force measurements 11

Effect of Jet Total-Pressure Ratio

Effect of jet total-pressure ratio on boattail pressure-coefficient distributions . . 12
Typical nozzle internal-pressure distributions 13
Variation of boattail axial-force coefficient with jet total-pressure ratio 14

Effect of Jet Exit-Pressure Ratio

Variation of boattail axial-force coefficient with jet exit-pressure ratio. 15
Variation of boattail axial-force coefficient with ratio of boattail flap length to maximum diameter 16

DISCUSSION

Jet-Off Measurements

The strut-supported air-powered nacelle model used in the present investigation was located forward in the tunnel test section and below the tunnel center line. Flow-field investigations showed that the flow was relatively uniform over the model. The measured boundary-layer displacement thickness was approximately 0.10 of the boundary-layer thickness and 0.011 of the maximum diameter of the model. The boundary-layer momentum thickness was 0.0080 of the model maximum diameter at $M = 0.60$ and 0.0092 of the model maximum diameter at $M = 1.30$. More detailed information about the model flow field is given in appendix B.

Figure 5 illustrates the reason for using the top row of orifices (at $\phi = 0^\circ$) for pressure integration. It shows typical boattail pressure-coefficient distributions on a boattailed afterbody at various Mach numbers and values of ϕ. The discrepancy between the values of pressure coefficient of the different rows at Mach numbers of 0.90 and 1.30 is thought to be caused by the flow disturbance of the model support strut, and hence, the top row of pressure orifices is the most interference free as is also indicated in appendix B. Therefore, only the top row was used for pressure comparisons and when integrating the boattail pressures for axial force in the rest of the report.

Figures 5 to 11 show the jet-off characteristics for the different configurations. The variation of boattail axial-force coefficient with Mach number is shown in figure 7 for all configurations with conical boattails. Between, but not including, Mach numbers of 0.95 and 1.20, normal and reflected shocks which were influenced by the support strut and which may have impinged on the model or near its base caused the absolute value of the pressure level to be in doubt. This result precludes the use of data in this region and these points are not included in the faired values of boattail axial-force coefficient. Figure 7(d) presents data for a 15° sharp-corner boattail having the same geometric parameters as one in reference 20 (ratio of boattail radius of curvature to diameter of 0). The dashed line represents data from reference 20 for the boattail with a ratio of sting diameter to base diameter of 0.605. It is believed that the main difference between the levels of the boattail axial-force coefficients for the two investigations is due to the influence of the sting which can cause a reduction in the boattail axial-force coefficient compared with the no-sting condition (see ref. 21). The variation of boattail axial-force coefficient with the ratio of boattail flap length to maximum diameter is given in figure 8. In addition, the ratio of base area to maximum area is indicated. This figure, together with the boattail pressure distributions, shows that for conditions in which boattail pressures were lower than free-stream static pressure, shortening the boattail with β constant decreased the boattail axial force, whereas for conditions in which boattail pressures had recovered to greater than free-stream value, shortening the boattail with β constant increased the boattail axial force (see figs. 5(b) and (c) and fig. 8(c)). The axial-force coefficients for the short-length boattails, $l/d_m = 0.6$, are plotted as a function of boattail angle in figure 9.

Since no theory adequately predicts the effects of the jet on boattail pressures, the jet-off data were compared with theory. Boundary-layer measurements obtained at station 104.14 indicate that the local Mach number approaching the boattail corner was approximately 0.02 above the free-stream Mach number. Data from figure 7 at free-stream Mach numbers of 1.20 and 1.30 are plotted in figure 10 at free-stream Mach numbers of 1.22 and 1.32, respectively. These data are compared with data computed by the axisymmetric method of characteristics at Mach numbers of 1.22 and 1.32. The agreement between the calculated and measured boattail axial-force coefficient is good except for the 15° boattails. The discrepancy between the theoretical and experimental results for the 15° boattails results from the failure of the theory to predict the more positive pressure distribution near the base of the boattail (see fig. 6).

Figure 11 shows a comparison between jet-off force data and jet-off pressure data for a typical boattailed afterbody. For this comparison, the axial force calculated from the pressure measurements was obtained by integrating all the rows of boattail pressures. To this force, the base axial force was added giving a parameter with which to compare the force data. The method of obtaining the base axial-force coefficient and the afterbody axial-force coefficient from the balance measurements is discussed in the section, "Data Reduction." The agreement between the force and pressure data for this configuration is within 2 percent at the supersonic Mach numbers and generally within 10 percent at the subsonic Mach numbers. The actual magnitude of the discrepancy, however, is only a difference in axial-force coefficients of 0.005 based on nacelle cross-sectional area.

Jet Effects

Boattail pressure-coefficient distributions for various jet total-pressure ratios and several Mach numbers are shown in figure 12 for all conical-boattailed configurations tested. The distributions are presented with the configurations grouped according to constant boattail angles so that the effect of shortening the nozzle flap length can be observed. Axial location of the pressure orifices was measured from station 104.14, the common theoretical hinge point for each length nozzle. This point is indicated in the figure by a heavy vertical line. For boattail angles of 3°, 5°, and 10°, the pattern of shortening the nozzle flap was to keep the boattail angle the same, shorten the nozzle, keep the throat area the same, and allow the divergence angle and exit area to increase. All the configurations with boattail angles of 15° have the same internal-expansion ratio except one, the one with an l/d_m of 0.60. One factor determining the jet effect on boattail pressures, plume shape, depends to a large degree on exit static-pressure ratio and nozzle divergence angle. Therefore the design jet total-pressure ratios and nozzle divergence half-angles are included for each configuration to help in understanding the effect of the jet on boattail pressures.

Figure 12 shows that for a given boattail angle, the nozzles with higher fineness ratios generally provide greater recovery of pressure, a fact that can also be noted in Salmi's paper (ref. 11). Another point of particular interest is the tendency for the jet to affect the pressures over the entire length of the boattail for the configurations with the larger boattail angles at Mach numbers of 0.8 and 0.9 and, for the configuration with a boattail angle of 20°, even at a Mach number of 1.20. Also, the location of the shock noticed on some configurations is seen to progress upstream with increasing total-pressure ratio. The extent of this effect shown in figure 12(c) for $M = 1.20$ was also found on similar configurations investigated by Forsgren (ref. 22). Figure 13, which presents the internal-pressure distributions for several configurations at various total-pressure ratios and the same Mach numbers, shows the approximate pressure ratio for internal flow separation. Reference 23 presents similar internal-pressure measurements for an overexpanded nozzle.

Figure 14 presents the variation of boattail axial-force coefficient with jet total-pressure ratio at several Mach numbers for all the conical-boattail configurations. Again, nozzles are grouped according to boattail angle so that the relative effect of the jet total-pressure ratio on the different-length boattails can be studied. Since the exit static-pressure ratio and Mach number directly affect the amount of jet pluming and hence the amount of jet interference on a boattail, the effects of total-pressure ratio on boattail axial force for nozzles with different boattail angles are not directly comparable because the design total-pressure ratios vary from configuration to configuration. The design total-pressure ratio also varies slightly with boattail length for a given boattail angle.

As mentioned previously, the nozzle with a 7.5° boattail angle and a large base annulus, configuration 19, was included to investigate a trade-off between boattail axial force and base axial force. The data for this configuration are presented both as the axial-force coefficient of the boattail only and as the axial-force coefficient of the boattail plus base annulus (fig. 14(e)). A comparison of the axial force of the boattail plus base annulus with the axial force of the boattail of its equivalent nozzle, the one with a boattail angle of 15° and an l/d_m of 0.6 (configuration 18, fig. 14(d)), shows that trading off boattail axial force for base axial force does have some advantages for this nozzle at higher Mach numbers. However, this trade-off is detrimental in the Mach number range up to and including 0.80 for which the internal geometry of the nozzle is designed.

Because the design jet total pressure generally varies as the nozzle configuration changes, a more meaningful parameter than the jet total-pressure ratio for comparing the jet effects on the boattail axial force is the jet exit-pressure ratio. Figures 15 and 16 present the data using this parameter in which p_e is considered to be represented by the most rearward orifice in the nozzle wall.

In figure 15, which presents the boattail axial-force coefficient as a function of the jet exit-pressure ratio, the solid symbols indicate conditions at which the jet exhaust has separated from the internal walls of the nozzle. Figure 15 shows that, as would be expected, all the configurations experienced a continuous decrease in boattail axial force with increasing pressure ratio above an exit-pressure ratio of about 1.0. However, the figure also indicates that, generally, for the same exit pressure ratio, the configurations with large boattail angles recieved greater benefit from the jet interference, compared with the jet-off conditions, than those with small boattail angles. This effect possibly results because the external flow at the nozzle exit of the configurations with large boattail angles must turn a greater angle to aline itself with the jet exhaust than the external flow at the exit of the configurations with small boattail angles. Thus for the boattails with large angles, greater compression of the flow occurs thereby causing more favorable jet interference effects with equal pluming, or with equal contracting, of the jet exhaust.

The boattail axial-force coefficient as a function of the ratio of boattail flap length to maximum diameter is presented at various values of jet exit-pressure ratio and for several Mach numbers in figure 16, a summary of figure 15. This figure shows that the boattail axial force of the configurations with boattail angles of 3° and 5° continuously declines as the boattail flap length is shortened. Inspection of figure 12 shows that this continuous decline would be expected because the pressure on the boattails of these configurations never recovers to the free-stream value. For the configurations with boattail angles of 10° and 15° at conditions in which the pressure recovers to greater than free-stream value, shortening the boattail can cause the axial force to rise. However, this effect does not always occur when the jet is operating, a fact illustrated by plots for the 15° boattails at Mach numbers of 0.40, 0.80, and 0.90 (fig. 16(d)). Here, as the boattail is shortened from an l/d_m of 1.0 to 0.8, the influence of the jet over the forward portion of the boattail increases and the result is a decreased axial force even though a portion of the boattail with positive pressures acting on it was removed. There is a limit to this latter effect, as can be seen by the increase in boattail axial force between an l/d_m of 0.8 and 0.6 for the 15° boattailed configurations. Whether the rise in axial force would be as abrupt or have the magnitude that is indicated in the figure is questionable because the boattail shoulder of the configuration with an l/d_m of 0.638 was inadvertently rounded slightly when the model was faired, and this rounded shape quite probably resulted in a lower drag than would have existed if the boattail shoulder had been sharper. How much lower is hard to estimate. Of course the boattail axial force must eventually start declining again as the boattail length is decreased, for if the length were reduced to zero, the area and hence the axial force would be zero. Also shown in figure 16(d) are symbols plotted at the l/d_m of the similar configuration with sting jet simulators from reference 20. The values from Shrewsbury's report should correspond to a jet exit-pressure ratio of 1.0.

CONCLUDING REMARKS

An investigation was conducted in the Langley 16-foot transonic tunnel to determine the jet effects on the boattail axial force (i.e., boattail drag since angle of attack is zero) of nozzles having conical afterbodies. The results of the investigation indicate that with the jet off and with the boattail angle constant, shortening the boattail at conditions in which the boattail pressures were below free-stream static pressure decreased the boattail axial force, whereas shortening the boattail at conditions in which the boattail pressures had recovered to greater than free-stream value increased the boattail axial force. Contrary to the jet-off conditions, with the jet operating, shortening the boattail and keeping the boattail angle constant at conditions in which the boattail pressures have recovered to greater than free-stream value can cause a decrease in axial force by allowing the jet exhaust to have a greater influence on the pressures on the forward portion of the boattail.

Generally, boattail axial force continually decreased with increasing pressure ratio above a jet exit-pressure ratio of about 1.0. For the same jet exit-pressure ratio, or the same amount of jet pluming, the configurations with the larger boattail angles generally derived more benefit from the jet interference, compared with the jet-off conditions, than those with the smaller boattail angles.

For two boattail configurations with ratios of flap length to maximum nacelle diameter of 0.6 and design total-pressure ratios of 4.62, the configuration with a 15° boattail angle and no base had lower afterbody axial forces at Mach numbers of 0.40, 0.60, and 0.80 than the configuration with a boattail angle of 7.5° and a base, but the configuration with a 15° boattail angle and no base generally had the higher axial forces at higher Mach numbers.

Langley Research Center,
National Aeronautics and Space Administration,
Langley Station, Hampton, Va., November 5, 1969.

APPENDIX A

REFERENCE NOZZLE WITH CIRCULAR-ARC BOATTAIL

A reference nozzle with a circular-arc boattail and internal and external geometries which followed the recommendations of the Supersonic Tunnel Association (STA) for a "standard nozzle" was tested on the air-powered nacelle in order to provide a reference level for the conical-boattail configurations. A sketch of this nozzle with its orifice locations is shown in figure 17. The jet total pressure for the standard nozzle was the average measurement of the five internal rake tubes. The data presented for this nozzle were calculated in the same manner as the data for the boattail configurations in the body of the report.

Jet-off boattail pressure-coefficient distributions for the reference nozzle are presented in figures 18 and 19, which respectively show the peripheral variation of boattail pressures and the variation of the pressure distribution for the top row of orifices ($\phi = 0^{\circ}$) with Mach number. The data from these figures generally are in good agreement with boattail pressure-coefficient data obtained on the STA standard exhaust nozzle presented in reference 24. The variation of jet-off axial-force coefficient with Mach number for the reference nozzle is given in figure 20. At Mach numbers of 0.80 and 0.90, the boattail axial-force coefficients of the reference nozzle closely match the jet-off values of afterbody XII in reference 25 which is geometrically similar. Also shown in figure 20 for comparison are the boattail axial-force coefficients for three of the conical boattails with $l/d_m = 1.0$ from figure 7(a), which have about the same fineness ratios as the circular-arc boattail. The circular-arc boattail has nearly the same drag level as the 10° conical boattail up to a Mach number of 0.80. The drag-rise Mach number was approximately the same as that for the 5° conical boattail. At supersonic speeds, the drag level of the reference nozzle lies between those of the 10° and 15° conical boattails.

The effect of jet total-pressure ratio on boattail pressure coefficients for the reference nozzle is presented in figure 21. At high subsonic speeds, the jet interference effects extend forward over the entire boattail, an effect also noted in reference 26. At a Mach number of 1.20, increasing the jet total-pressure ratio causes the shock-induced separation of the boattail to extend farther forward. Figure 22 shows the effect of jet operation on the boattail axial-force coefficient for the reference nozzle. The variation of axial force with jet total-pressure ratio is similar to that observed for the conical nozzles. Generally similar results were obtained with the curved afterbody, configuration IV, of reference 27. The variation of boattail axial-force coefficient with jet exit-pressure ratio for the reference nozzle is presented in figure 23.

APPENDIX B

CALIBRATION BODIES

Measurements on Cylindrical Afterbodies

The strut-supported air-powered nacelle model used in the present investigation was located forward of the normal location in the tunnel test section and below the tunnel center line. Because of the new location and possibility of support-strut interference, the cylindrical calibration body shown in figure 24 was constructed to determine the flow field in the region of the afterbody. Figure 25 shows the geometry of the model and strut as used in the survey of the boundary layer and the pressures along this cylindrical calibration afterbody. Three boundary-layer rakes were attached 45° apart to a removable section of the model so that they could be indexed to obtain data at $\phi = 0^{\circ}$, 45°, and 90° or at $\phi = 90^{\circ}$, 135°, and 180°. The locations of the afterbody pressure orifices were measured axially from station 104.14 with the rearward direction positive. Figure 26 gives the area distribution of the model and support strut. The maximum-blockage cross section of the model and support was 0.19 percent.

Figure 27 shows the static-pressure-coefficient distributions on the cylindrical afterbody for several Mach numbers. The pressures of the different rows of orifices are about equal except near the base where the pressure on the bottom row is lower, an effect possibly caused by the strut. The local static pressures along the afterbody for those Mach numbers shown are below free-stream static pressure and the decrease in the pressure coefficient toward the rear is indicative of the flow's turning into the base region.

The effect of length and open and flat bases on afterbody pressures and average base pressures, the average reading of several base pressure taps, are shown in figures 28 and 29. In these figures, the pressure coefficients of the cylindrical calibration afterbody are compared with those of configurations 2, 8, and 14 listed in the body of the report. The boattail angle is zero for each configuration. In figure 28, the pressure coefficients at $x/d_m = 0$, the corner (station 104.14) for the boattail nozzles, indicate similar pressure levels for all the different-length boattails. Although the most rearward orifices are not at the same location relative to the bases, generally similar trends occur for all the configurations indicating minor effects of the support system on the bodies of different lengths. Additional information on various base configurations for the test model is presented in reference 28.

The representative boundary-layer Mach number profiles in figure 30 were obtained from the total-pressure rakes and the static pressures on the model at the position of the rakes with the rakes removed. The boundary-layer thickness is about 1.52 cm

$(\delta/d_m = 0.1)$ and is very consistent at all values of ϕ except at 180°, where there is a loss in total pressure in the wake of the model support strut. The data in figure 30 indicate that the local Mach number approaching the boattail corner (station 104.14) was higher than the free-stream Mach number by 0.02 up to $M = 0.8$ and was higher than the free-stream Mach number by 0.012 to 0.016 from $M = 0.9$ to 1.30. The experimental and power-law-calculated boundary-layer profiles are compared in figure 31 for a representative subsonic and supersonic Mach number. The total temperature was assumed constant in calculating these profiles. The boundary-layer displacement thickness is approximately 0.10 of the boundary-layer thickness and 0.011 of the maximum diameter of the model. The boundary-layer momentum thickness is 0.0080 of the model maximum diameter at $M = 0.60$ and 0.0092 of the model maximum diameter at $M = 1.30$.

Pressure Distributions on Extended Strut-Mounted and Sting-Mounted Nacelle Model

External flow characteristics over bodies in transonic wind tunnels can be affected by blockage and tunnel operational conditions (refs. 29 and 30), tunnel-wall-boundary-reflected disturbances and support configurations (ref. 31), nose shape, and model fineness ratio (ref. 32). The extent to which these conditions may affect the data obtained in the present investigation is considered in this section.

The basic characteristics and model support system of the Langley 16-foot transonic tunnel are presented in reference 33. Subsequent to the publication of reference 33, the tunnel capability was increased by providing additional power and revised slot configurations which allow the tunnel to operate at low supersonic speeds up to a Mach number of 1.30. As the Mach number is increased above a value of about 1.0, the test section of uniform Mach number distribution gradually decreases in length until at $M = 1.30$, it is about 2.44 meters (8 ft) long extending from tunnel stations 39.63 meters to 42.1 meters (130 ft to 138 ft). Model length restrictions in the normal revised-tunnel test section for a center-line sting-mounted model are discussed in reference 31.

The air-powered nacelle model of the present investigation was located farther forward in the tunnel than the usual model installation position (model nose at tunnel station 39.2 meters (128.58 ft)) with the center line of the model 0.914 meters (3 ft) below the tunnel center line and was strut mounted from the floor. The possibility existed, therefore, that the flow over the strut-mounted nacelle model could be affected by the upstream and offcenter location of the model and by the support system.

To investigate the flow field of the model more thoroughly, the three configurations shown in figure 32 were tested. One was an extended cylindrical afterbody which was mounted on the air-powered jet nacelle used in the present investigation. A photograph of this model is shown in figure 33. The other two consisted of a survey body mounted on two different stings on the center line of the tunnel. The survey body was an exact replica of the surface contours of the air-powered jet nacelle with a cylindrical afterbody. The two stings positioned the center-line body at two axial locations in the tunnel, one coinciding with the axial position of the air-powered jet nacelle in the forward part of the test section and the other at the normal position in the center of the test section. This latter position is indicated in figure 32 by dashed lines and the former position is indicated by solid lines. Both the extended cylindrical afterbody mounted on the air-powered jet nacelle and the center-line survey body had only one row of orifices and were rotated to obtain pressure distributions at values of ϕ of 0^o, 90^o, and 180^o. The locations of the pressure orifices for the extended floor-mounted body were measured from model station 104.14, the same station that was used to locate the orifices for the conical-boattail configurations discussed in the main body of the report.

The pressure-coefficient distributions for the strut-mounted extended afterbody are shown for various free-stream Mach numbers in figure 34. Since a separate tunnel run was made with the single row of orifices indexed at each value of ϕ, the free-stream Mach numbers at which data were taken for each value of ϕ did not coincide exactly. The Mach numbers at which the data were taken are indicated in the figure. The pressure distributions at the subsonic Mach numbers of 0.40 and 0.95 are relatively flat and consistent with ϕ in the region of the boattail of the normal-length model $\left(x/d_m = -0.5 \text{ to } 1.0\right)$. Data between free-stream Mach numbers of 0.40 and 0.95 are not shown because the trends and relative levels of the pressure distributions in this speed range are very much like those at $M = 0.40$. The pressure distributions for Mach numbers of 1.00 to 1.30 show the magnitude of the shock disturbances on the extended afterbody and the positions of their intersection with it. At a Mach number of 1.00, the pressure rise is thought to be caused by a flow-field recompression whose position is influenced by the model support strut. For Mach numbers of 1.05 to 1.30, the shock reflections can be seen to progress aft and at $M = 1.20$ can be seen to be far enough behind the location of the base of the normal-length model not to influence its pressures.

The setting of the tunnel-wall-flat divergence angle was varied from -0.0833^o to 0.1667^o to determine the effect of test-section wall divergence on the pressure distributions over the strut-mounted extended cylindrical body. Only small changes in pressure levels were noticed; therefore, the remainder of the tests were run with the tunnel-calibration wall settings.

The sting-supported model had orifices extending over the entire length of the model (119.4 cm). The body fineness ratio was 7.83 and the blockage was 0.099 percent. Little or no effect of peripheral angle on the pressure distributions was found; therefore, the data have been averaged and the effect of model axial location in the wind tunnel on the pressure-coefficient distributions is shown in figure 35. Generally the pressure coefficients over the body are more negative for the forward position in the wind tunnel.

The samples shown are typical for all subsonic Mach numbers. These results indicate that measurements obtained over afterbodies located at the forward position can result in slightly higher values of boattail axial-force coefficient than would be obtained on a similar afterbody located at the normal test position.

A comparison of the experimental pressure-coefficient distributions obtained over the sting-supported body at the normal test position (nose at tunnel station 40.33 meters) with the slender-body theory of Laitone (ref. 34) is shown in figure 36 for a Mach number of 0.50. Agreement is generally good except in regions of high-velocity perturbations such as near the forebody shoulder radius and near the rear of the body where the flow turning into the base region causes lower pressures which feed forward through the boundary layer.

Pressure-coefficient distributions obtained on the strut-mounted model and the center-line sting-supported model, both with the noses located at tunnel station 39.2 meters, are presented in figure 37. Two conditions for the sting-supported model are shown, transition fixed with a strip of No. 80 grains located 2.54 cm back of the model nose and also transition free. The presence of the transition strip had a negligible effect on the afterbody pressure distributions. For most Mach numbers, the pressure coefficients measured on the strut-mounted nacelle show very close agreement with the pressure coefficients measured on the center-line sting-supported model except for the station nearest the base. The pressures near the base of the sting-supported model are probably influenced by the presence of the sting (refs. 31 and 35). At a Mach number of 1.00, the strut-mounted model exhibits an increase in pressure coefficient just ahead of the base which may be due to a strut-support-induced disturbance. At supersonic speeds, the agreement of the data of the two models is good but the pressure coefficients for the strut-mounted model are generally somewhat lower than the pressure coefficients for the sting-mounted model.

Lower pressures for the strut-supported model are also shown in figure 38. In this figure, data obtained at $M = 1.3$ are compared for the sting-supported center-line model, the strut-mounted model, and the strut-mounted model with the extended cylindrical afterbody. In the region of interest between $x_n/d_m = 6$ and 8, both strut-mounted models indicate lower pressures than the sting-mounted center-line model. The theoretical pressure-coefficient distribution obtained by the method of characteristics is also shown as the solid line in figure 38. There is excellent agreement between the sting-mounted model and the theory, which predicts a pressure coefficient of -0.005 at the base of the sting-mounted body ($\phi = 0^{\circ}$). The extended cylindrical model with higher fineness ratio also shows close agreement with theory for the orifices indexed at $\phi = 0^{\circ}$ beyond 8.5 body diameters where the afterbody may be out of the region of influence of the strut.

REFERENCES

1. Runckel, Jack F.: Review of NASA Exhaust Nozzle Research. Proceedings of NASA Conference on Supersonic-Transport Feasibility Studies and Supporting Research – September 17-19, 1963, NASA TM X-905, 1963, pp. 315-332.
2. Fraenkel, L. E.: Curves for Estimating the Wave Drag of Some Bodies of Revolution, Based on Exact and Approximate Theories. C.P. No. 136, British A.R.C., 1953.
3. Jack, John R.: Theoretical Pressure Distributions and Wave Drags for Conical Boattails. NACA TN 2972, 1953.
4. Maxwell, N. E.; and Shutts, W. H.: Aerodynamic Effects of Boattailing on a Body of Revolution – Mach Numbers 1.5, 2.0 & 2.5. Rept. No. CM-645 (Contract No. NORD 9028), Consolidated Vultee Aircraft Corp., Mar. 15, 1951.
5. Morris, Deane N.: A Summary of the Supersonic Pressure Drag of Bodies of Revolution. J. Aerosp. Sci., vol. 28, no. 7, July 1961, pp. 563-572.
6. Benson, J. L.; Miller, L. D.; and Horie, G.: Theoretical Study of Engine Exhaust Nozzle Airframe Integration. AEDC-TR-67-214, U.S. Air Force, Oct. 1967. (Available from DDC as AD 822 074.)
7. Patterson, R. T.: A Wind-Tunnel Investigation of the Drag of Conical Missile Afterbodies at Mach Numbers From 0.40 to 2.47 (TED No. TMB AD-3154). Aero. Rep. 857, David Taylor Model Basin, Navy Dept., Jan. 1954.
8. Silhan, Frank V.; and Cubbage, James M., Jr.: Drag of Conical and Circular-Arc Boattail Afterbodies at Mach Numbers From 0.6 to 1.3. NACA RM L56K22, 1957.
9. Armstrong, R. S.; and Miller, S. R.: Subsonic Aerodynamic Performance of Nozzle Installations in Supersonic Airplanes. J. Aircraft, vol. 5, no. 3, May-June 1968, pp. 230-235.
10. Cortright, Edgar M., Jr.; and Kochendorfer, Fred D.: Jet Effects on Flow Over Afterbodies in Supersonic Stream. NACA RM E53H25, 1953.
11. Salmi, Reino J.: Experimental Investigation of Drag of Afterbodies With Exiting Jet at High Subsonic Mach Numbers. NACA RM E54I13, 1954.
12. Cubbage, James M., Jr.: Jet Effects on the Drag of Conical Afterbodies for Mach Numbers of 0.6 to 1.28. NACA RM L57B21, 1957.
13. Rustemeyer, A. H.; and Twomey, E. J.: Thrust and Drag Characteristics of Several Turbojet Exhaust Models at Supersonic and High-Subsonic Mach Numbers. R-0922-16 (Contract NOa(s)55-134-c), Res. Dept., United Aircraft Corp., June 1957.

14. Beheim, Milton A.: Off-Design Performance of Divergent Ejectors. NACA RM E58G10a, 1958.

15. Swihart, John M.; Mercer, Charles E.; and Norton, Harry T., Jr.: Effect of Afterbody-Ejector Configurations on the Performance at Transonic Speeds of a Pylon-Supported Nacelle Model Having a Hot-Jet Exhaust. NASA TN D-1399, 1962. (Supersedes NASA MEMO 1-4-59L.)

16. Klann, John L.; and Huff, Ronald G.: Characteristics of Five Ejector Configurations at Free-Stream Mach Numbers From 0 to 2.0. NASA TM X-23, 1959.

17. Norton, Harry T., Jr.; Runckel, Jack F.; and Pendergraft, Odis C., Jr.: Transonic Performance of Two Convergent-Divergent Ejector Nozzles Designed for Corrected Secondary Flows of 3 and 9.4 Percent. NASA TM X-909, 1964.

18. Norton, Harry T., Jr.; and Pendergraft, Odis C. Jr.: Transonic Performance of a Convergent-Divergent Ejector Nozzle Designed for a Corrected Secondary-Weight-Flow Ratio of 0.07. NASA TM X-974, 1964.

19. Pendergraft, Odis, C., Jr.: Subsonic Cruise and Loiter Performance of a Multiposition Convergent-Divergent Ejector Applicable to a Supersonic Transport. NASA TM X-1535, 1968.

20. Shrewsbury, George D.: Effect of Boattail Juncture Shape on Pressure Drag Coefficients of Isolated Afterbodies. NASA TM X-1517, 1968.

21. Kurn, A. G.: Drag Measurements on a Series of Afterbodies at Transonic Speeds Showing the Effect of Sting Interference. Tech. Rep. No. 66298, Brit. R.A.E., Sept. 1966.

22. Forsgren, L. M.: SST Exhaust Nozzle Boattail Drag Tests at Subsonic and Transonic Conditions. Doc. No. D6-2559, Boeing Co., Oct. 1964.

23. Norton, Harry T., Jr.; Cassetti, Marlowe D.; and Mercer, Charles E.: Transonic Off-Design Performance of a Fixed Divergent Ejector Designed for a Mach Number of 2.0. NASA TM X-165, 1959.

24. Lowe, W. H.: General Dynamics High Speed Wind Tunnel Test of the Supersonic Tunnel Association Standard Exhaust Nozzle Model at Mach Numbers 0, 0.60, 0.70, 0.80, 0.90, 0.95 and 1.20. HST-TR-215-9, Gen. Dyn./Convair, [1969].

25. Henry, Beverly Z., Jr.; and Cahn, Maurice S.: Additional Results of an Investigation at Transonic Speeds To Determine the Effects of a Heated Propulsive Jet on the Drag Characteristics of a Series of Related Afterbodies. NACA RM L56G12, 1956.

26. Englert, Gerald W.; Vargo, Donald J.; and Cubbison, Robert W.: Effect of Jet-Nozzle-Expansion Ratio on Drag of Parabolic Afterbodies. NACA RM E54B12, 1954.

27. Henry, Beverly Z., Jr.; and Cahn, Maurice S.: Preliminary Results of an Investigation at Transonic Speeds To Determine the Effects of a Heated Propulsive Jet on the Drag Characteristics of a Related Series of Afterbodies. NACA RM L55A24a, 1955.

28. Compton, William B., III.: Effect on Base Drag of Recessing the Bases of Conical Afterbodies at Subsonic and Transonic Speeds. NASA TN D-4821, 1968.

29. Pel, C.; and Rustemeyer, A.: Investigation of Turbojet Exhaust-Interference Drag. Rep. R-0801-12 (Contract No. NOas 55-134-c), Res. Dep., United Aircraft Corp., Nov. 1955.

30. Nichols, James H.: Determination of Optimum Operating Parameters for the PWT 16-ft Transonic Circuit Utilizing One-Percent Bodies of Revolution. AEDC-TN-59-100, U.S. Air Force, Sept. 1959.

31. Capone, Francis J.; and Coates, Edward M., Jr.: Determination of Boundary-Reflected-Disturbance Lengths in the Langley 16-Foot Transonic Tunnel. NASA TN D-4153, 1967.

32. Mitchell, Glenn A.: Effect of Model Forebody Shape on Perforated Tunnel Wall Interference. NASA TM X-1656, 1968.

33. Ward, Vernon G.; Whitcomb, Charles F.; and Pearson, Merwin D.: Air-Flow and Power Characteristics of the Langley 16-Foot Transonic Tunnel With Slotted Test Section. NACA RM L52E01, 1952.

34. Laitone, E. V.: The Linearized Subsonic and Supersonic Flow About Inclined Slender Bodies of Revolution. J. Aeronaut. Sci., vol. 14, no. 11, Nov. 1947, pp. 631-642.

35. Cahn, Maurice S.: An Experimental Investigation of Sting-Support Effects on Drag and a Comparison With Jet Effects at Transonic Speeds. NACA Rep. 1353, 1958. (Supersedes NACA RM L56F18a.)

TABLE I.- NOZZLE-SURFACE ORIFICE LOCATIONS

(a) Conical boattails

ϕ, deg	Boattails with $l/d_m = 1.0$		Boattails with $l/d_m = 0.8$		
	x/d_m for –		x/d_m for –		
	$\beta = 3^\circ$, 5°, and 10°	$\beta = 15^\circ$	$\beta = 3^\circ$ and 5°	$\beta = 10^\circ$	$\beta = 15^\circ$
0 and 90	-0.02	-0.02	-0.02	-0.02	-0.02
	.02	.02	.02	.02	.02
	.08	.08	.08	.08	.08
	.25	.25	.20	.20	.20
	.50	.50	.40	.40	.40
	.75	.75	.60	.60	.60
	.97	.95	.78	.77	.76
45, 135, 157.5, and 180	.02	.02	.02	.02	.02
	.25	.25	.20	.20	.20
	.50	.50	.40	.40	.40
	.75	.75	.60	.60	.60
	.97	.95	.78	.77	.76

ϕ, deg	Boattails with $l/d_m = 0.6$			Boattail with $l/d_m = 0.638$
	x/d_m for –			x/d_m for $\beta = 15^\circ$
	$\beta = 3^\circ$, 5°, 7.5°, and 10° (a)	$\beta = 15^\circ$	$\beta = 20^\circ$	
0 and 90	-0.02	-0.02	-0.02	-0.02
	.02	.02	.02	.02
	.08	.08	.08	.08
	.15	.15	.15	.15
	.30	.30	.30	.30
	.45	.45	.45	.45
	.58	.56	.54	.57
45, 135, 157.5, and 180	.02	.02	.02	.02
	.15	.15	.15	.15
	.30	.30	.30	.30
	.45	.45	.45	.45
	.58	.56	.54	.57

[a] Base orifices for the configuration with $l/d_m = 0.6$ and $\beta = 7.5^\circ$ are located at $\phi = 0^\circ$, 90°, and 180°.

(b) Cylindrical boattails; $\phi = 0^\circ$ and 45°

x/d_m for –		
$l/d_m = 1.0$	$l/d_m = 0.8$	$l/d_m = 0.6$
-0.25	-0.25	-0.25
.42	.42	0
.92	.74	.42

TABLE II.- NOZZLE DIVERGENT-WALL ORIFICE LOCATIONS; $\phi = 337.5^\circ$

Boattails with $l/d_m = 1.0$			Boattails with $l/d_m = 0.8$			
f/d_m for –			f/d_m for –			
$\beta = 3^\circ$	$\beta = 5^\circ$ and 10°	$\beta = 15^\circ$	$\beta = 3^\circ$	$\beta = 5^\circ$	$\beta = 10^\circ$	$\beta = 15^\circ$
0.17	0.17	0.17	0.17	0.17	0.15	0.17
.33	.33	.33	.34	.34	.32	.33
.50	.50	.50	.50	.50	.48	.50
.67	.67	.67	.67	.67	.65	.67
.83	.83	.83	.75	.75	.73	.83
.91	.92	1.00	.83	.84	.82	1.00
1.00	1.00	1.12	.92	.92	.90	
1.08	1.08	1.17	1.00	1.00	.98	
1.16	1.17		1.08	1.08	1.07	

Boattails with $l/d_m = 0.6$						Boattail with $l/d_m = 0.638$
f/d_m for –						f/d_m for $\beta = 15^\circ$
$\beta = 3^\circ$	$\beta = 5^\circ$	$\beta = 7.5^\circ$	$\beta = 10^\circ$	$\beta = 15^\circ$	$\beta = 20^\circ$	
0.17	0.16	0.17	0.17	0.17	0.02	0.17
.34	.33	.33	.34	.33	.07	.33
.50	.49	.50	.42	.50	.19	.50
.66	.66	.67	.50	.67	.36	.67
.75	.74	.83	.59	.75	.53	.75
.83	.83	.92	.67	.83	.69	.83
.91	.91		.75	.92	.86	.91
			.84			
			.92			

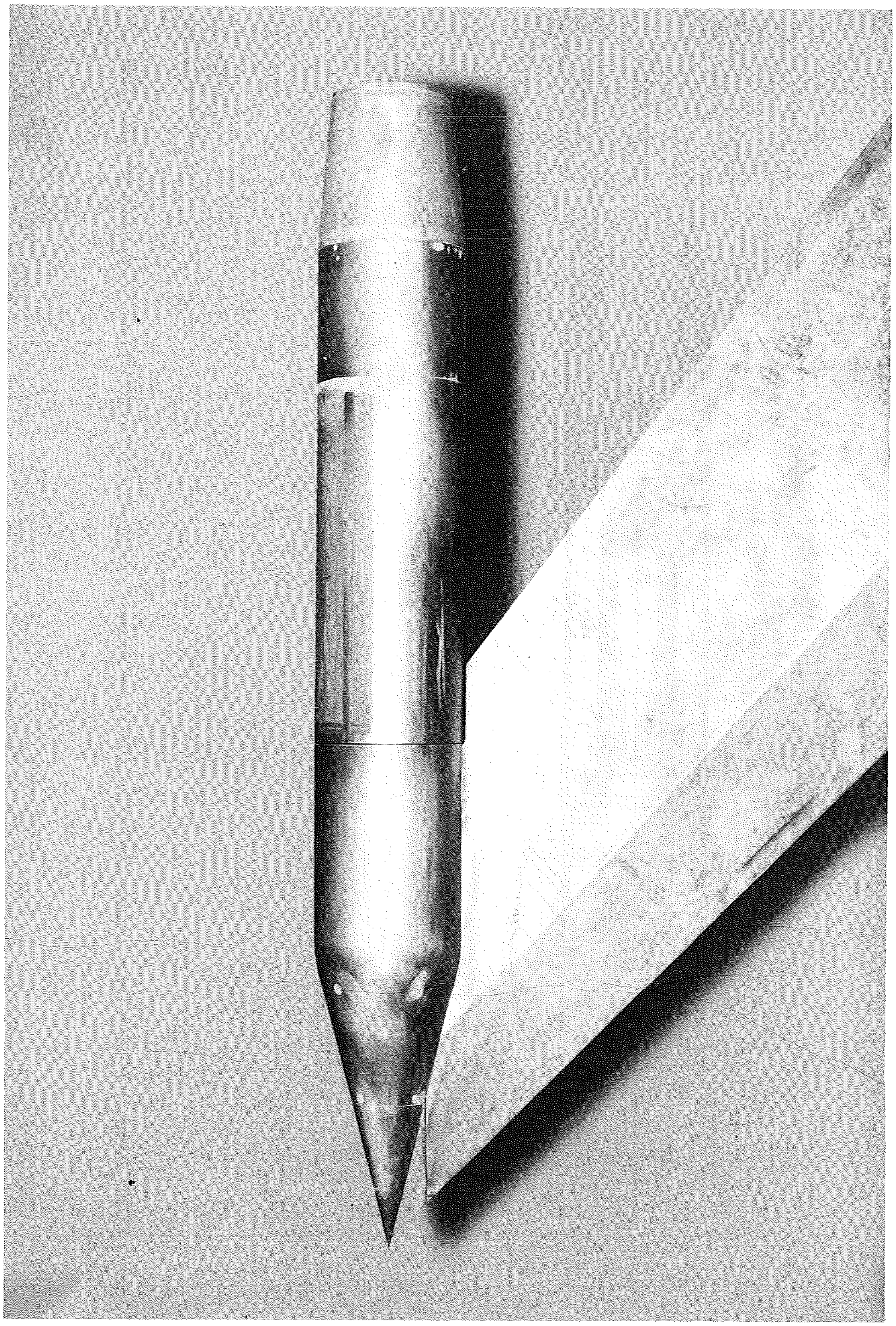

L-67-1987

Figure 1.- Photograph of model having nozzle with $l/d_m = 1.0$ and $\beta = 5^{\circ}$.

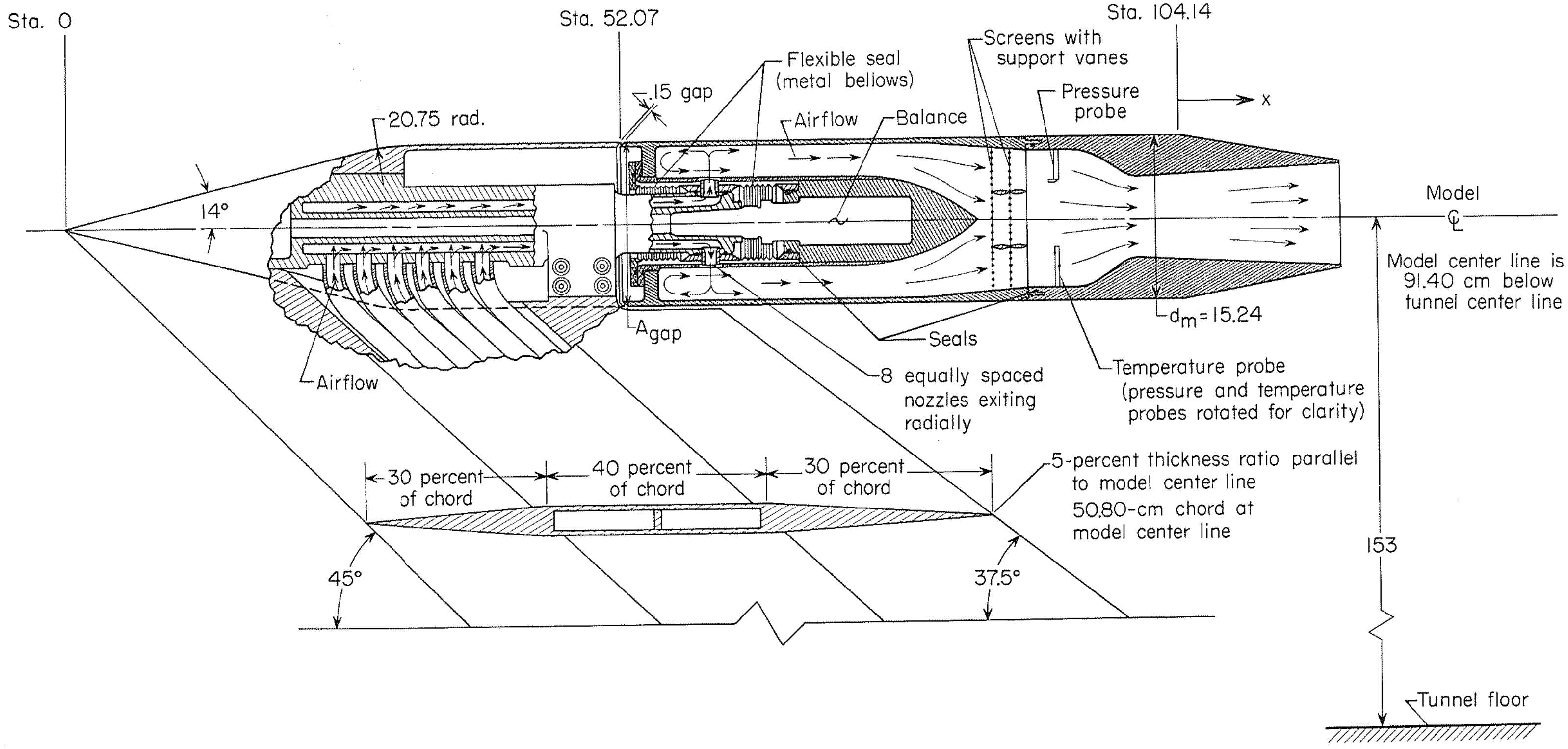

Figure 2.- Sketch of air-powered nacelle model with variable-flap nozzle configuration installed. (All dimensions are in centimeters unless otherwise noted.)

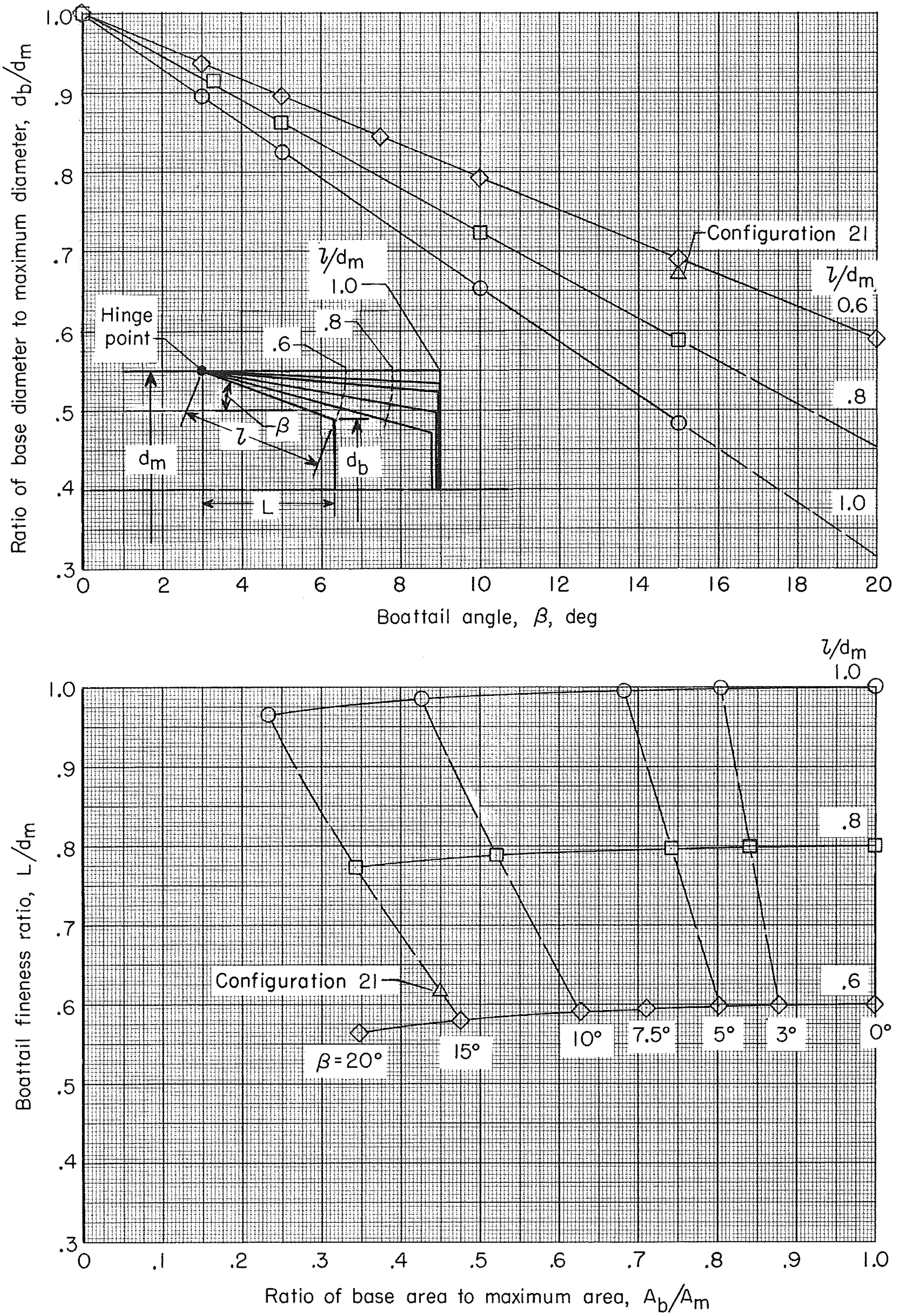

Figure 3.- Graphic illustration of extent of boattail geometric variations.

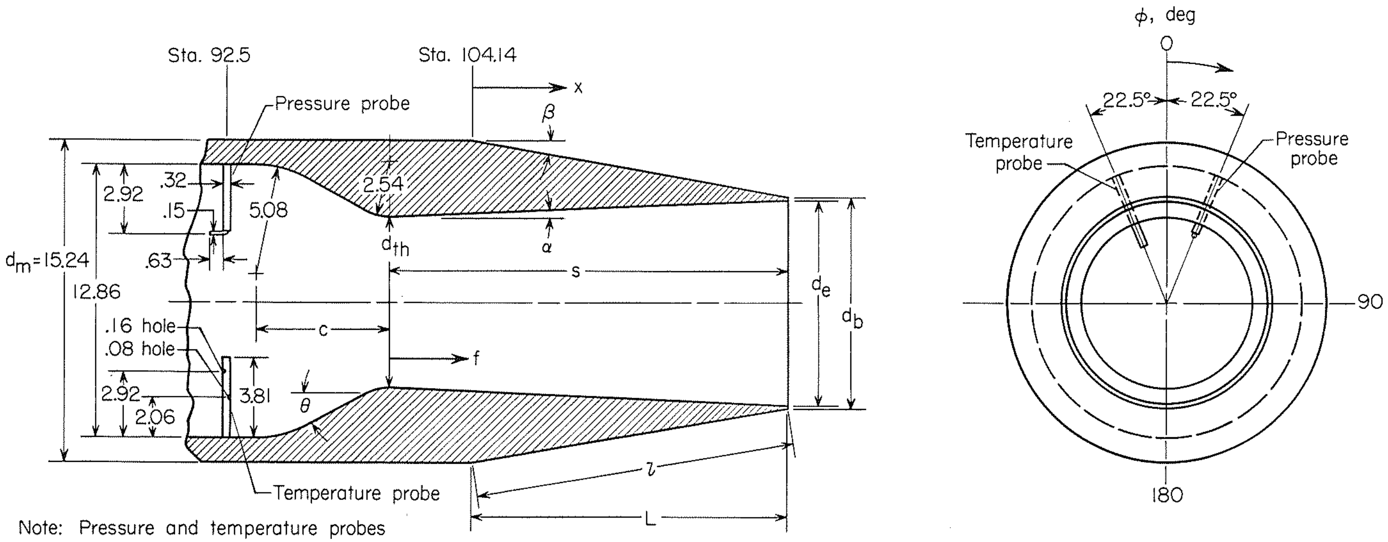

Note: Pressure and temperature probes shown rotated out of position for clarity in side view.

Configuration	Type nozzle	Design dimensions												
		l/d_m	β, deg	L/d_m	d_b/d_m	A_b/A_m	A_e/A_b	A_{th}/A_m	ϵ_e	s/d_{th}	α, deg	c/d_{th}	θ, deg	$(p_{t,j}/p_\infty)_{des}$
1	Super. cruise	1.0	0	1.000	1.000	1.000	0.970	0.247	3.925	2.444	11.5	0.860	30	32.60
2	Max. aug.	1.0	0	1.000	1.000	1.000	.970	.454	2.139	1.826	7.2	.484	20	11.95
3		1.0	3.00	1.000	.895	.802	.970	.452	1.716	1.840	4.8	.485	20	8.08
4		1.0	5.02	.996	.825	.681	.965	.445	1.460	1.846	3.2	.485	20	5.91
5		1.0	10.00	.985	.653	.426	.955	.366	1.111	2.049	.8	.689	20	3.14
6	Sub. cruise	1.0	15.00	.966	.482	.233	.939	.218	1.087	2.765	.4	1.063	30	2.94
7	Super. cruise	.8	0	.800	1.000	1.000	.970	.293	3.307	2.045	11.5	.487	30	24.80
8	Max. aug.	.8	0	.800	1.000	1.000	.970	.454	2.135	1.659	8.0	.477	20	11.95
9		.8	3.30	.800	.916	.839	.968	.452	1.795	1.670	5.8	.487	20	8.77
10		.8	5.00	.797	.861	.741	.965	.450	1.589	1.678	4.4	.486	20	6.98
11		.8	10.00	.788	.722	.521	.959	.450	1.111	1.682	.9	.486	20	3.14
12	Sub. cruise	.8	15.00	.773	.586	.343	.950	.300	1.086	2.062	.6	.712	30	2.94
13	Super. cruise	.6	0	.600	1.000	1.000	.970	.360	2.695	1.627	11.5	.530	30	17.70
14	Max. aug.	.6	0	.600	1.000	1.000	.970	.455	2.156	1.459	9.1	.474	20	11.95
15		.6	3.00	.599	.937	.878	.968	.453	1.876	1.468	7.2	.480	20	9.52
16		.6	5.00	.598	.895	.802	.967	.450	1.722	1.477	6.0	.482	20	8.14
17		.6	10.00	.590	.792	.627	.962	.451	1.340	1.482	3.0	.484	20	4.92
18	Sub. cruise	.6	15.00	.580	.698	.475	.957	.350	1.300	1.682	2.4	.595	30	4.62
19		.6	7.50	.595	.843	.711	.642	.350	1.300	1.709	2.4	.465	30	4.62
20		.6	20.00	.564	.590	.347	.950	.330	1.186	1.637	.8	.703	30	3.74
21		.638	15.00	.616	.670	.449	.956	.395	1.087	1.628	.7	.510	30	2.94

Figure 4.- Geometry and dimensions of variable-flap nozzle configurations. (All dimensions are in centimeters unless otherwise noted.)

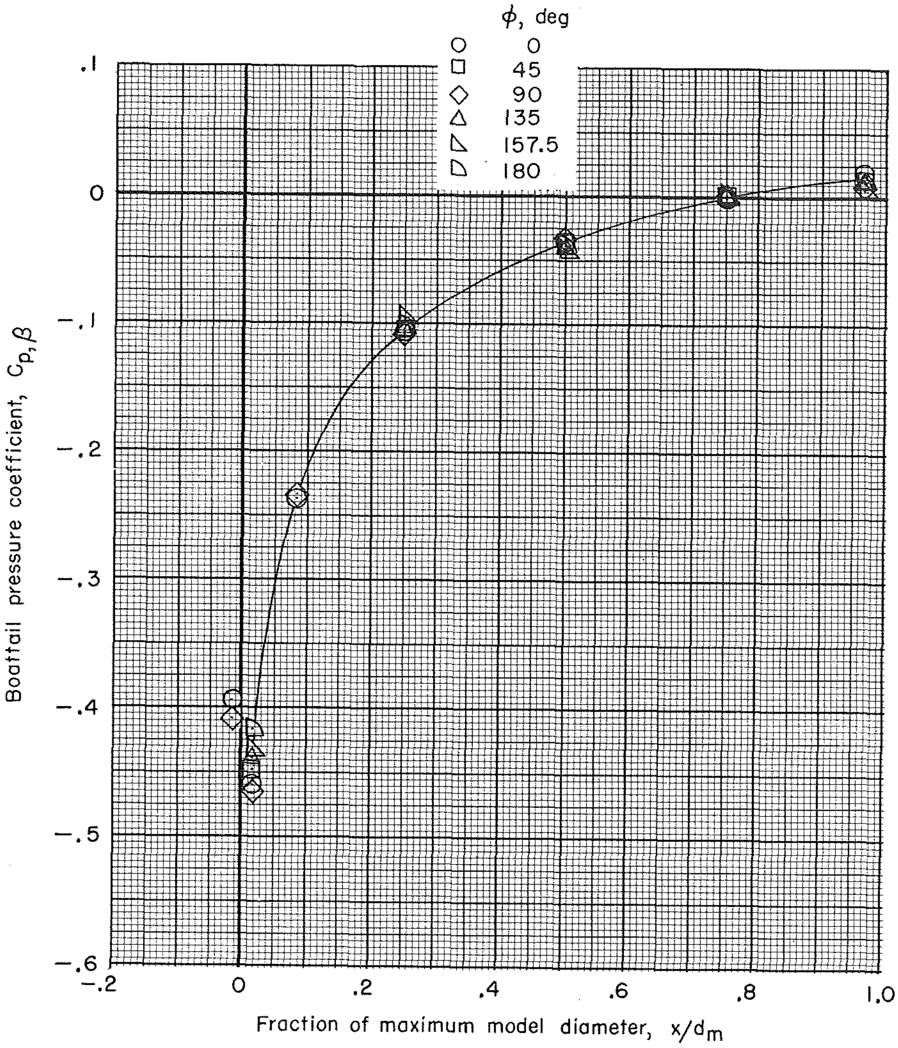

(a) $M = 0.60$.

Figure 5.- Typical boattail pressure-coefficient distributions for several free-stream Mach numbers and values of Φ. $l/d_m = 1.0$; $\beta = 10^0$; jet off.

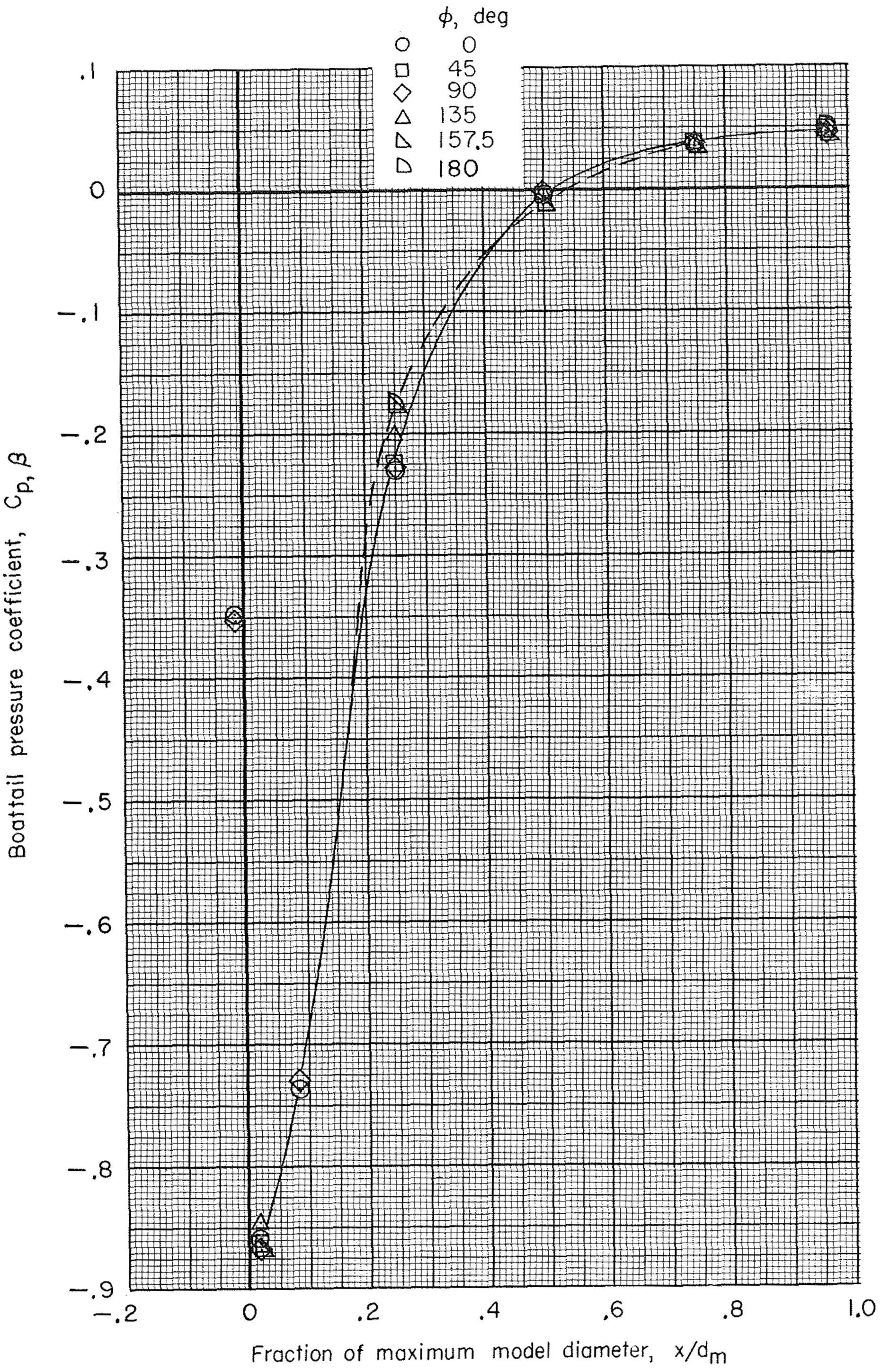

(b) M = 0.90.

Figure 5.- Continued.

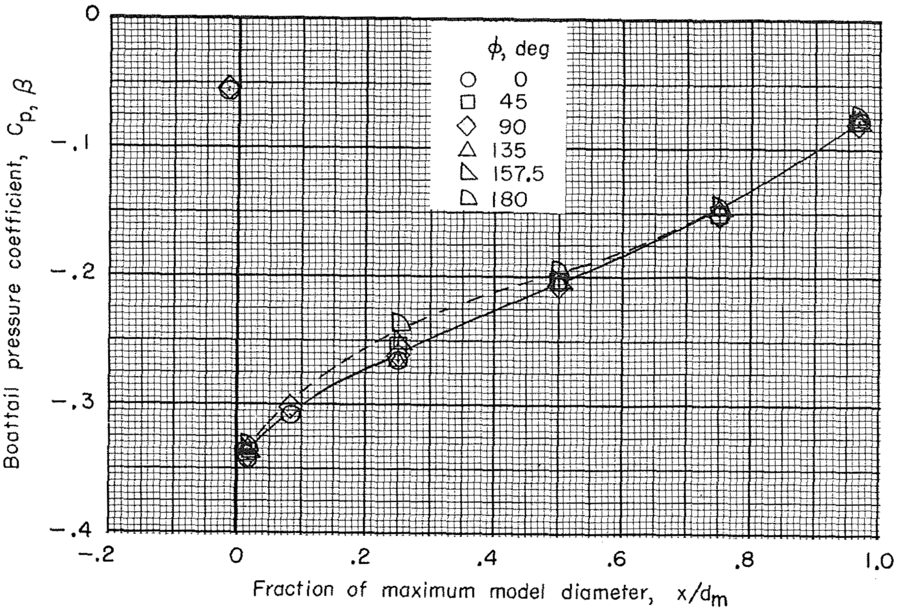

(c) M = 1.30.

Figure 5.- Concluded.

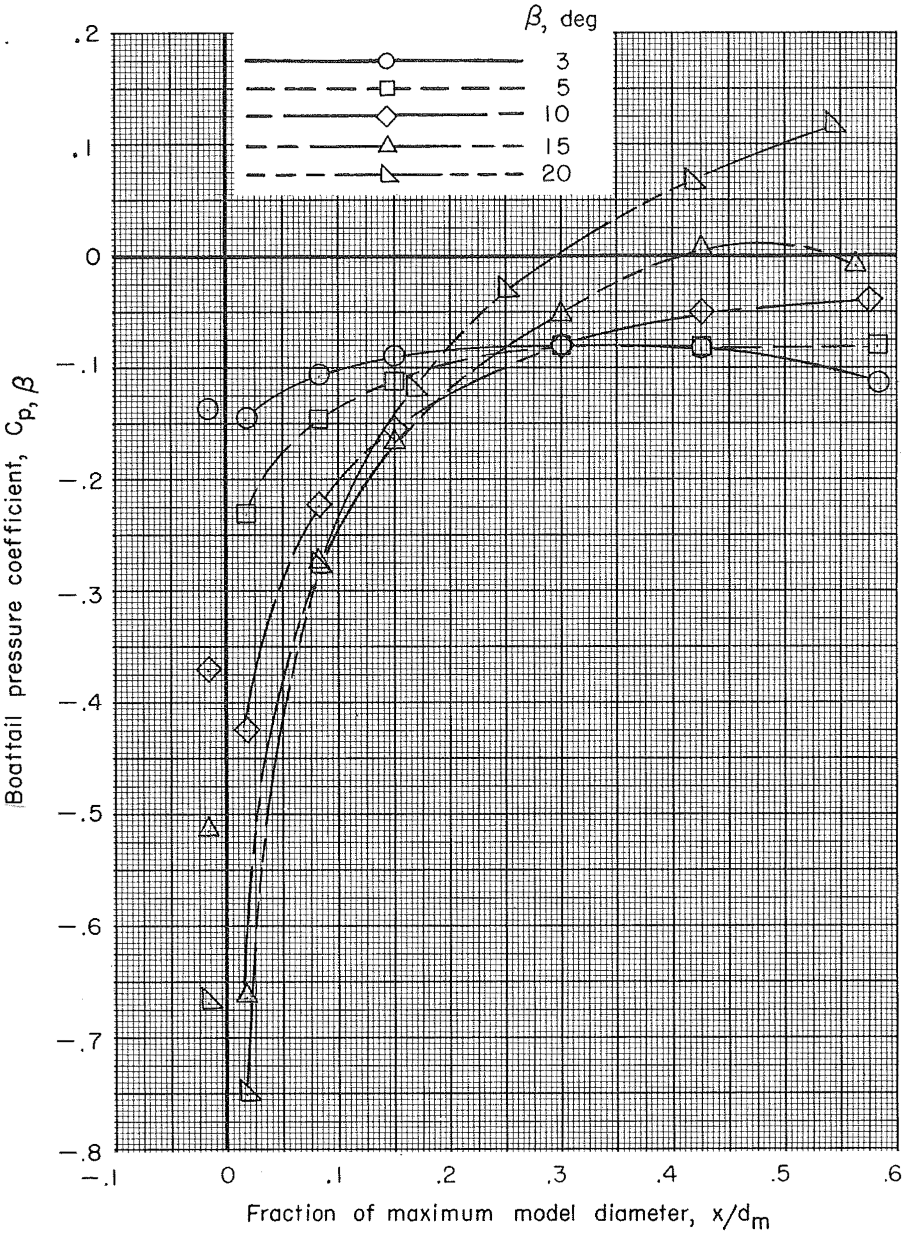

(a) M = 0.50.

Figure 6.- Effect of boattail angle on boattail pressure-coefficient distributions at typical free-stream Mach numbers. $l/d_m = 0.6$; jet off.

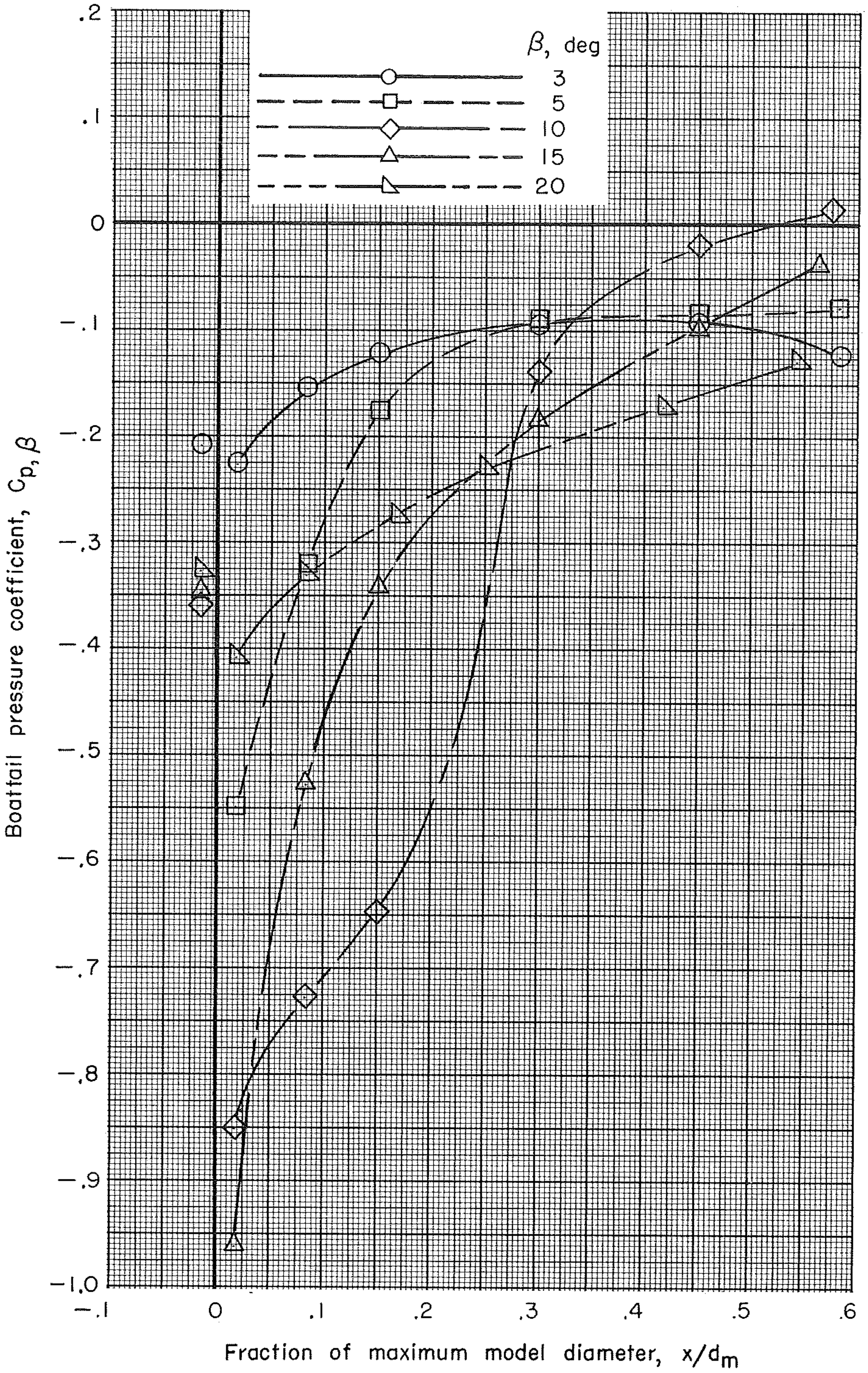

(b) M = 0.90.

Figure 6.- Continued.

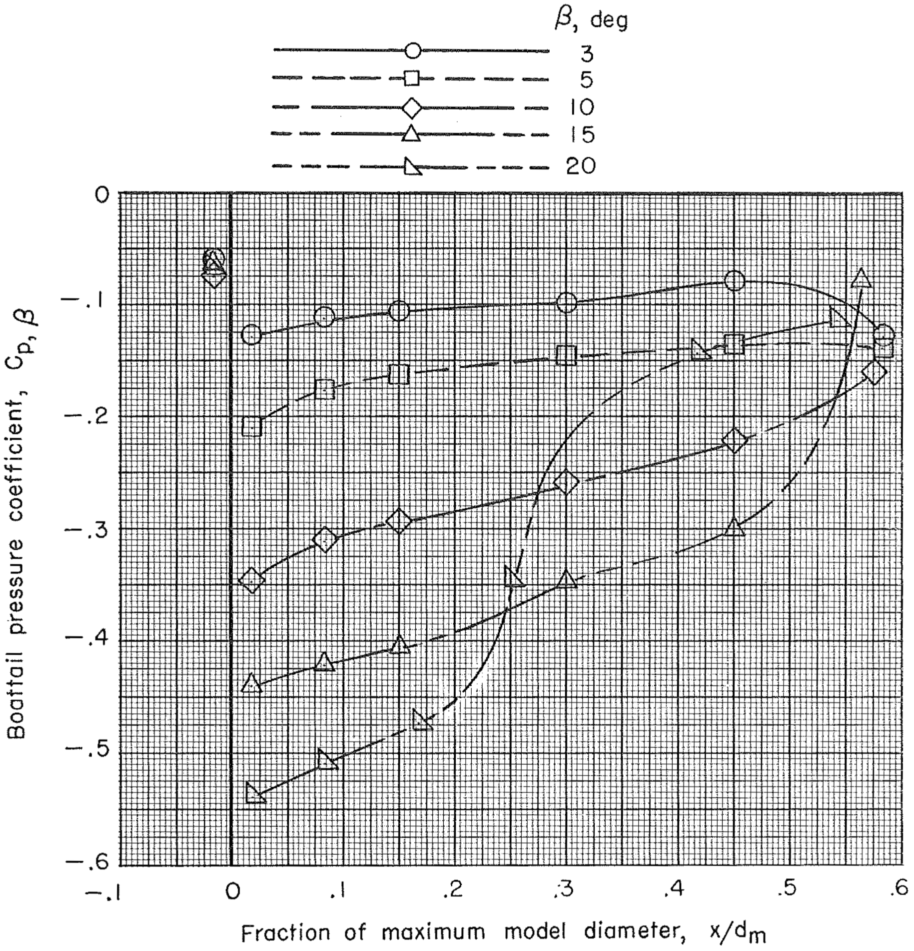

(c) M = 1.30.

Figure 6.- Concluded.

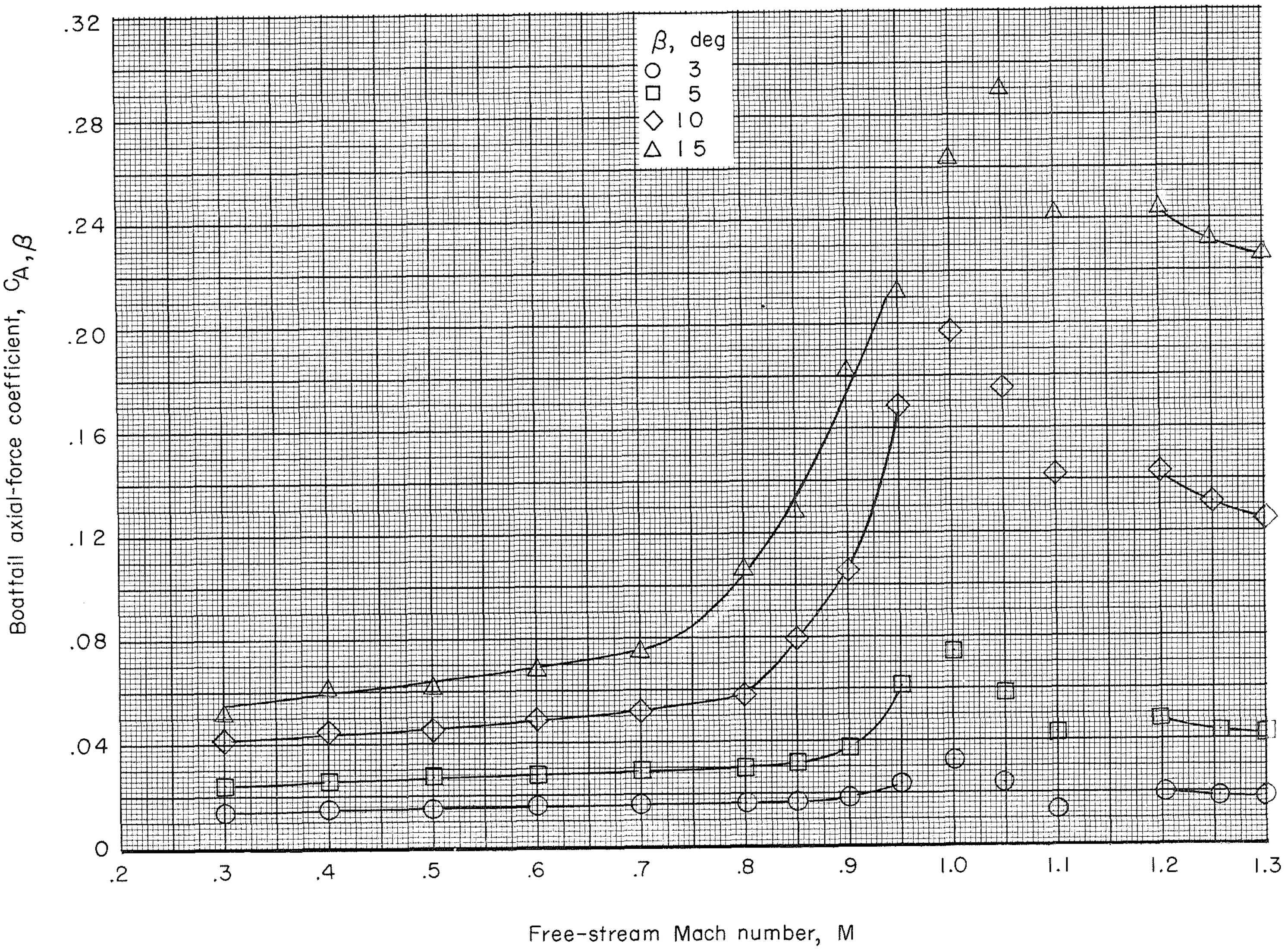

(a) $l/d_m = 1.0$.

Figure 7.- Variation of boattail axial-force coefficient with free-stream Mach number for all conical boattails. Jet off.

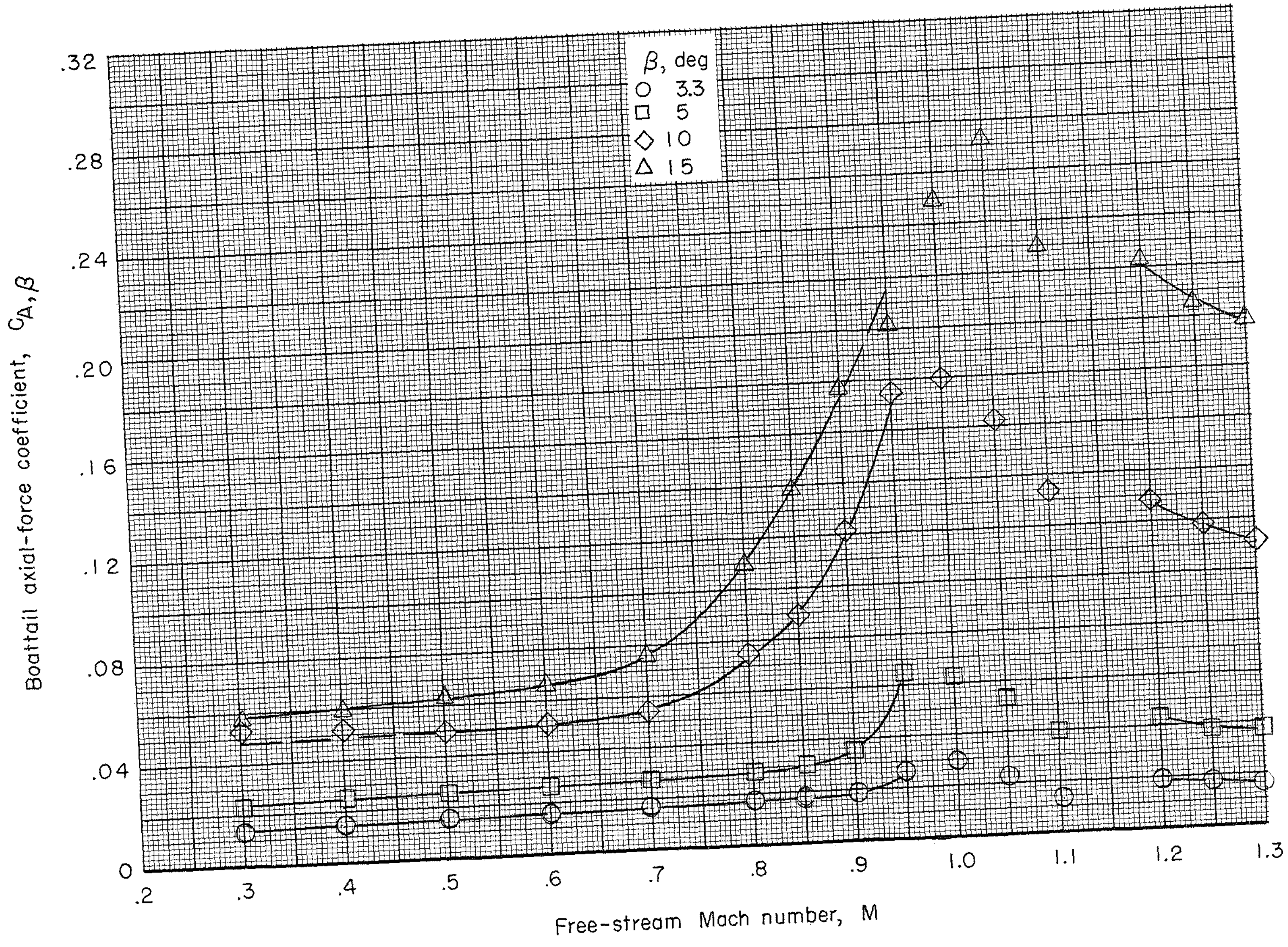

(b) $l/d_m = 0.8$.

Figure 7.- Continued.

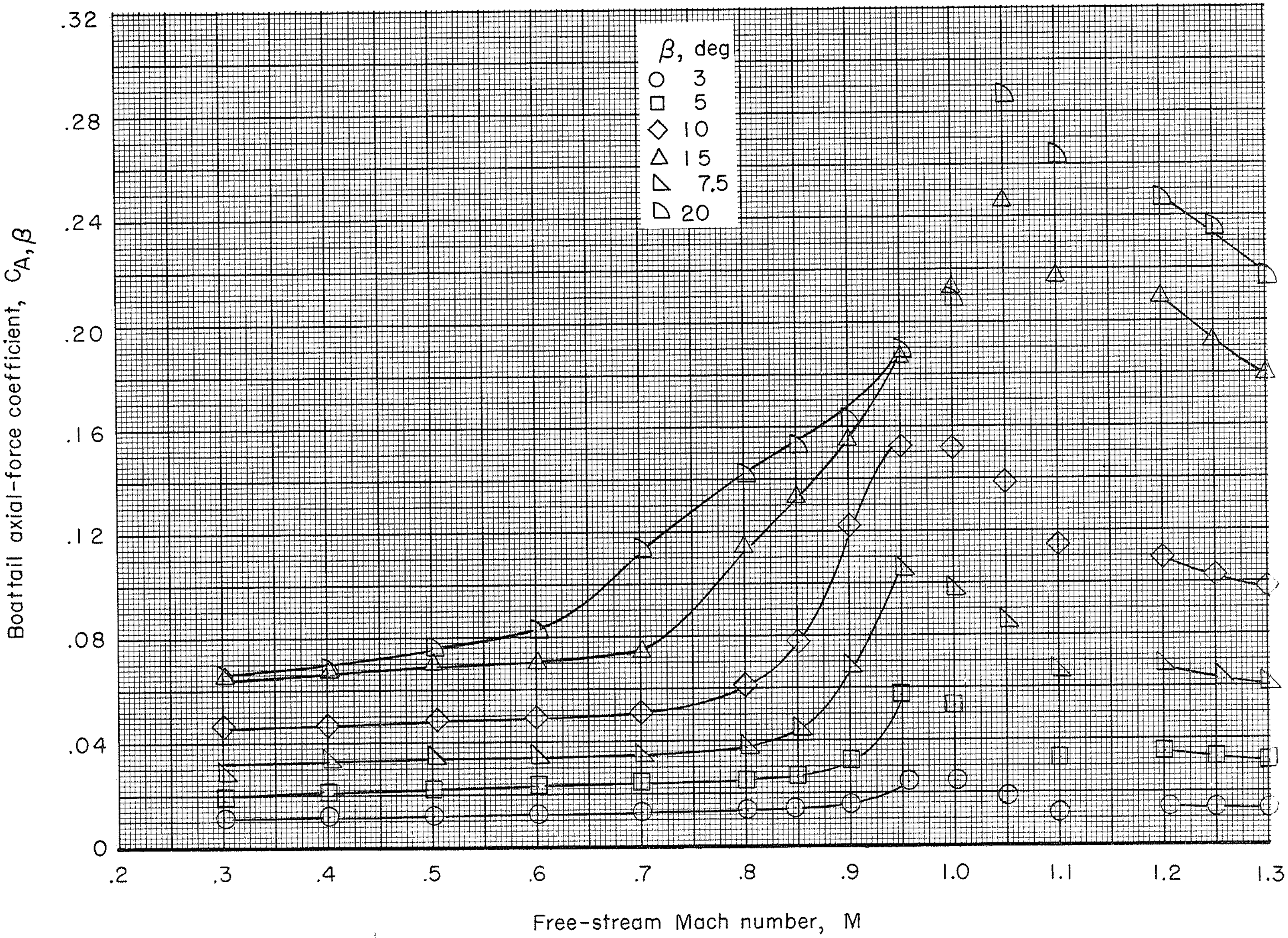

(c) $l/d_m = 0.6$.

Figure 7.- Continued.

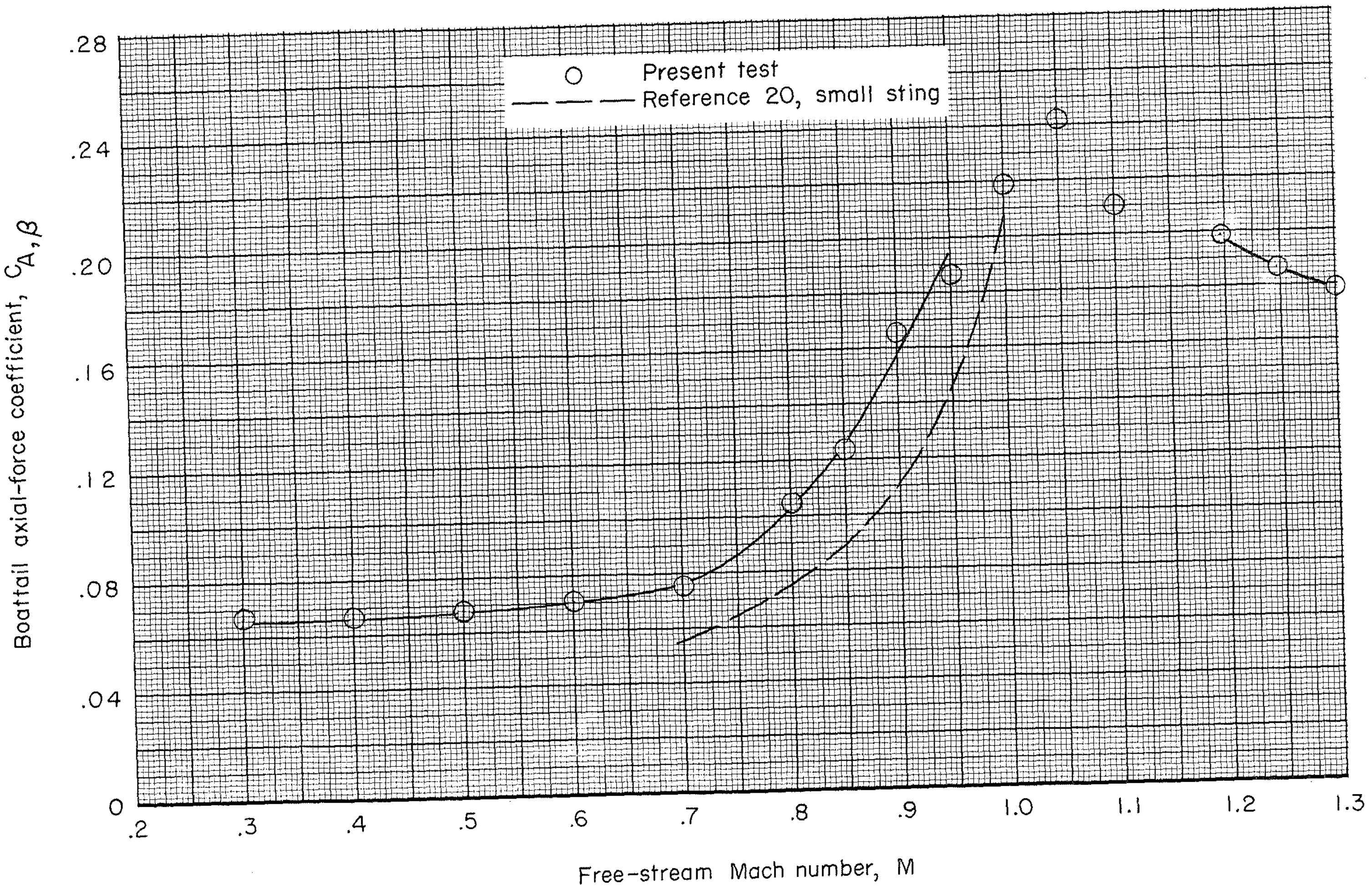

(d) $l/d_m = 0.638$; $\beta = 15^0$.

Figure 7.- Concluded.

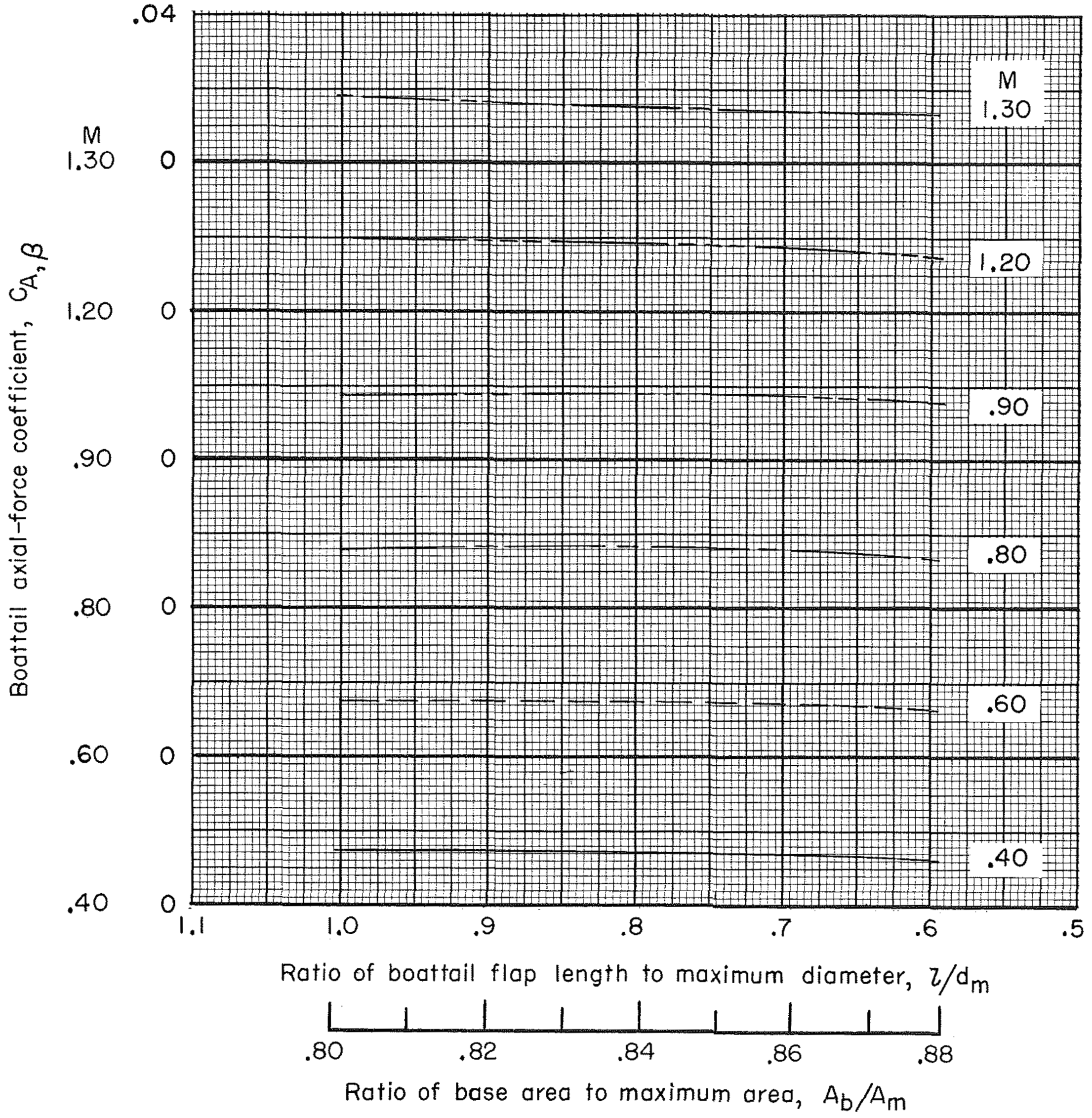

(a) $\beta \approx 3^{\circ}$.

Figure 8.- Variation of boattail axial-force coefficient with ratio of boattail flap length to maximum diameter. Jet off.

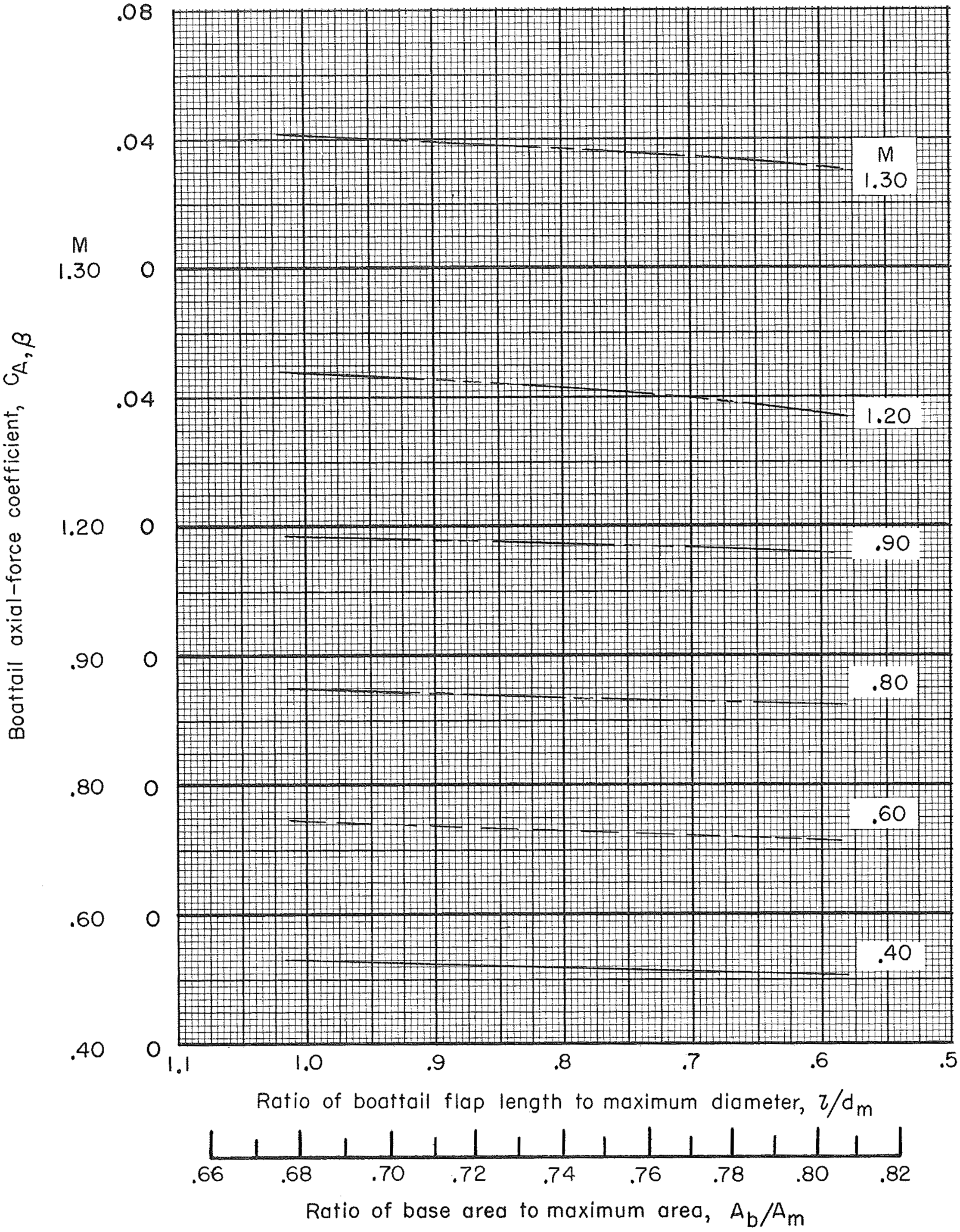

(b) $\beta = 5^0$.

Figure 8.- Continued.

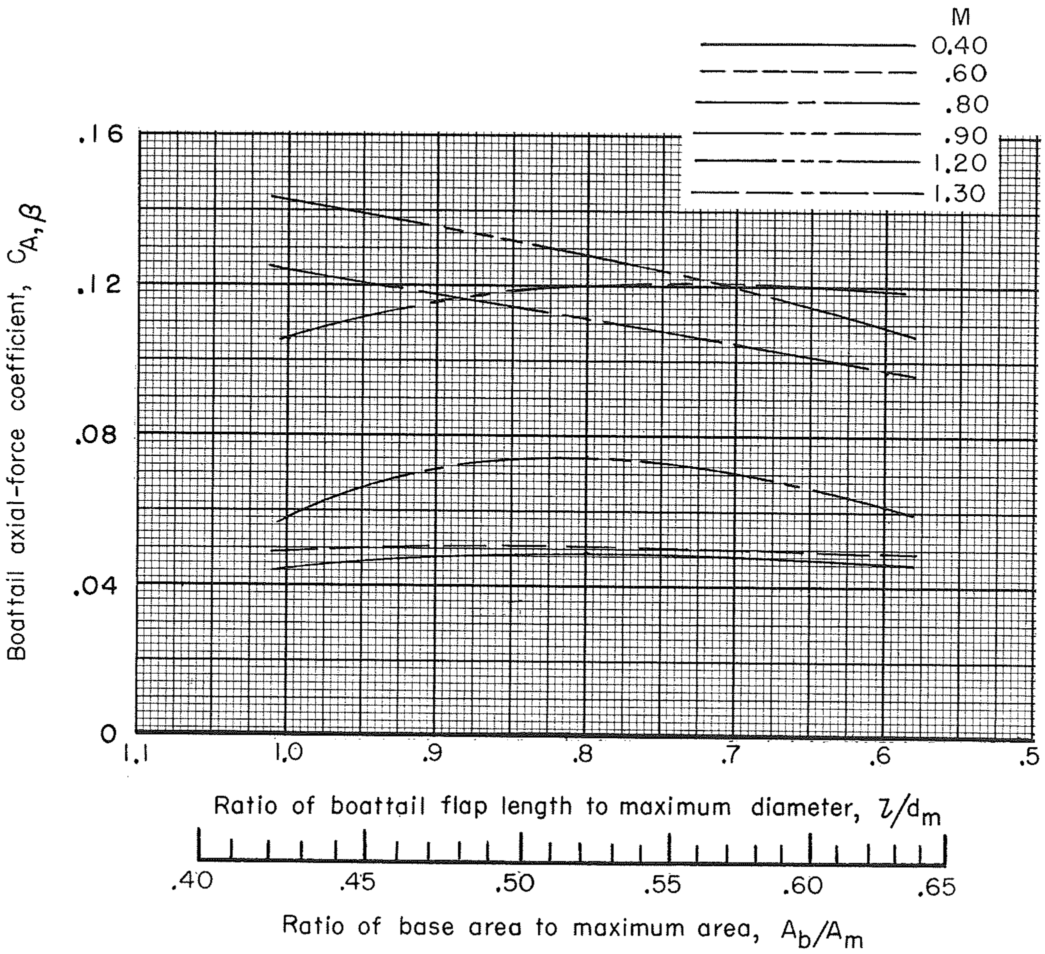

(c) $\beta = 10^{\circ}$.

Figure 8.- Continued.

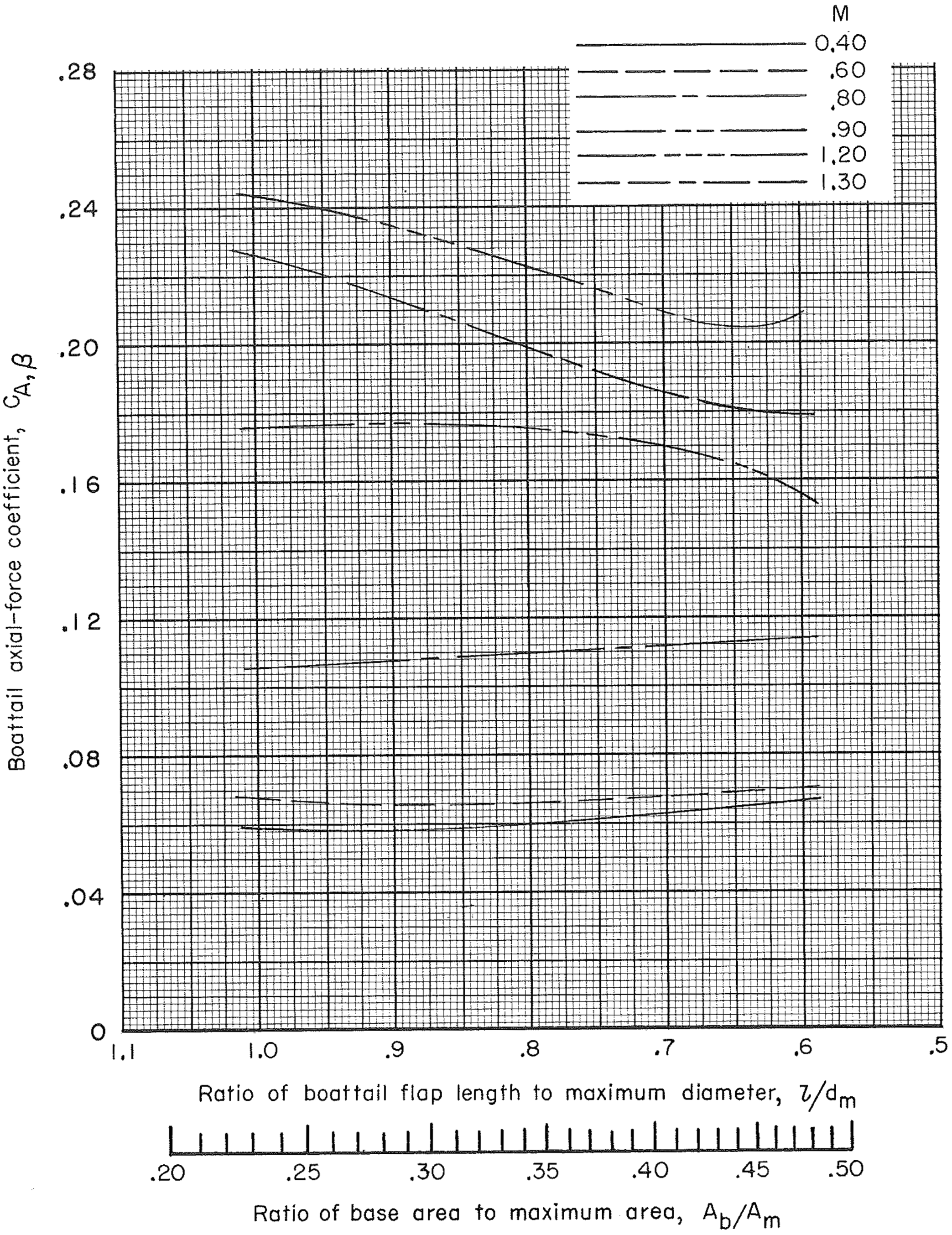

(d) $\beta = 15^0$.

Figure 8.- Concluded.

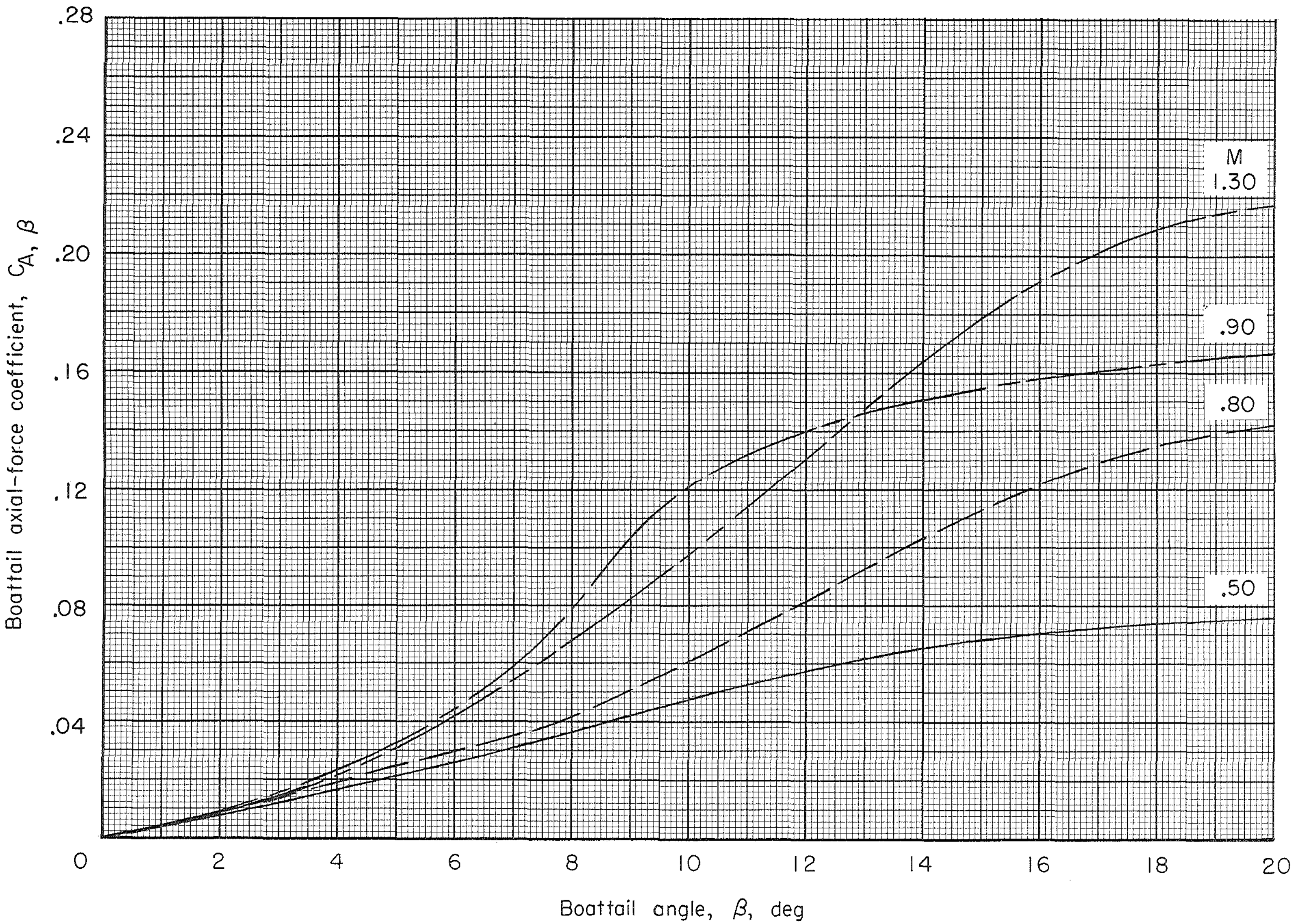

Figure 9.- Variation of boattail axial-force coefficient with boattail angle. $l/d_m = 0.6$; jet off.

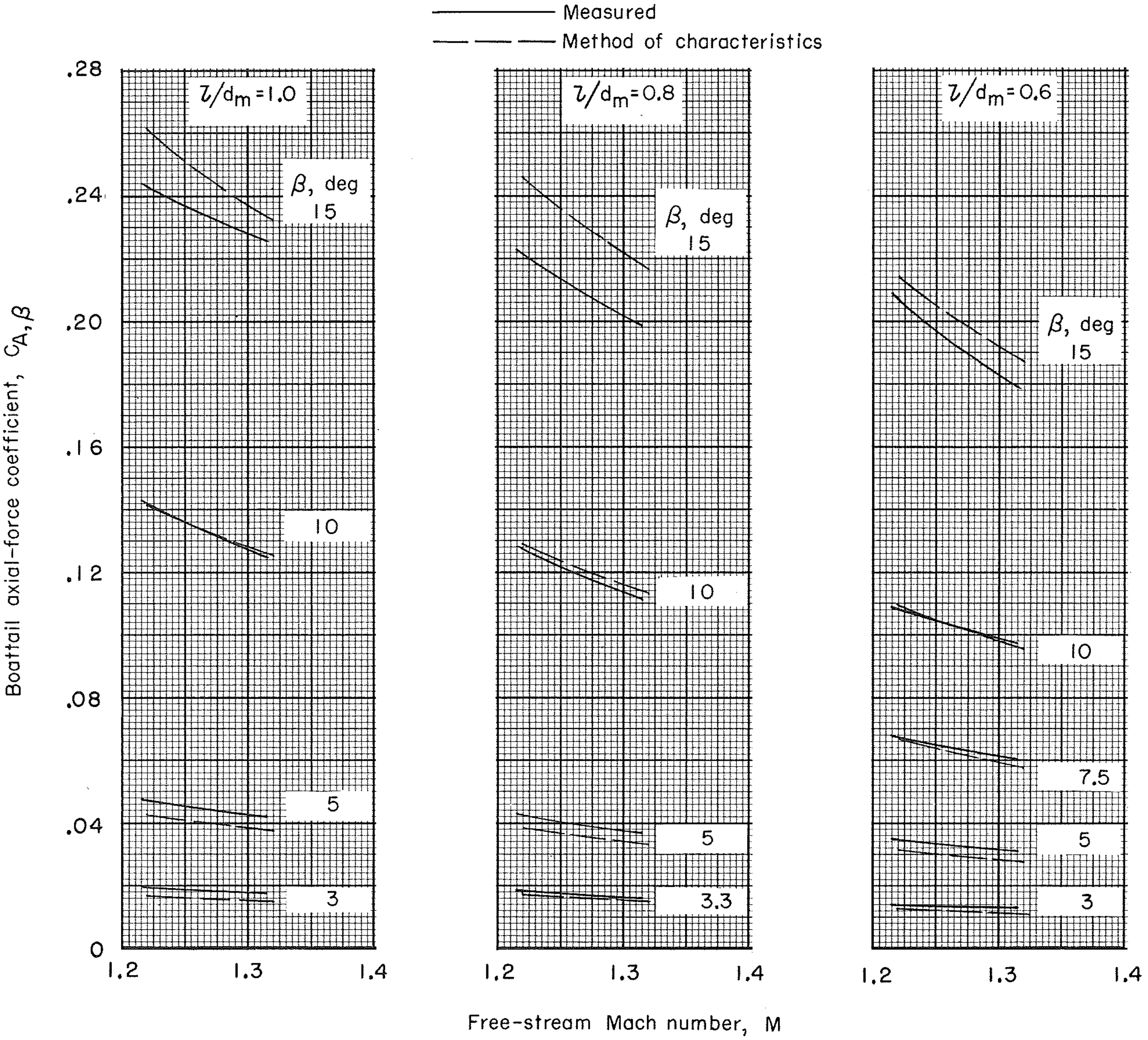

Figure 10.- Comparison of boattail axial-force coefficients with those computed by method of characteristics. Jet off.

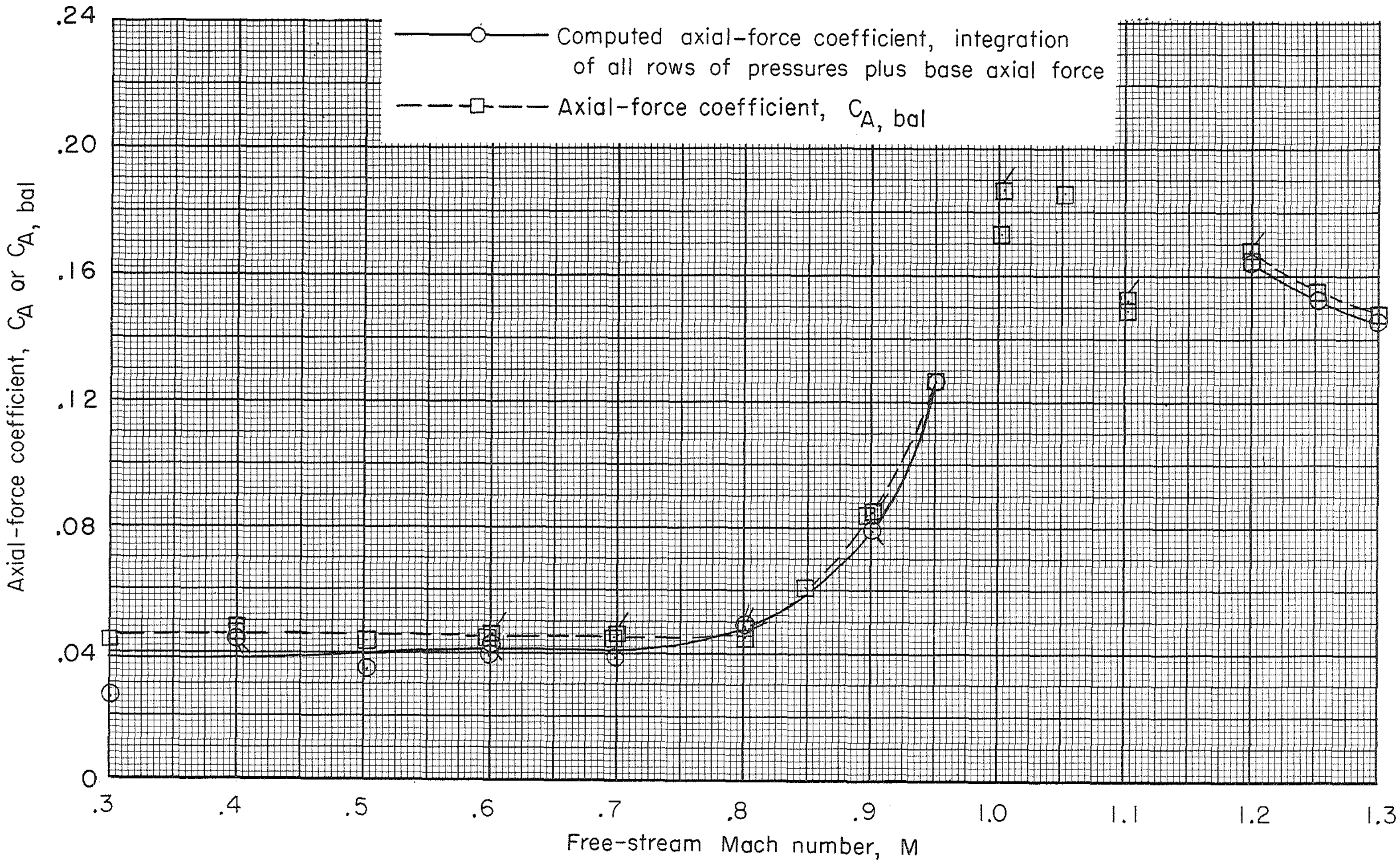

Figure 11.- Comparison of pressure and force measurements. $\beta = 10^0$; $l/d_m = 1.0$; jet off. (Flagged symbols indicate data taken as free-stream Mach number was decreased.)

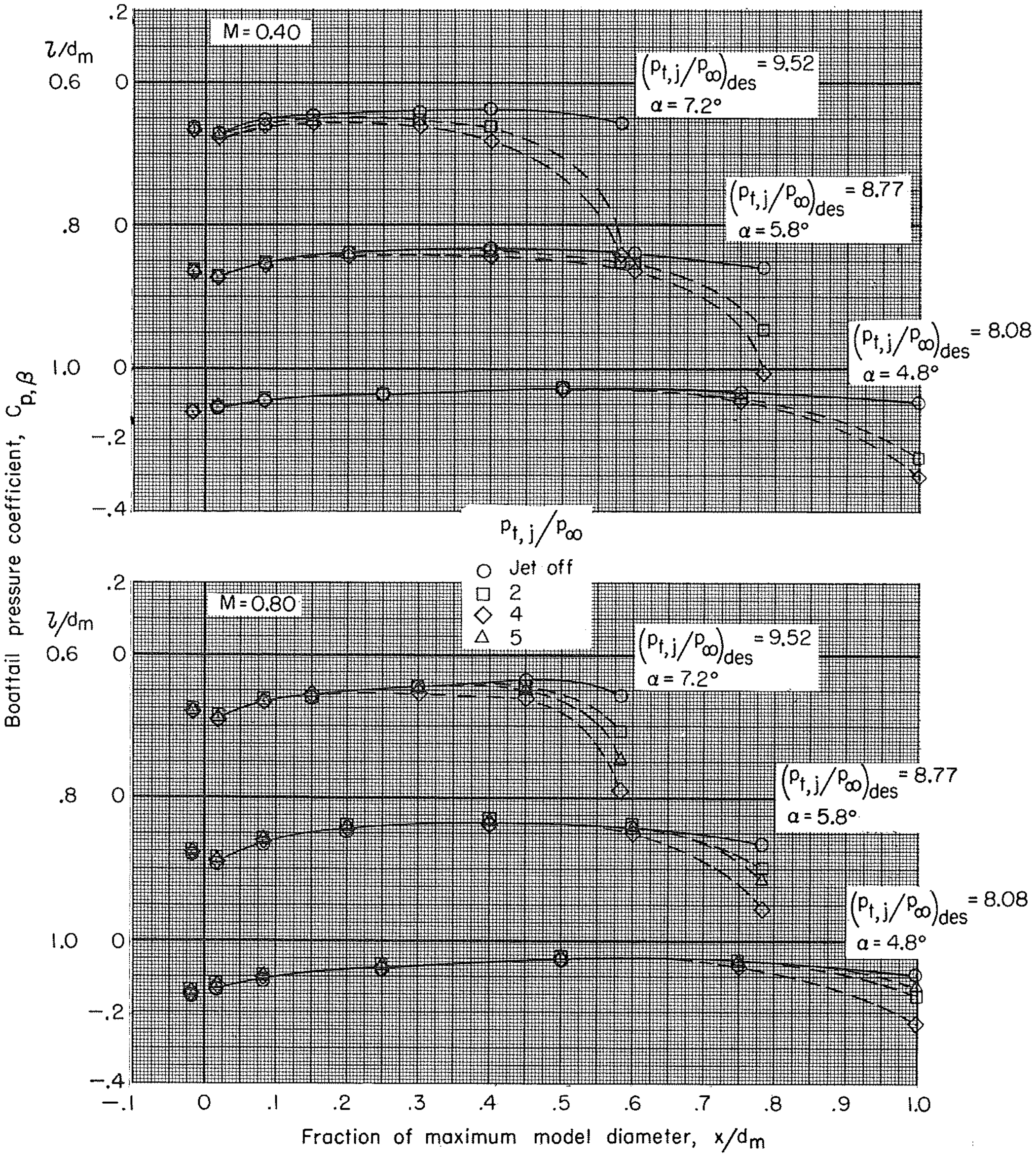

(a) $\beta \approx 3^0$.

Figure 12.- Effect of jet total-pressure ratio on boattail pressure-coefficient distributions for all conical boattails.

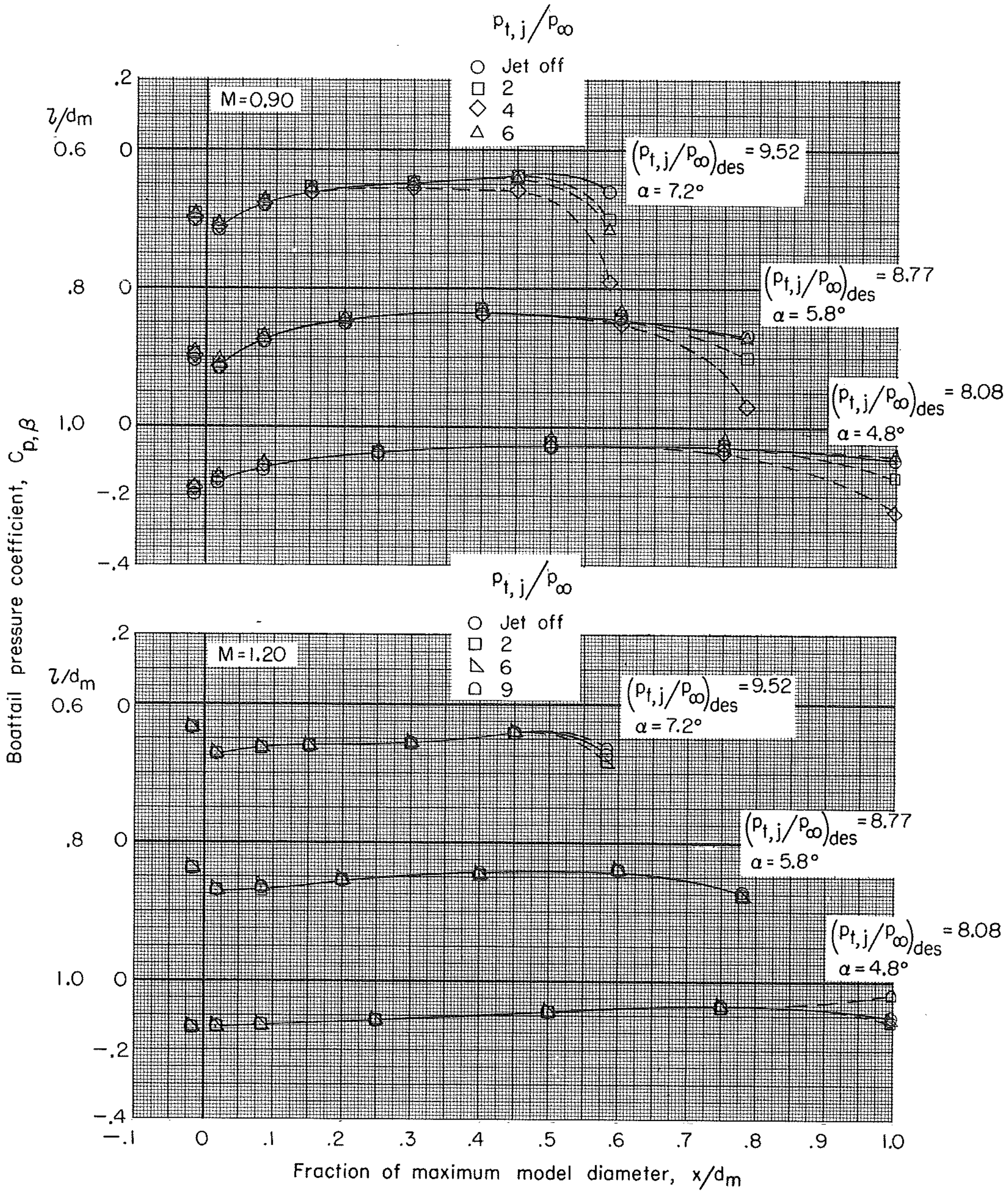

(a) β ≈ 3°. Concluded.

Figure 12.- Continued.

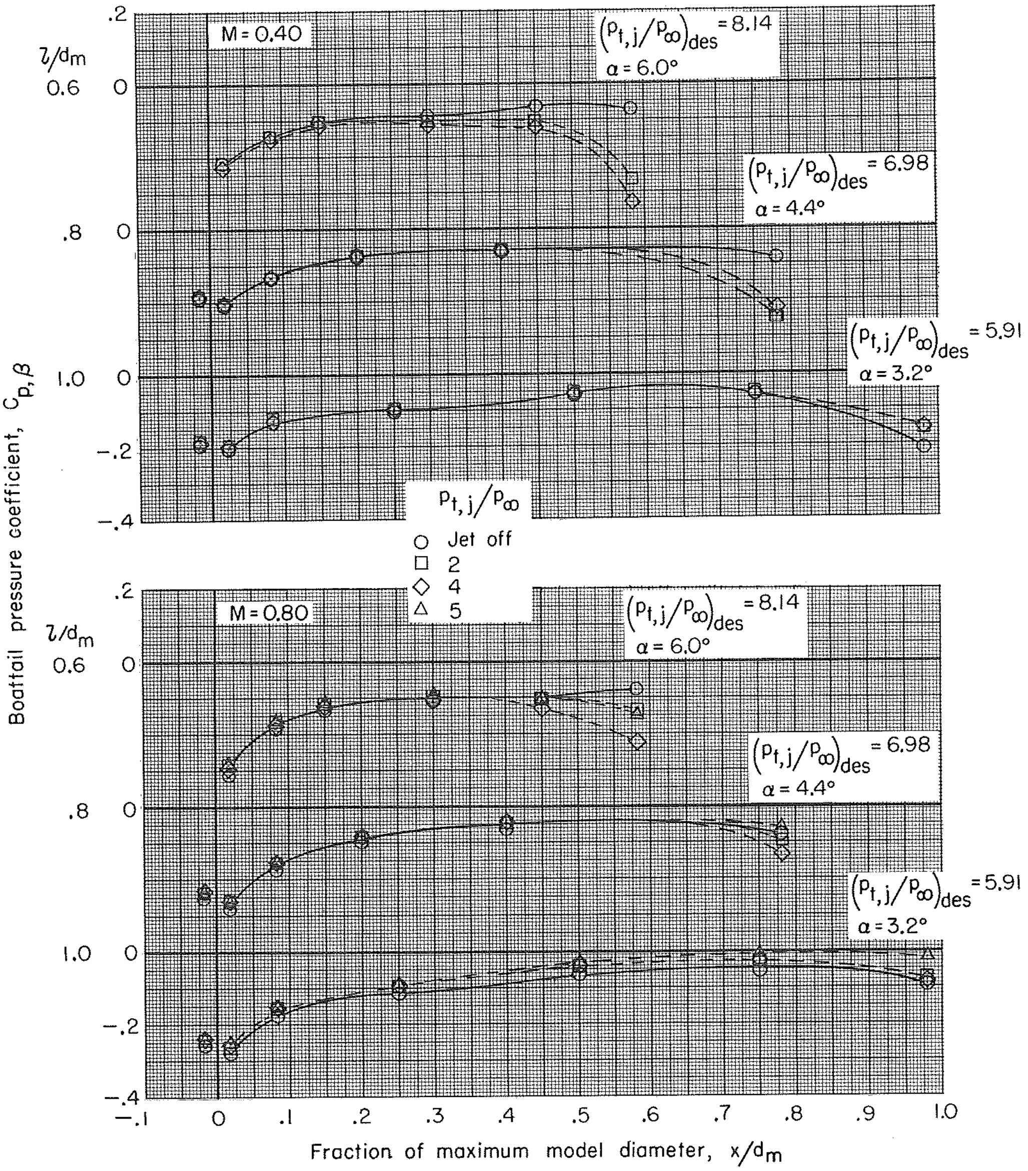

(b) $\beta = 5^0$.

Figure 12.- Continued.

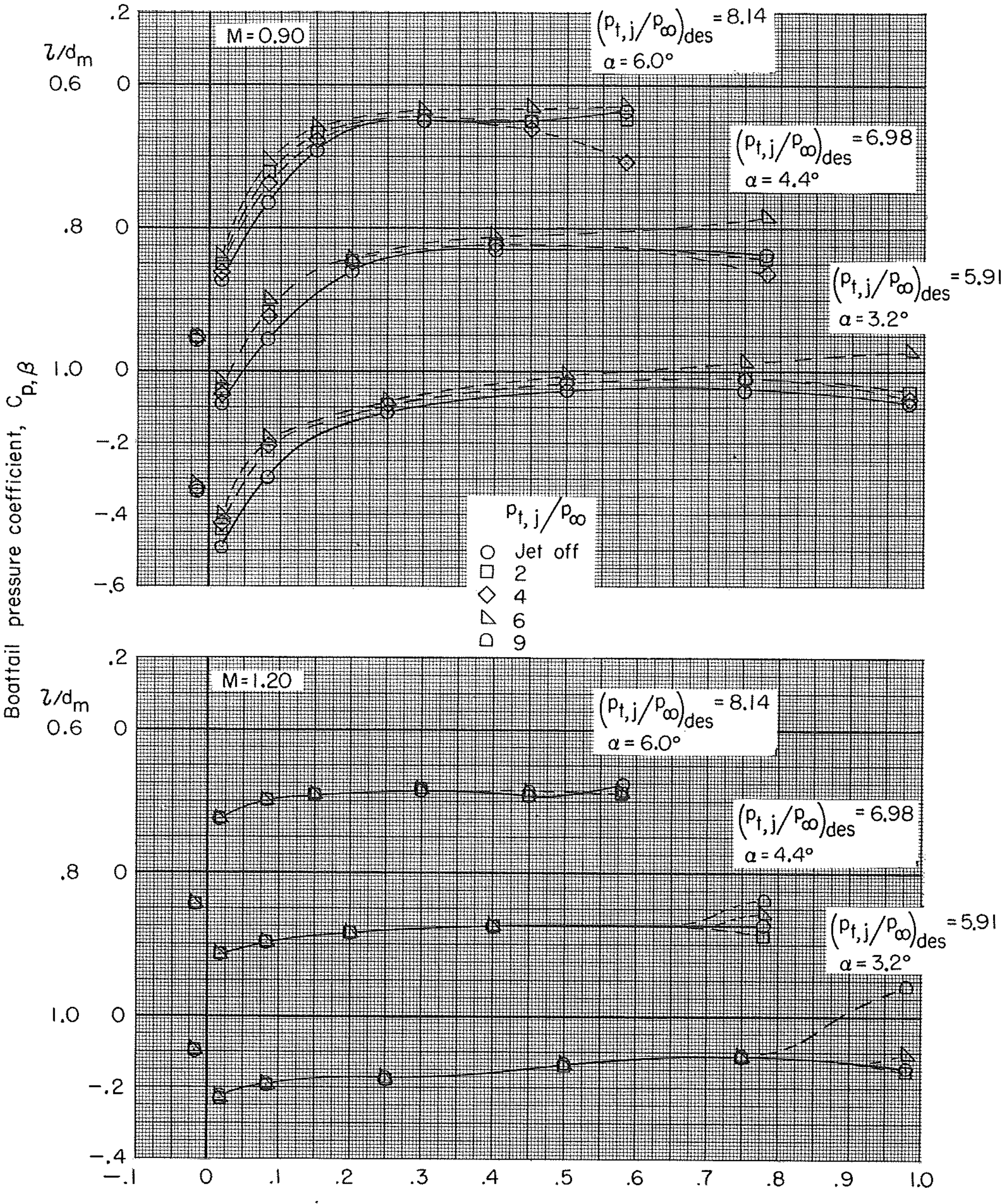

(b) $\beta = 5^0$. Concluded.

Figure 12.- Continued.

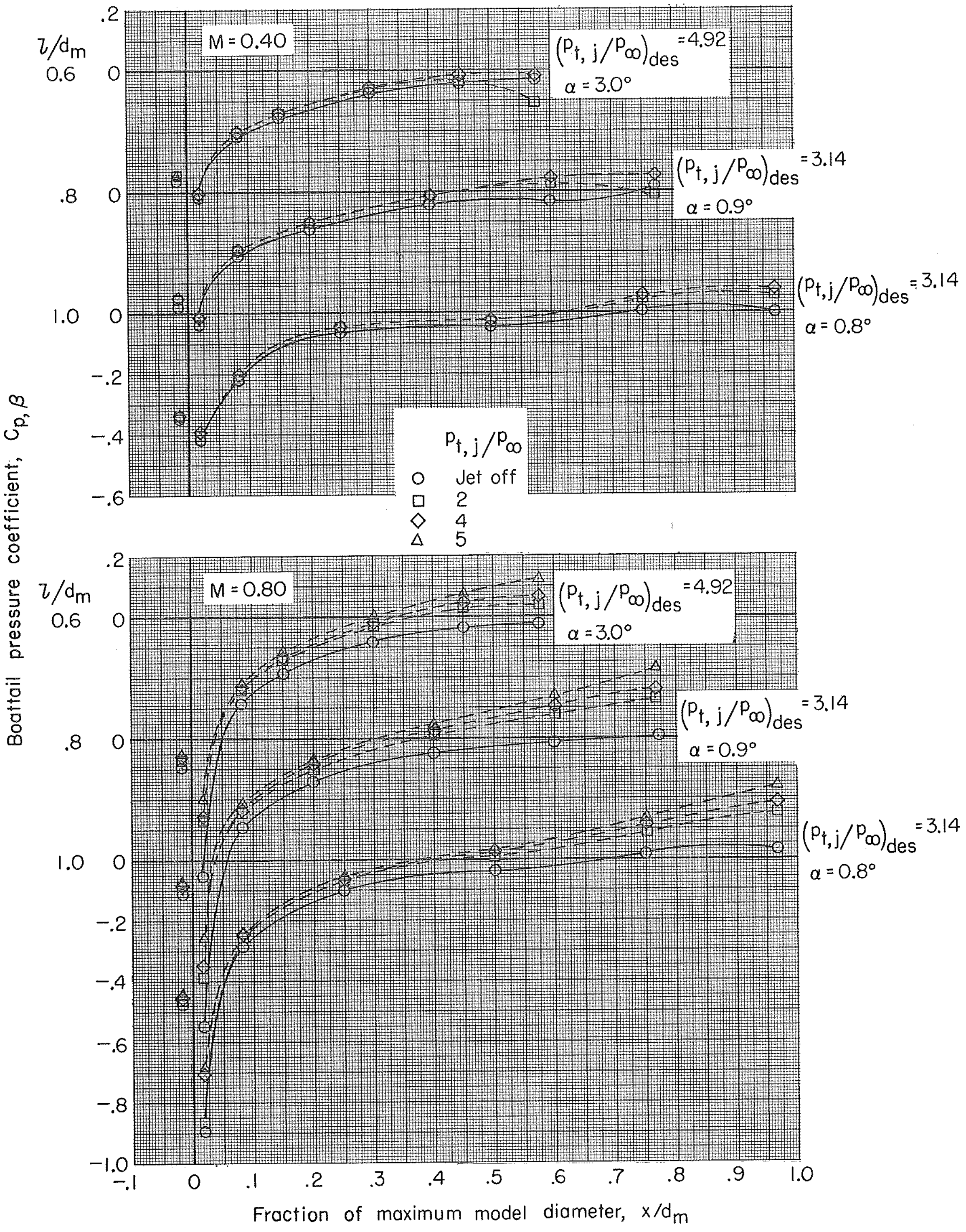

(c) $\beta = 10^0$.

Figure 12.- Continued.

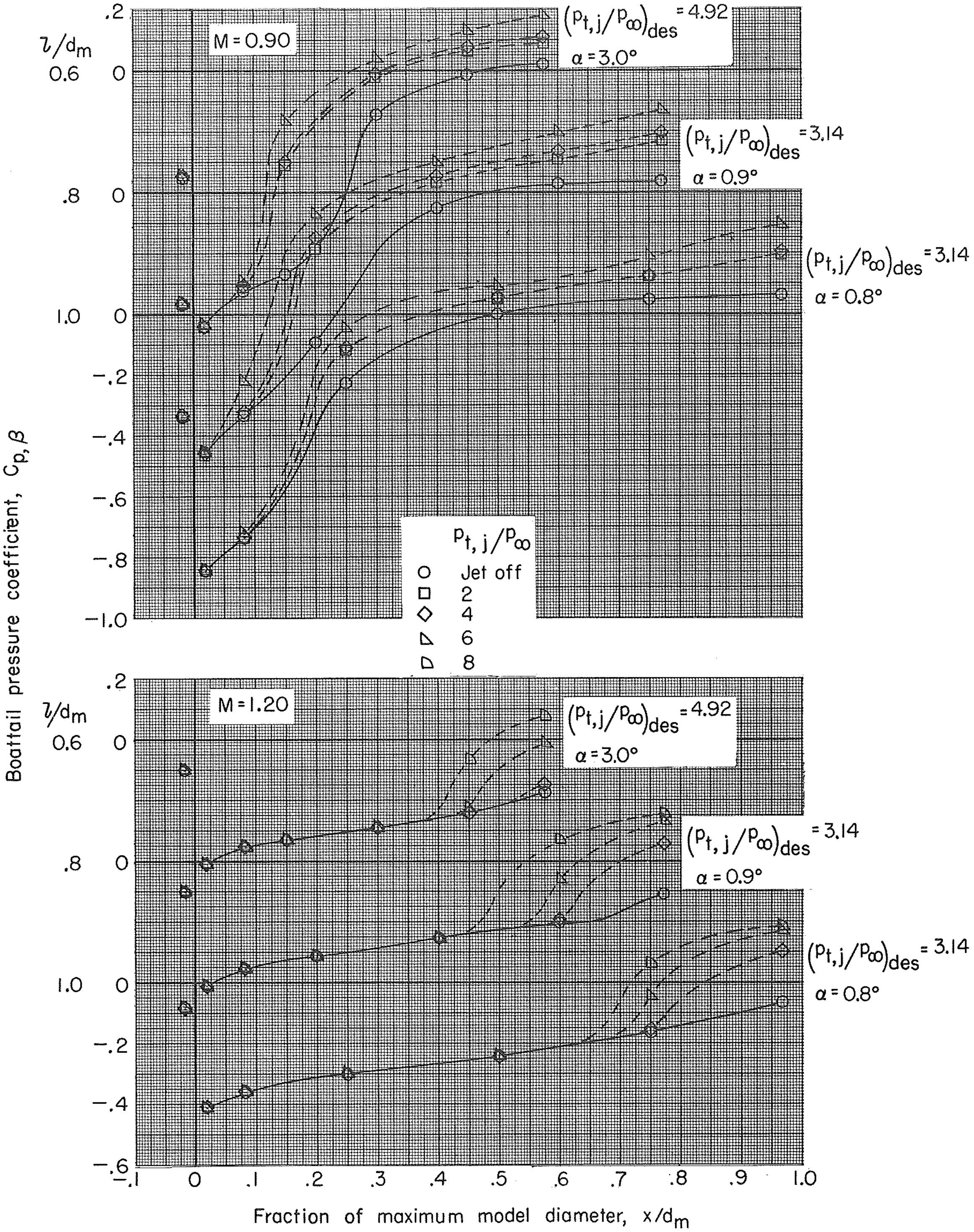

(c) β = 10°. Concluded.

Figure 12.- Continued.

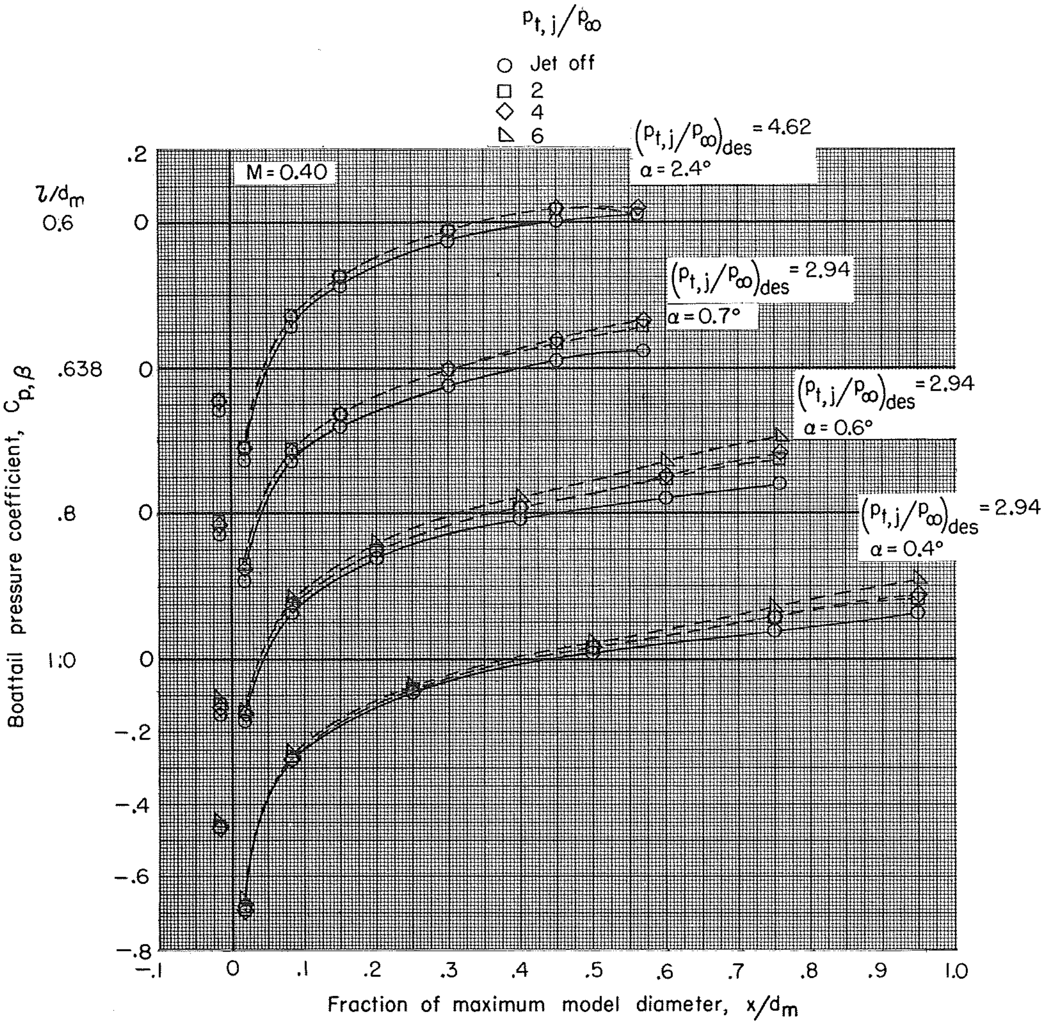

(d) β = 15°.

Figure 12.- Continued.

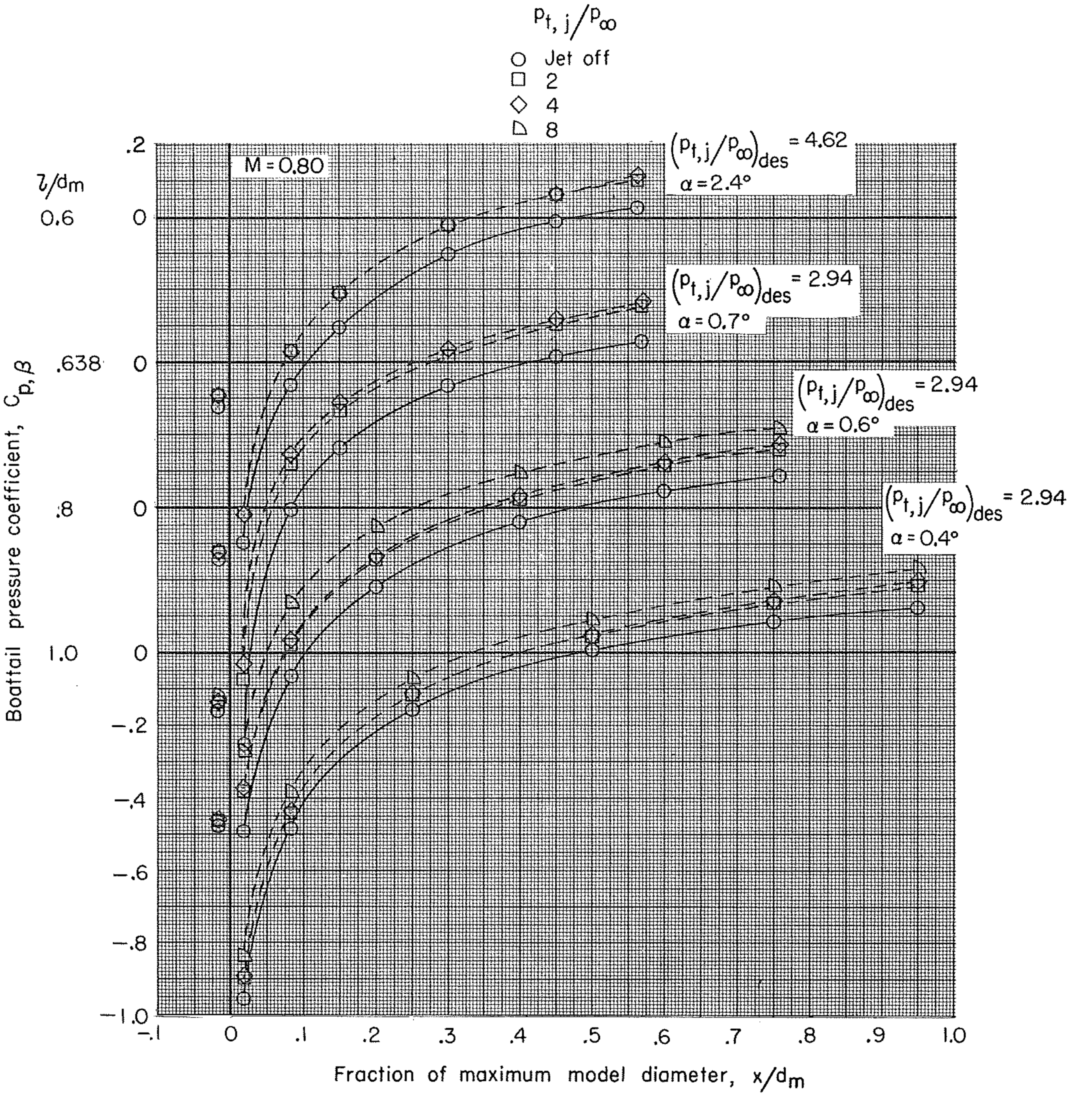

(d) β = 15°. Continued.

Figure 12.- Continued.

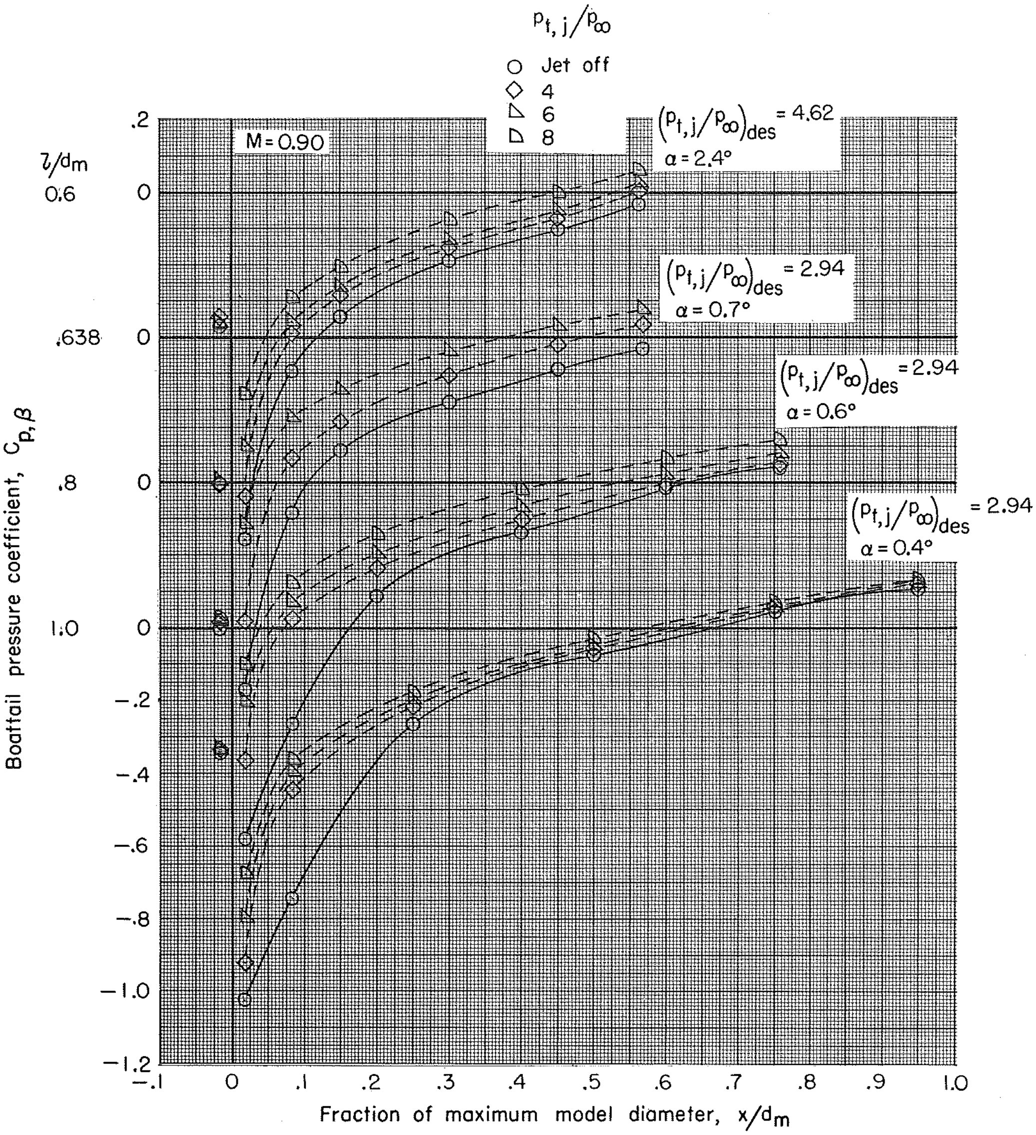

(d) $\beta = 15^0$. Continued.

Figure 12.- Continued.

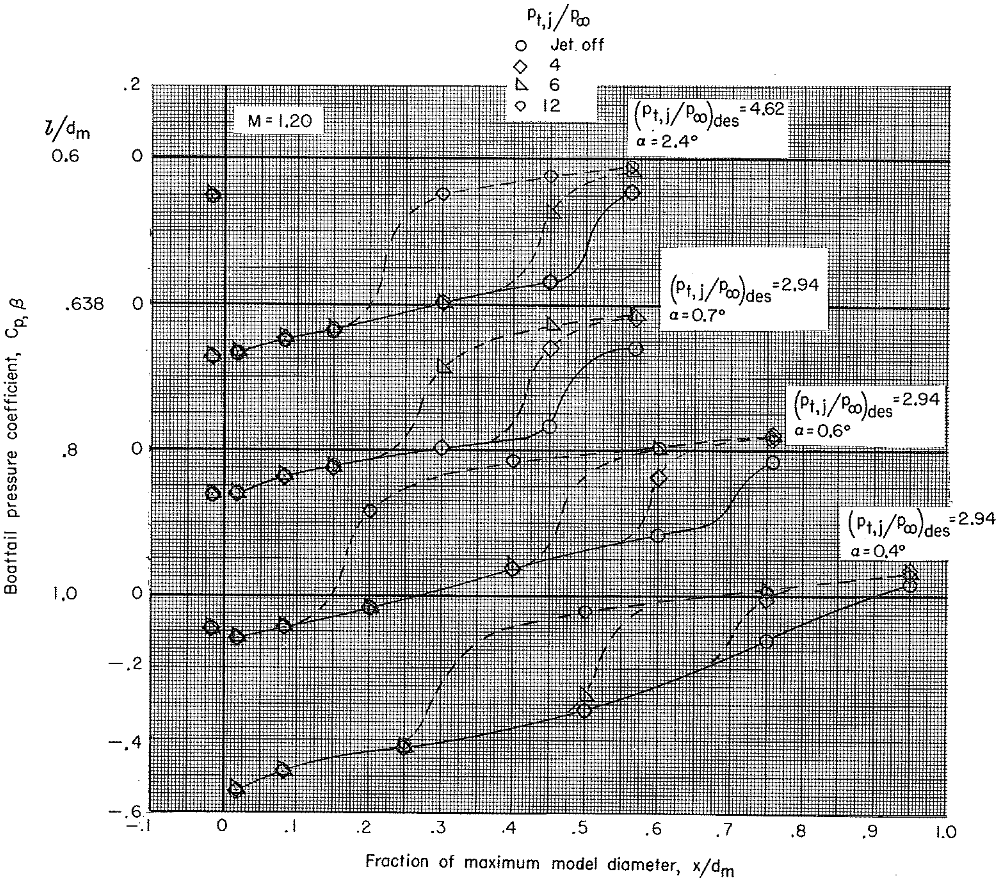

(d) β = 15°. Concluded.

Figure 12.- Continued.

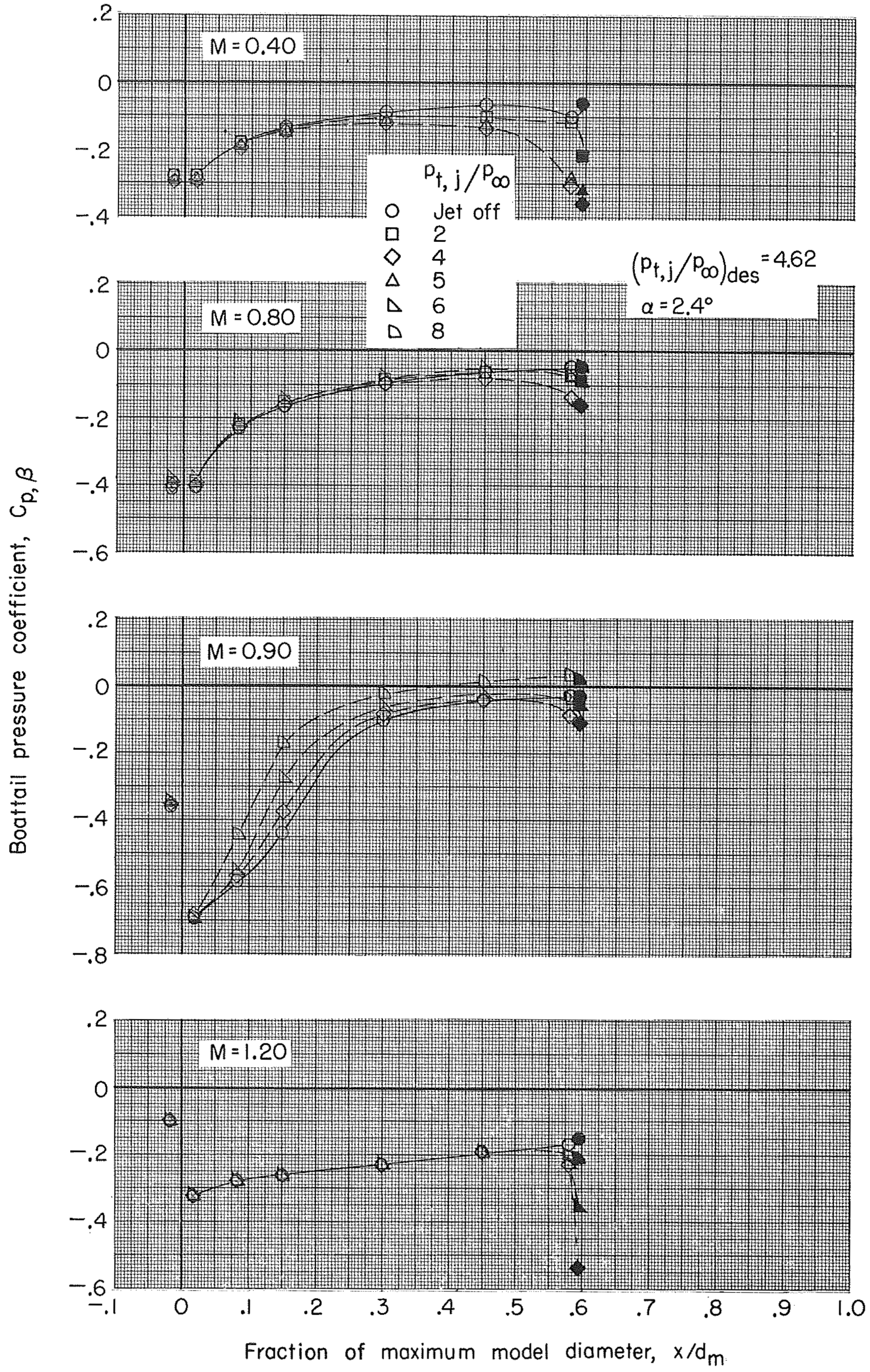

(e) $\beta = 7.5^0$; $l/d_m = 0.6$. (Solid symbols indicate base pressures.)

Figure 12.- Continued.

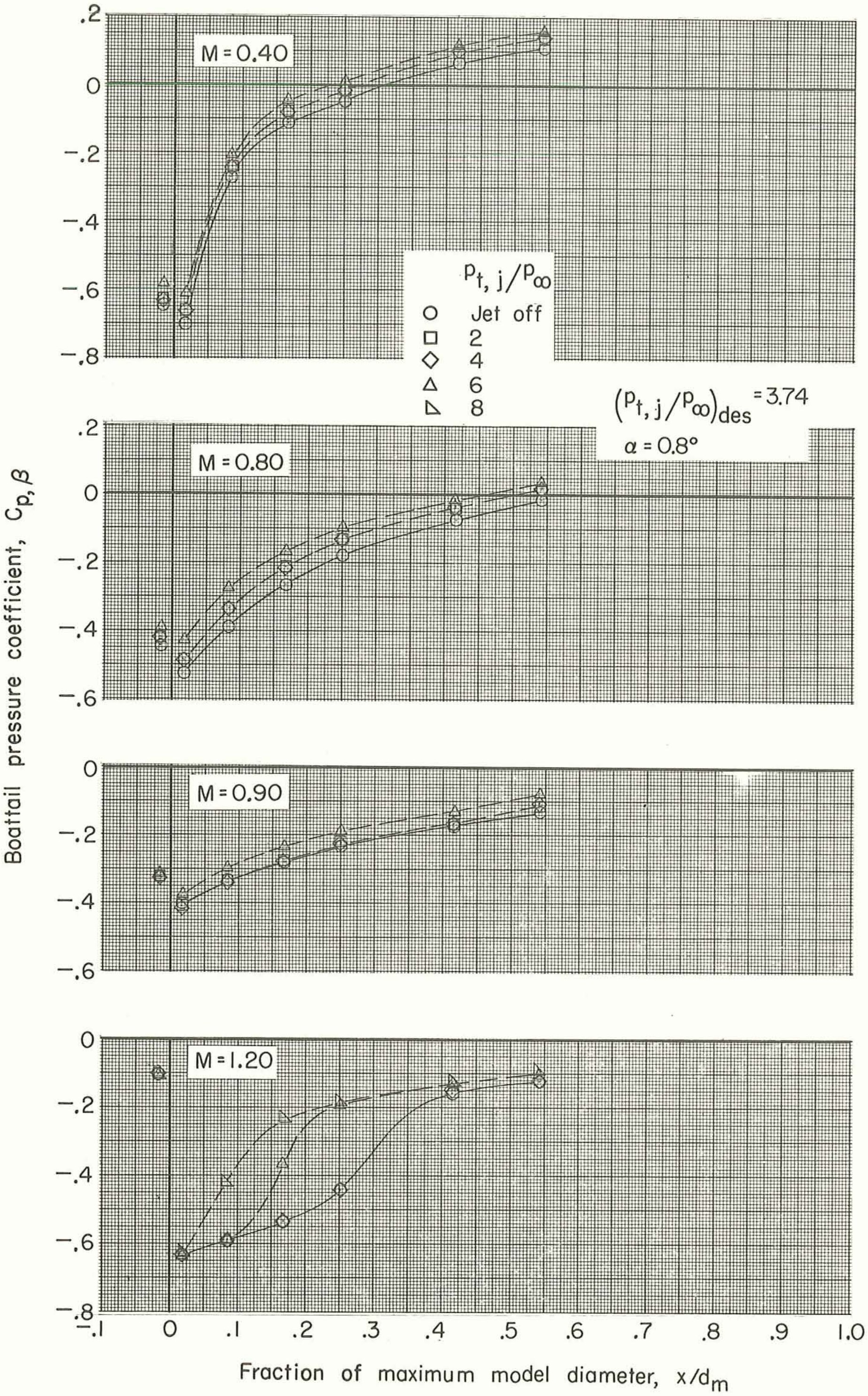

(f) $\beta = 20^0$; $l/d_m = 0.6$.

Figure 12.- Concluded.

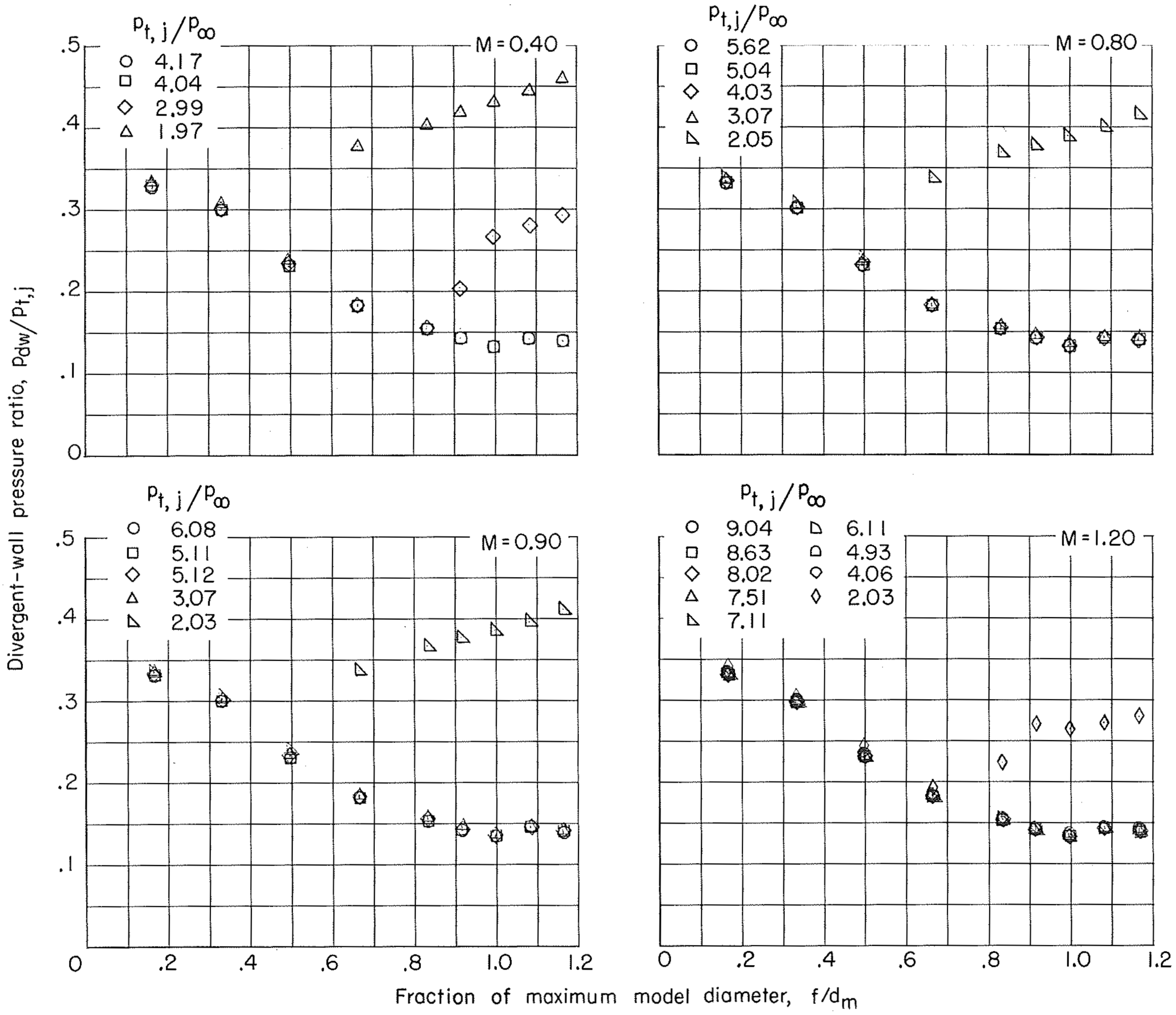

(a) $\beta = 3^0$; $l/d_m = 1.0$.

Figure 13.- Typical nozzle internal-pressure distributions for various total-pressure ratios and free-stream Mach numbers.

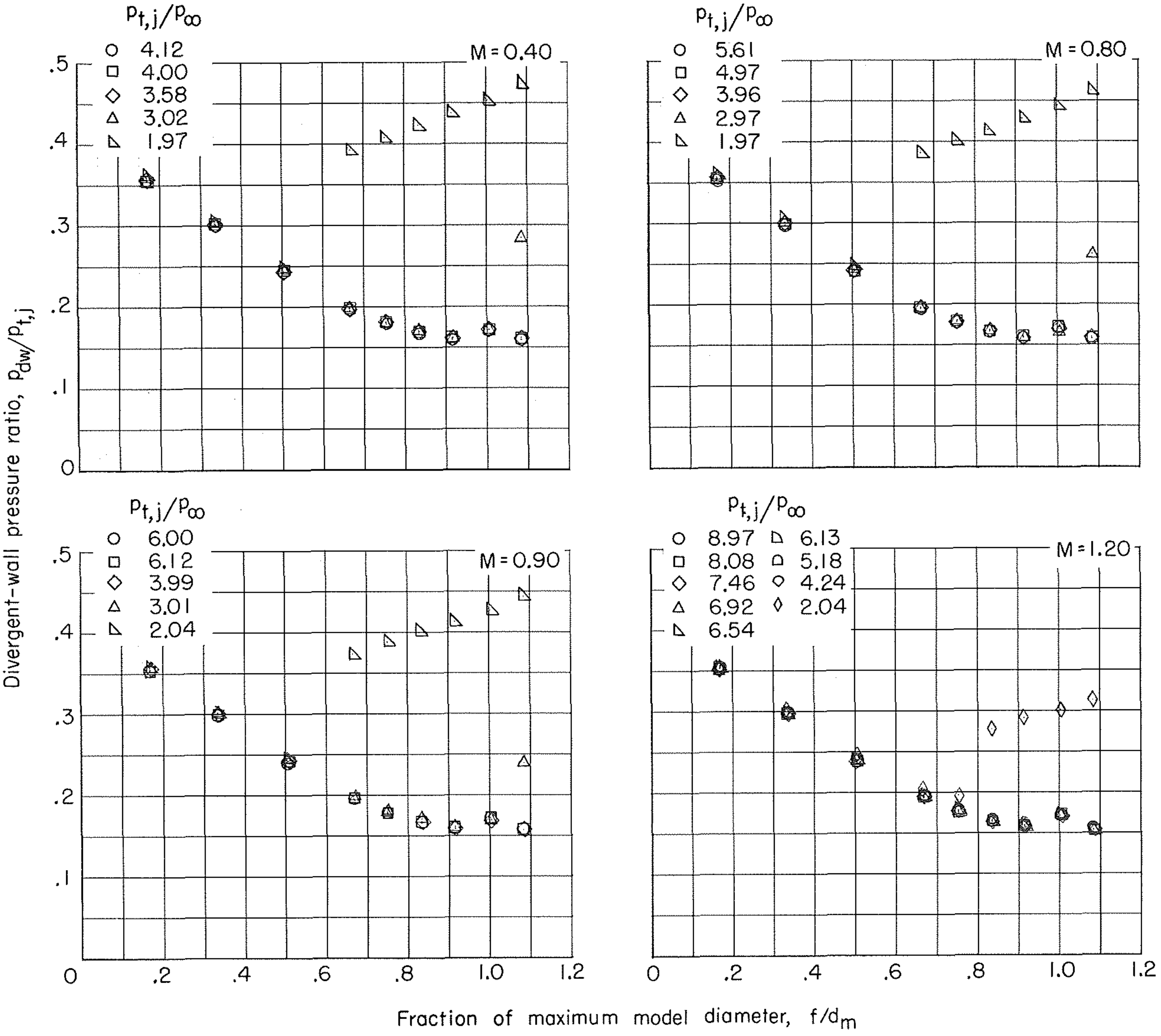

(b) $\beta = 5^{\circ}$; $l/d_m = 0.8$.

Figure 13.- Continued.

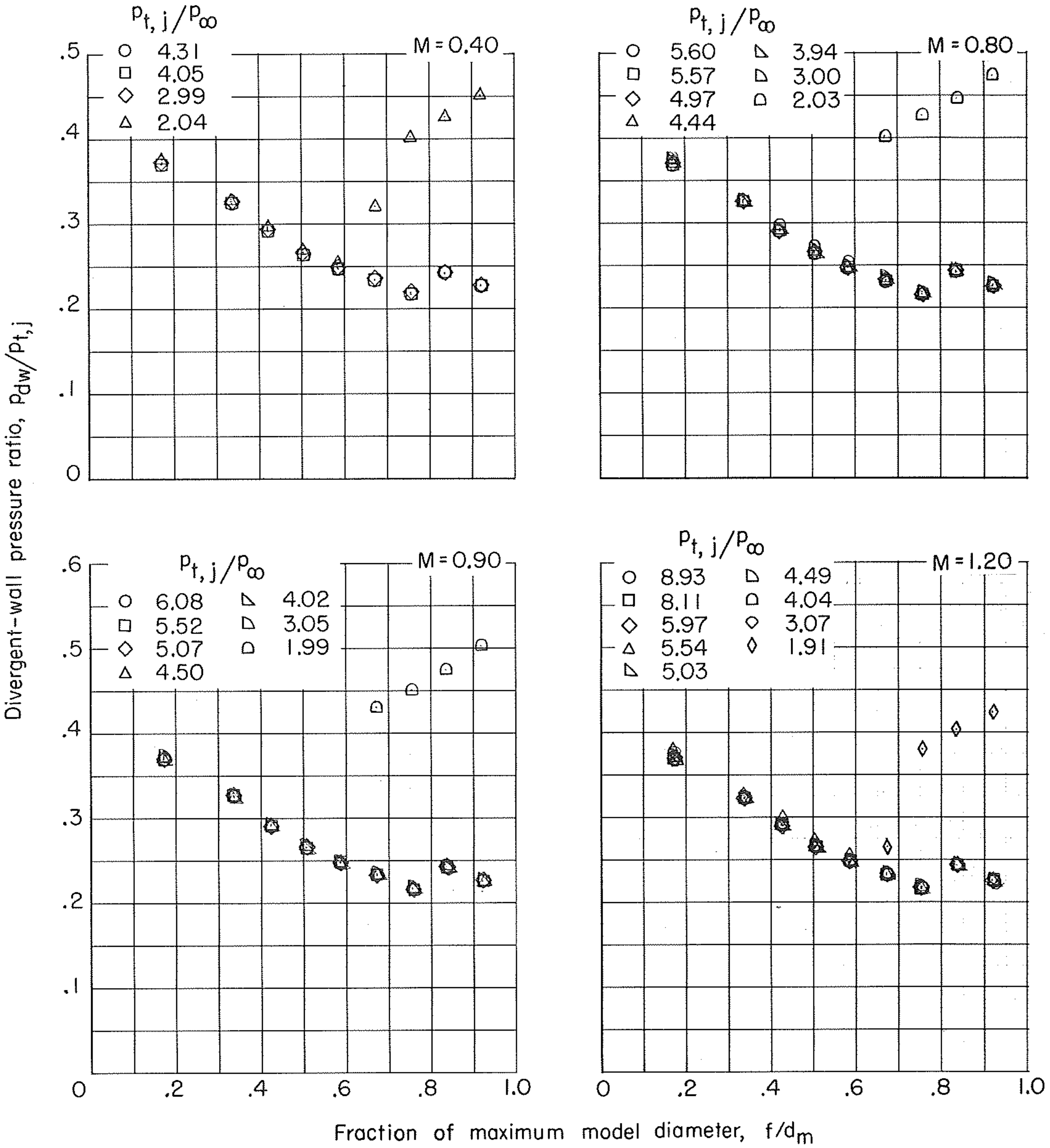

(c) $\beta = 10^0$; $l/d_m = 0.6$.

Figure 13.- Continued.

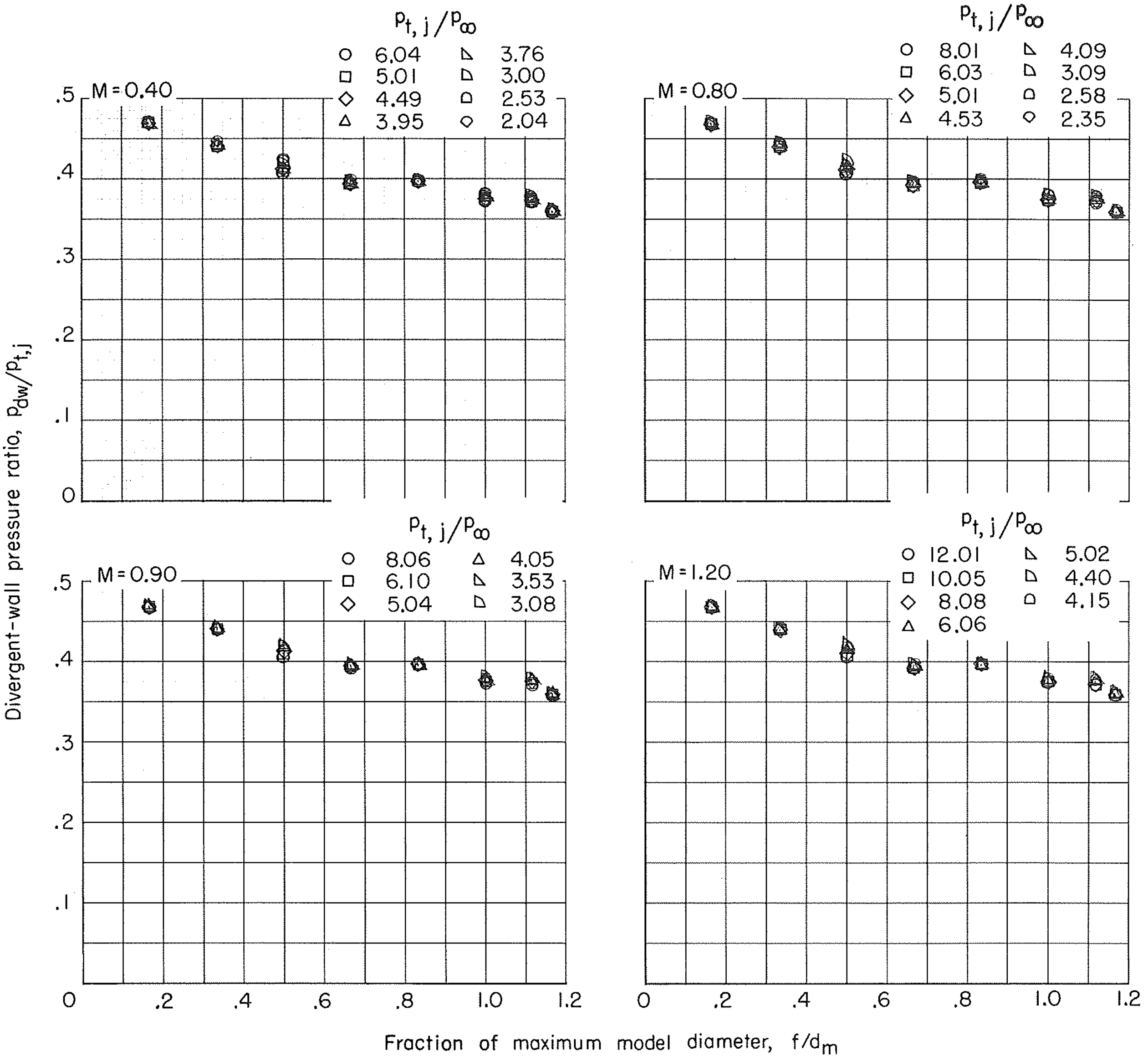

(d) $\beta = 15^0$; $l/d_m = 1.0$.

Figure 13.- Continued.

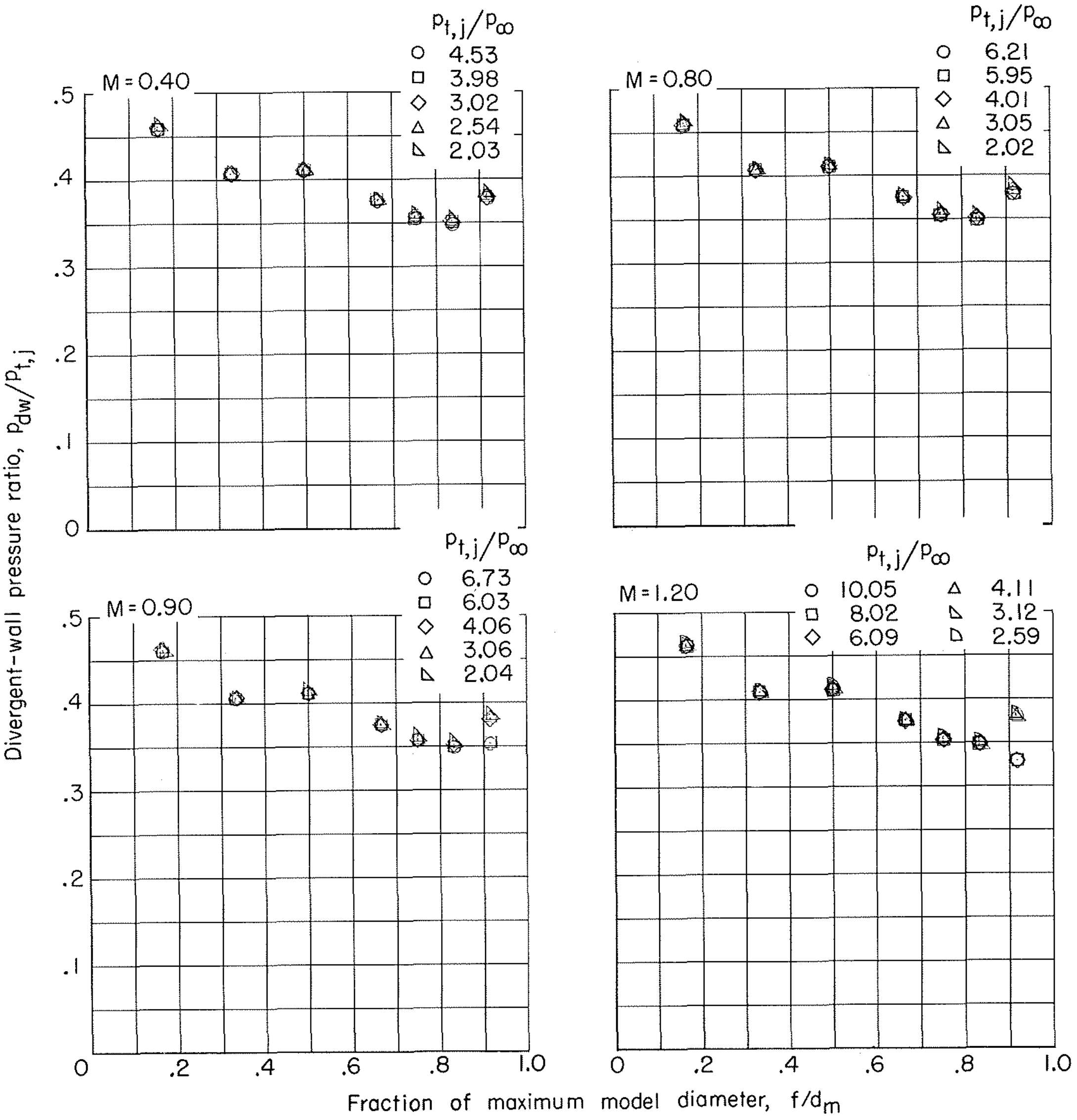

(e) $\beta = 15^0$; $l/d_m = 0.638$.

Figure 13.- Continued.

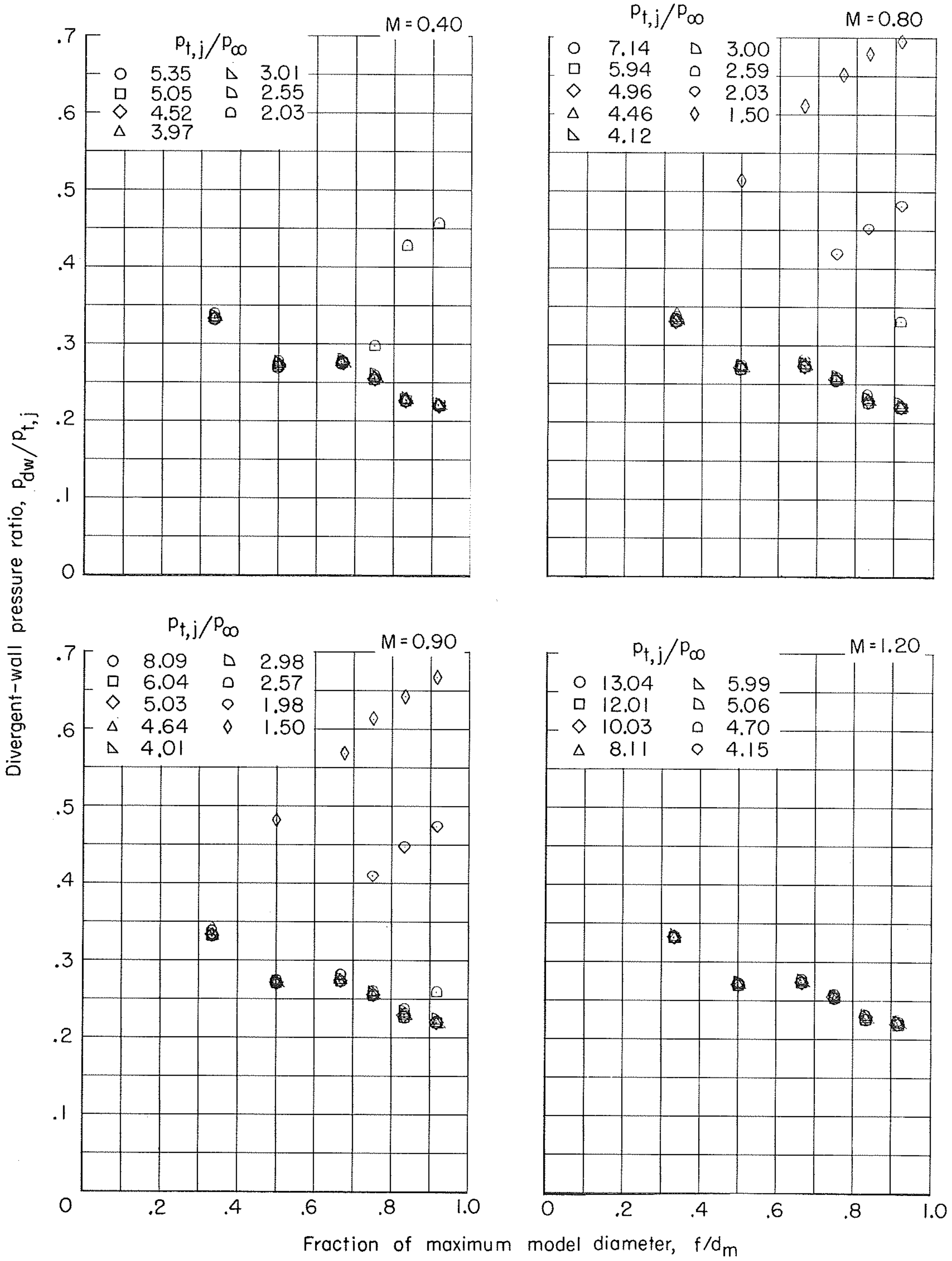

(f) $\beta = 15^0$; $l/d_m = 0.6$.

Figure 13.- Concluded.

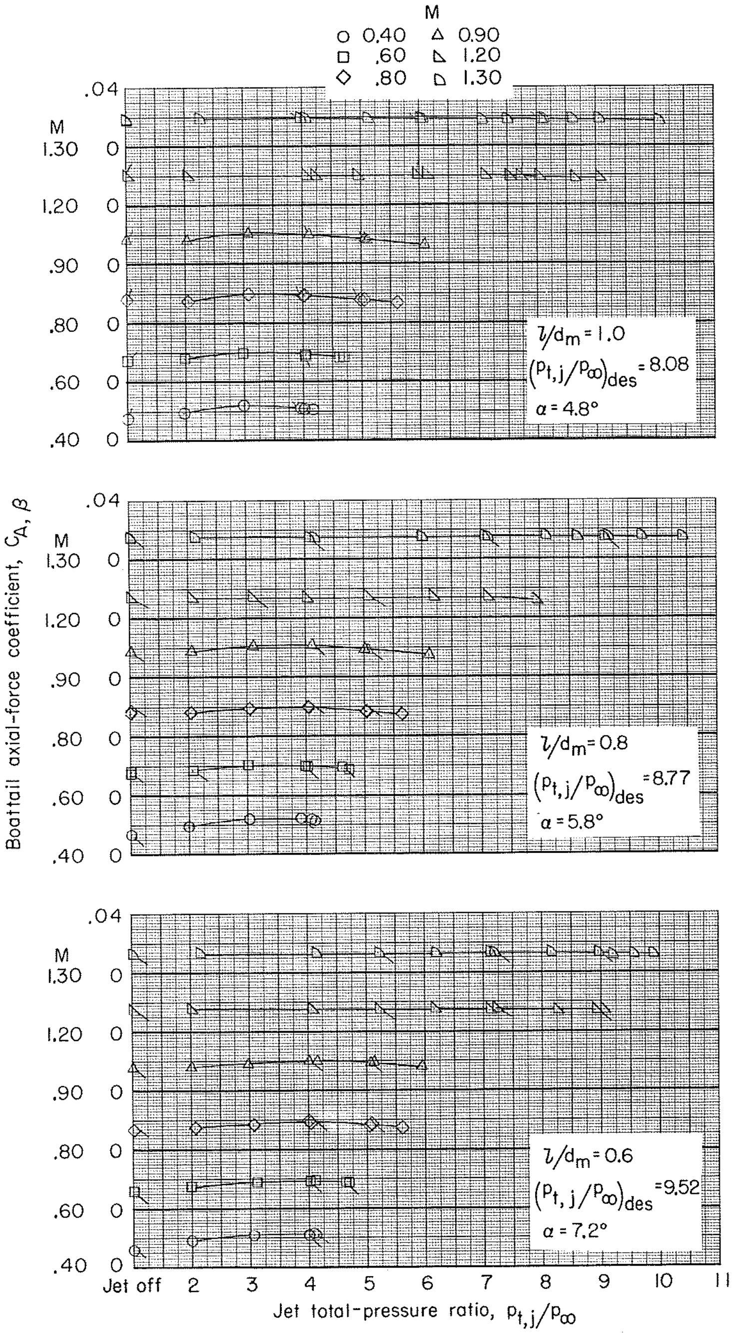

(a) $\beta \approx 3^{0}$.

Figure 14.- Variation of boattail axial-force coefficient with jet total-pressure ratio for various free-stream Mach numbers. (Flagged symbols indicate data taken as pressure ratio was increased.)

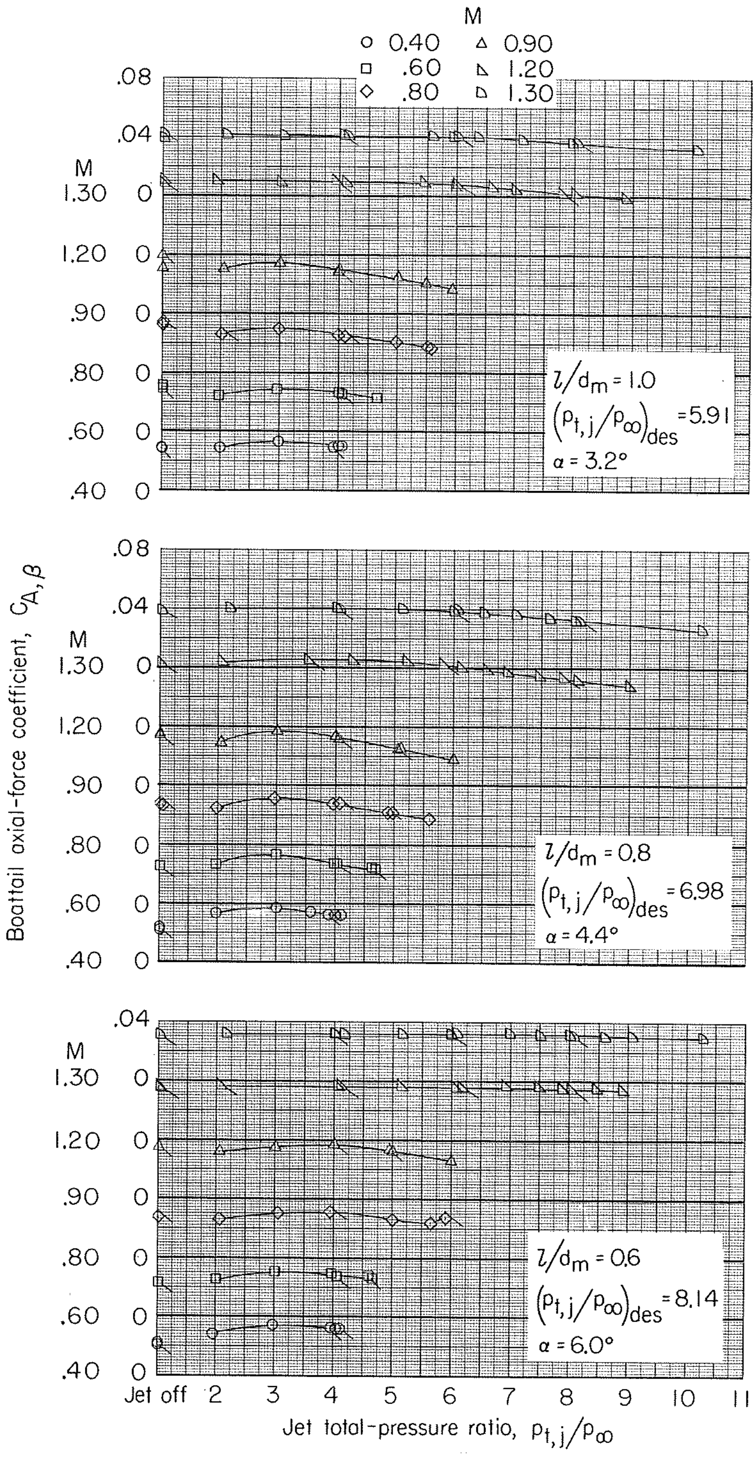

(b) $\beta = 5^0$.

Figure 14.- Continued.

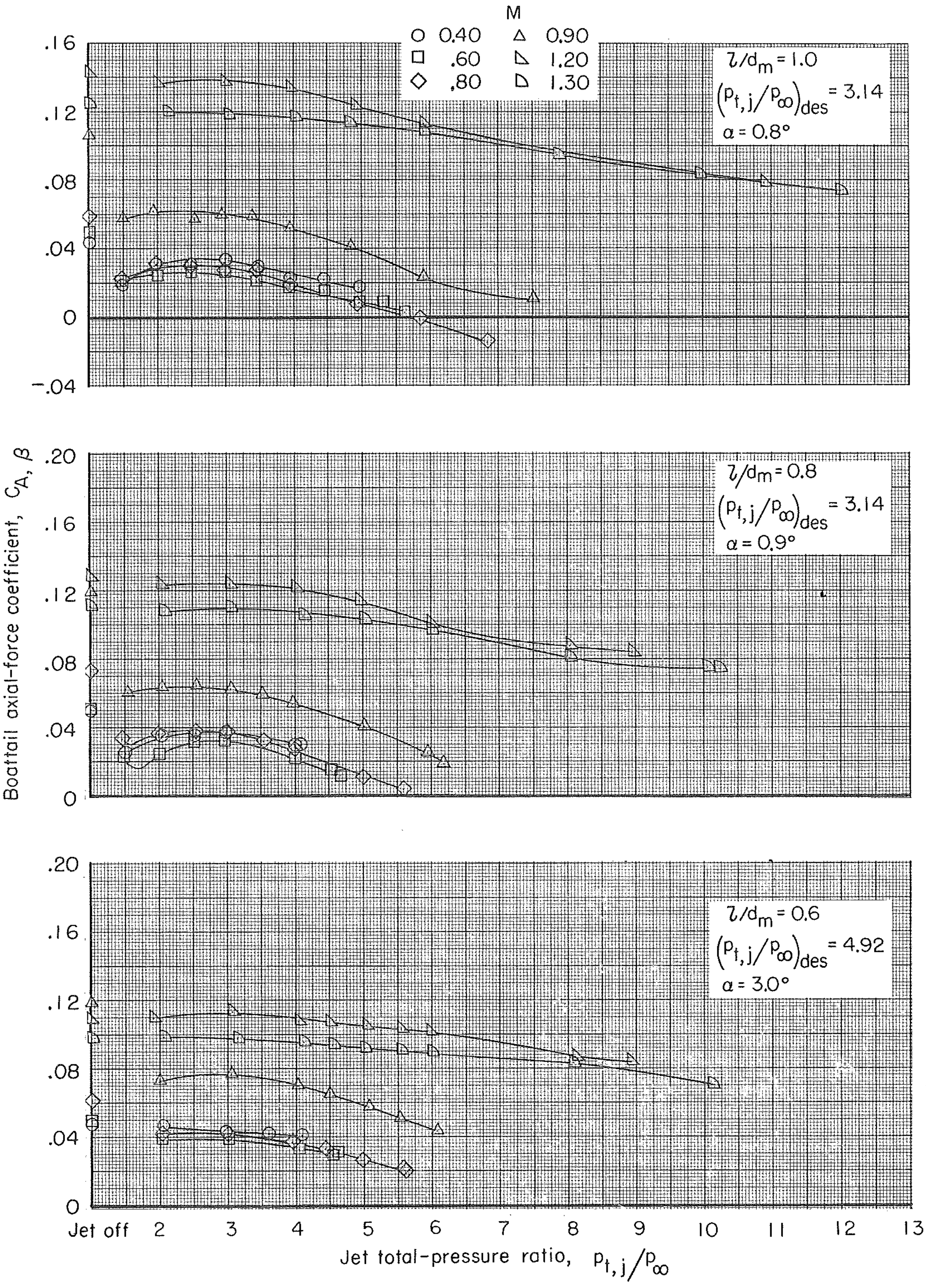

(c) β = 10°.

Figure 14.- Continued.

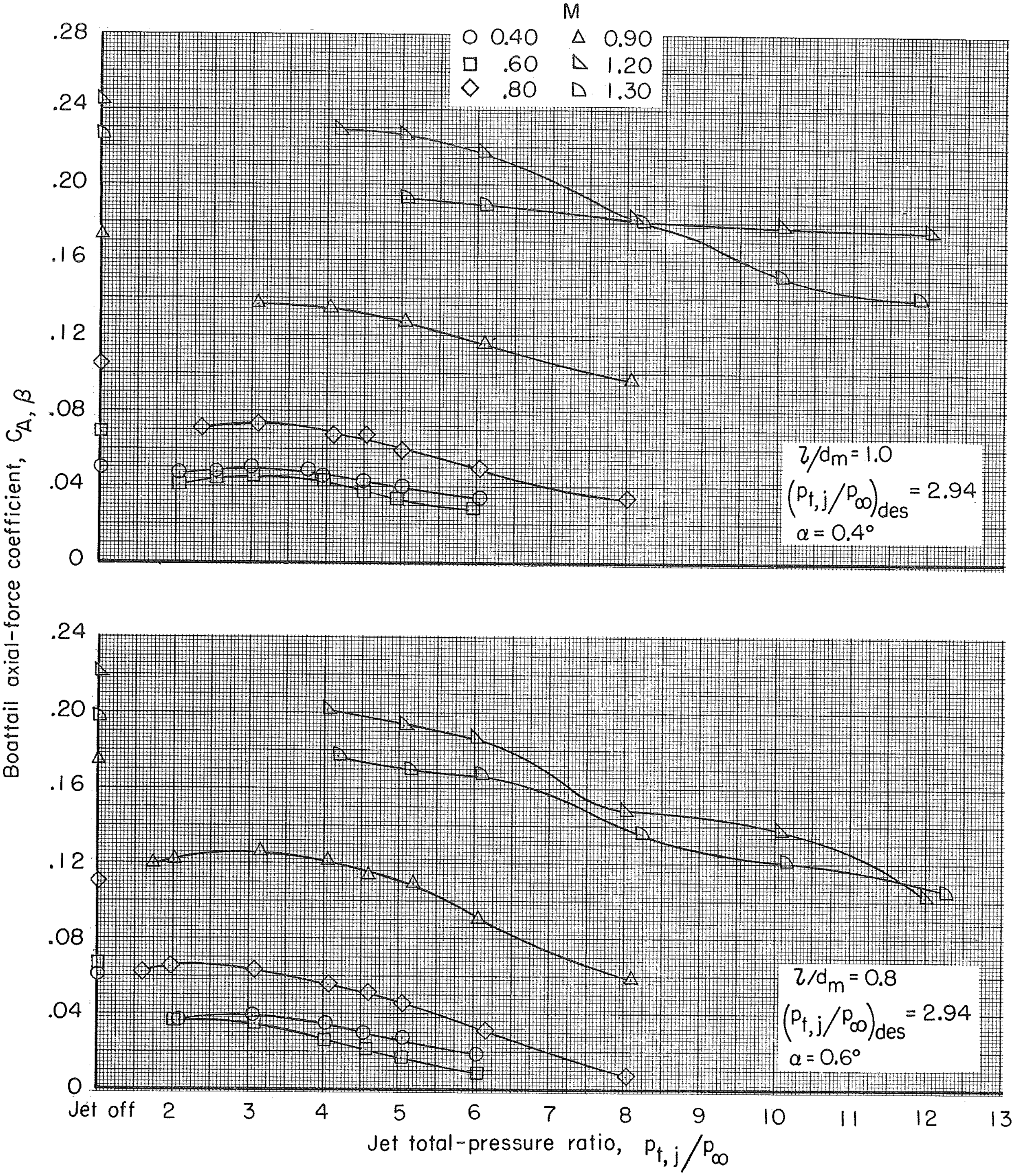

(d) β = 15°.

Figure 14.- Continued.

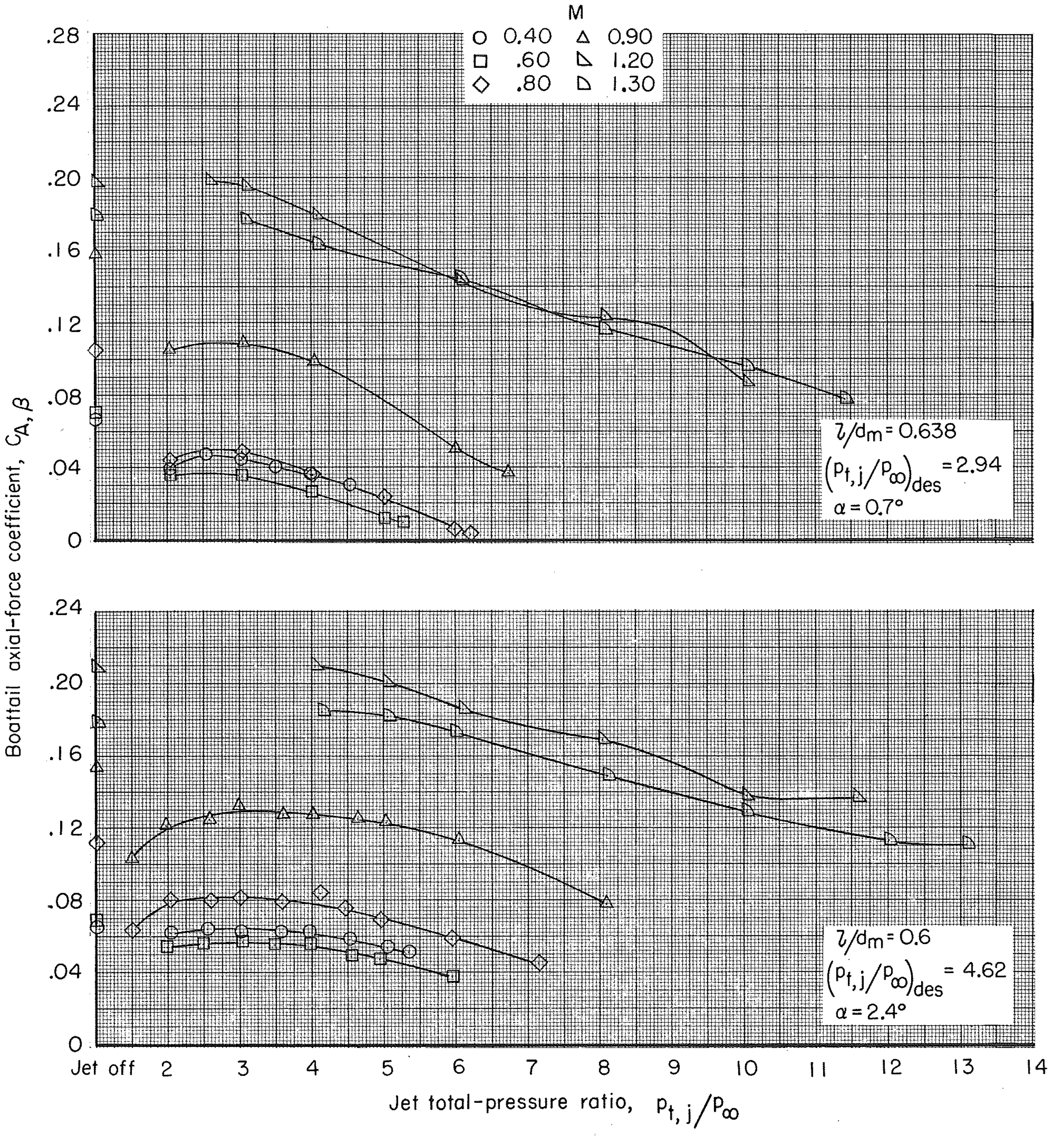

(d) β = 15°. Concluded.

Figure 14.- Continued.

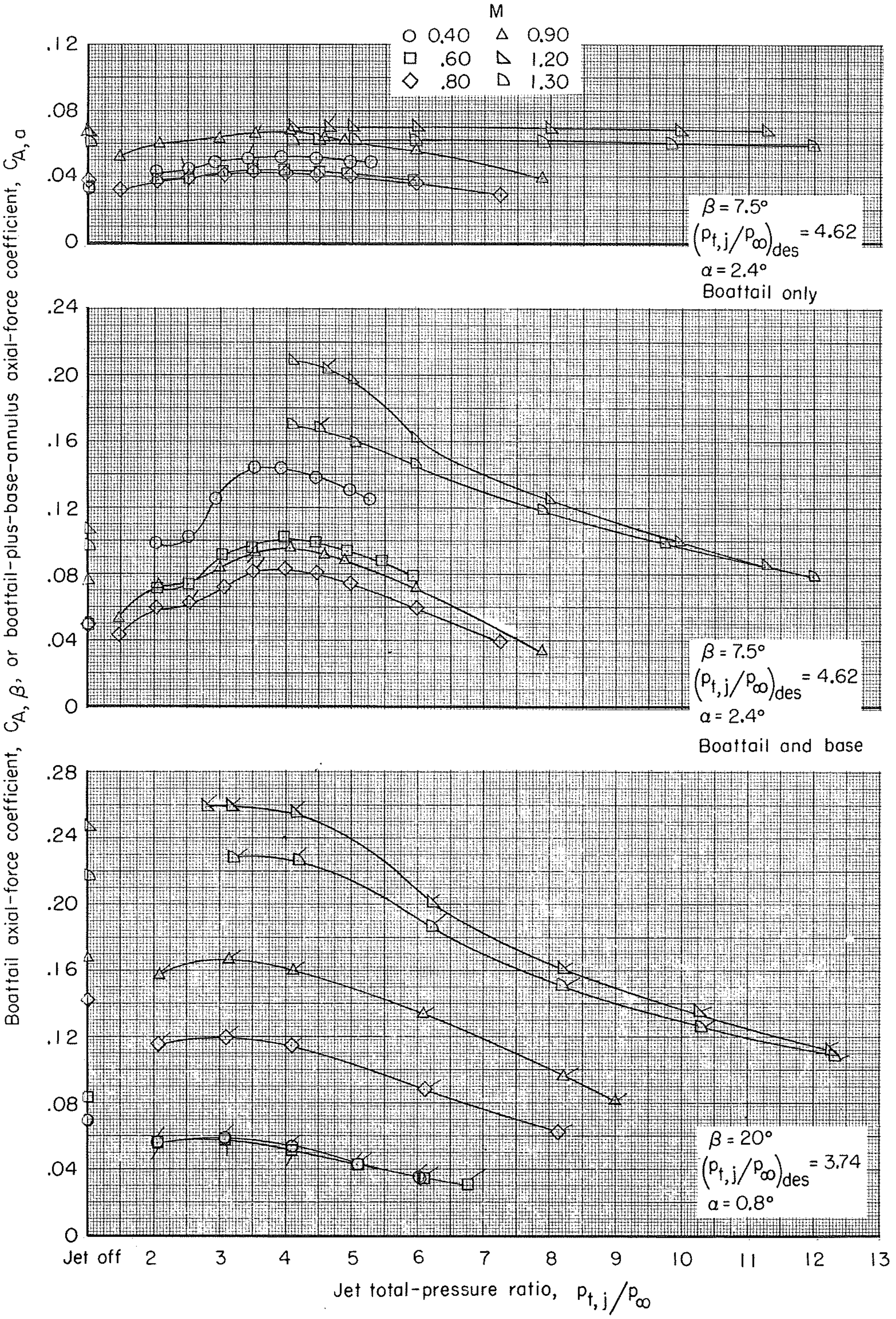

(e) $\beta = 7.5^0$ and 20^0; $l/d_m = 0.6$.

Figure 14.- Concluded.

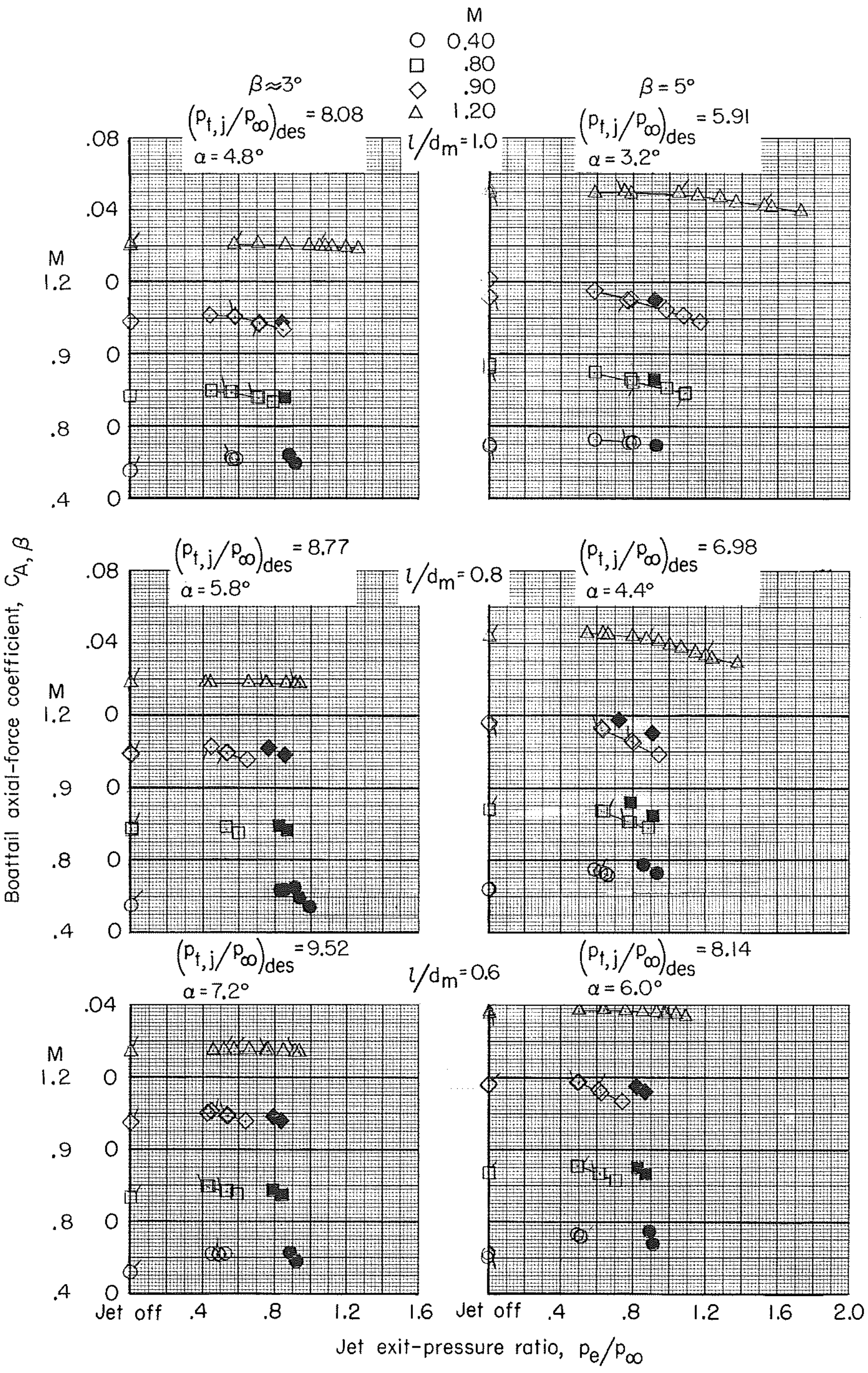

(a) $\beta \approx 3^0$ and 5^0.

Figure 15.- Variation of boattail axial-force coefficient with jet exit-pressure ratio. (Flagged symbols indicate data taken as pressure ratio was increased; solid symbols indicate internally separated flow.)

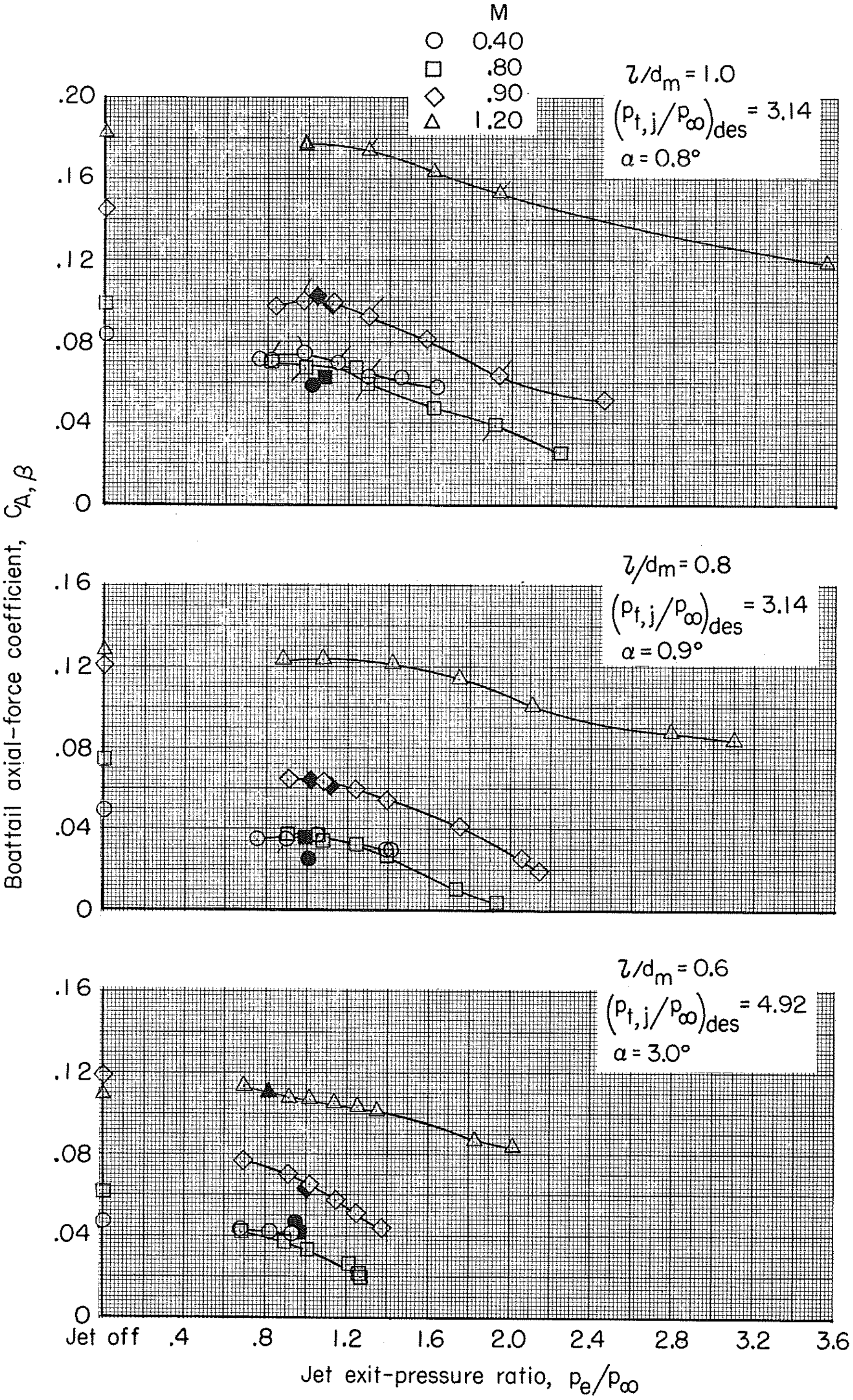

(b) $\beta = 10^0$.

Figure 15.- Continued.

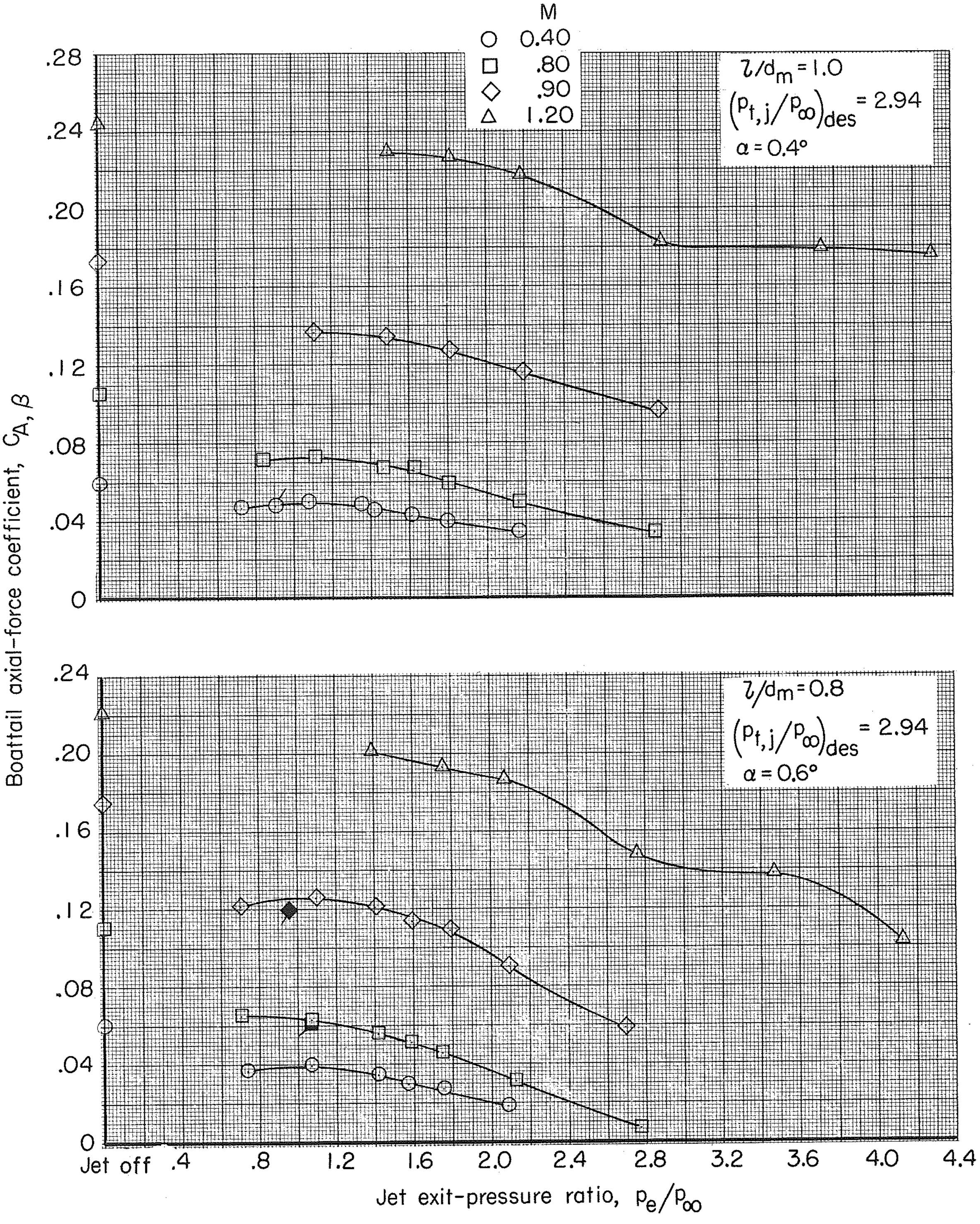

(c) $\beta = 15^0$.

Figure 15.- Continued.

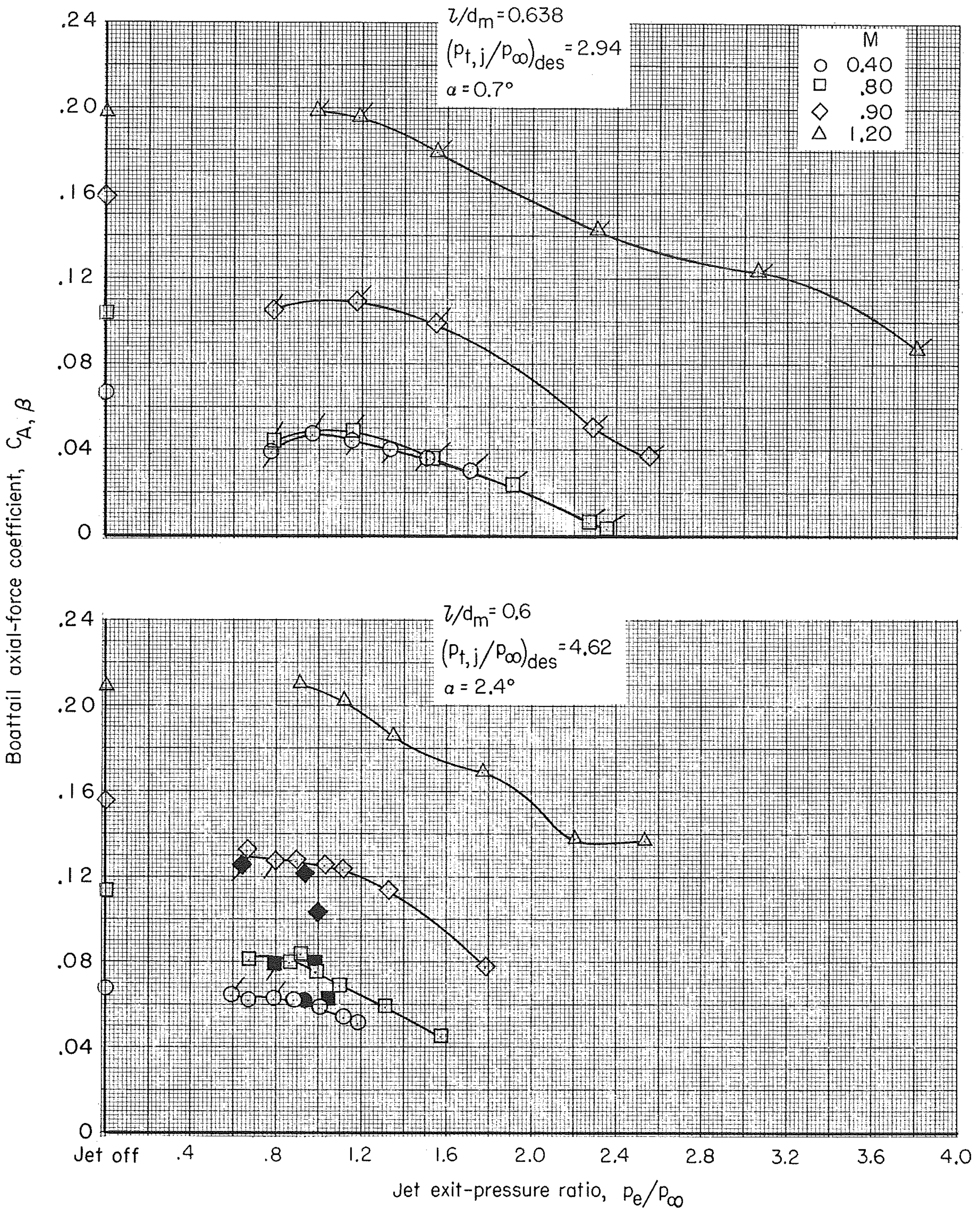

(c) β = 15°. Concluded.

Figure 15.- Continued.

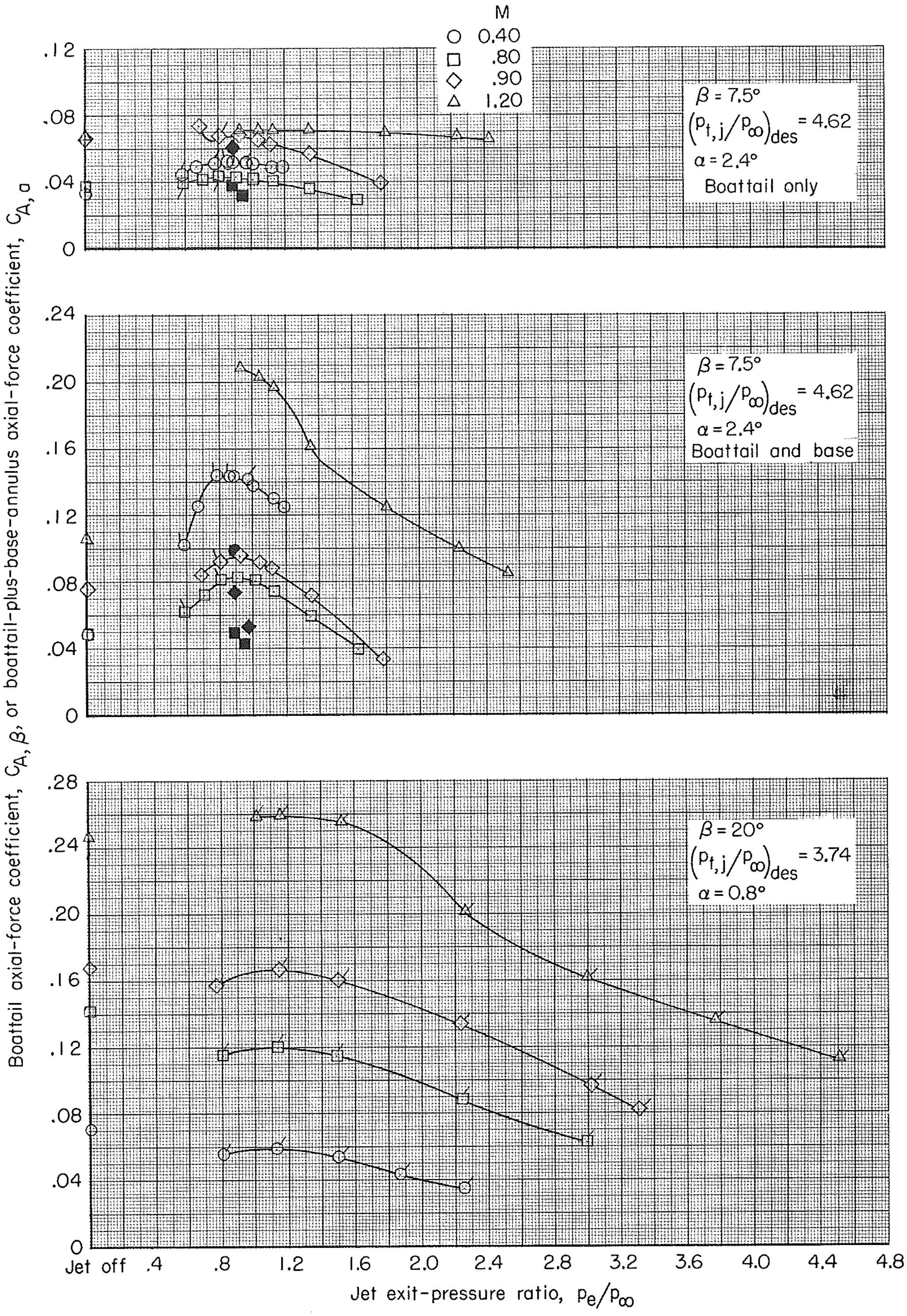

(d) $\beta = 7.5^0$ and 20^0; $l/d_m = 0.6$.

Figure 15.- Concluded.

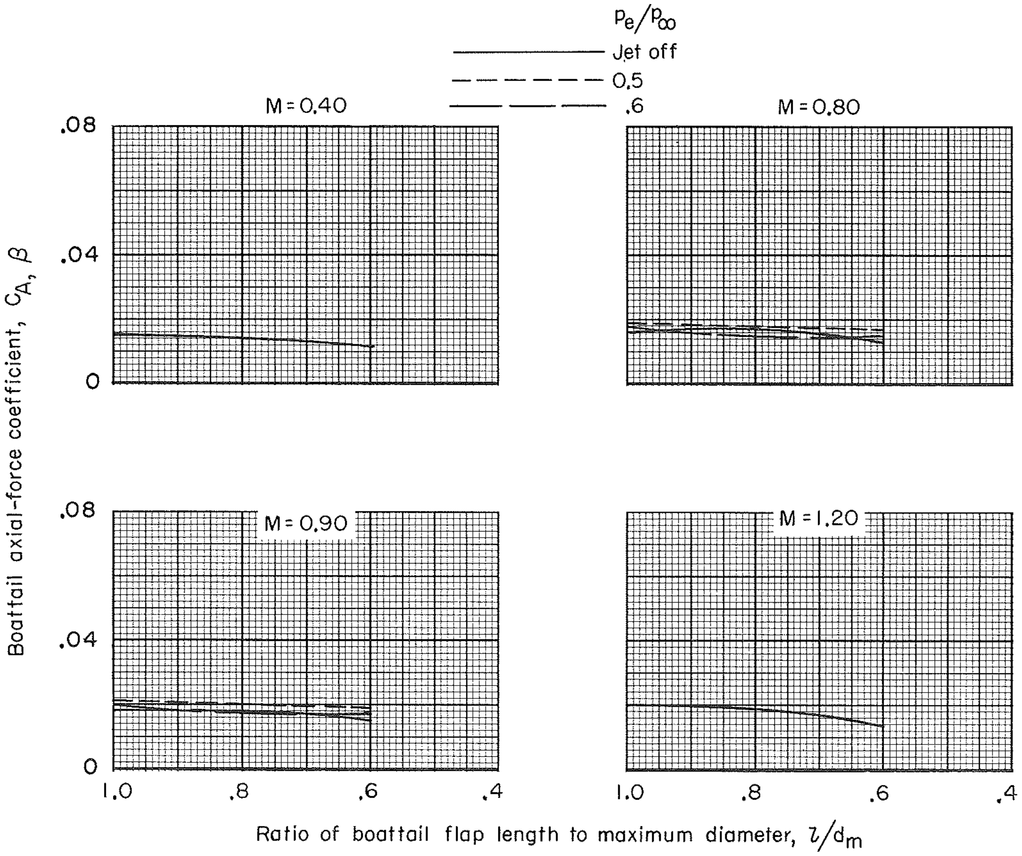

(a) $\beta \approx 3^0$.

Figure 16.- Variation of boattail axial-force coefficient with ratio of boattail flap length to maximum diameter for various jet exit-pressure ratios.

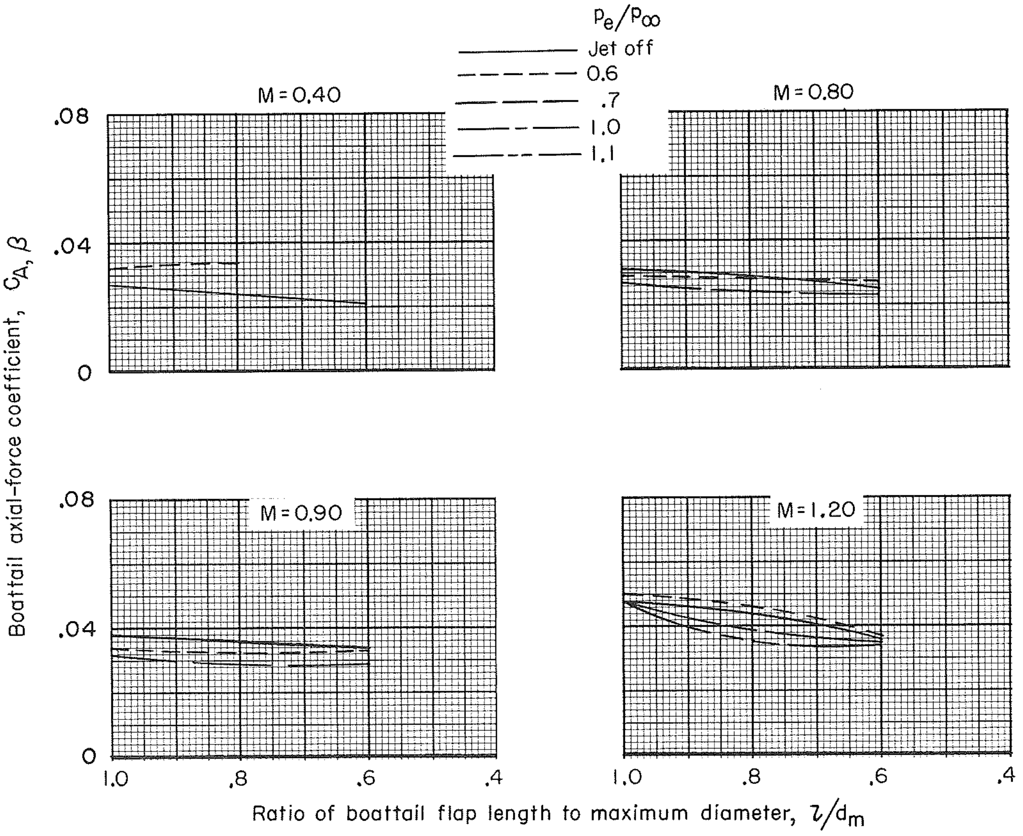

(b) $\beta = 5^0$.

Figure 16.- Continued.

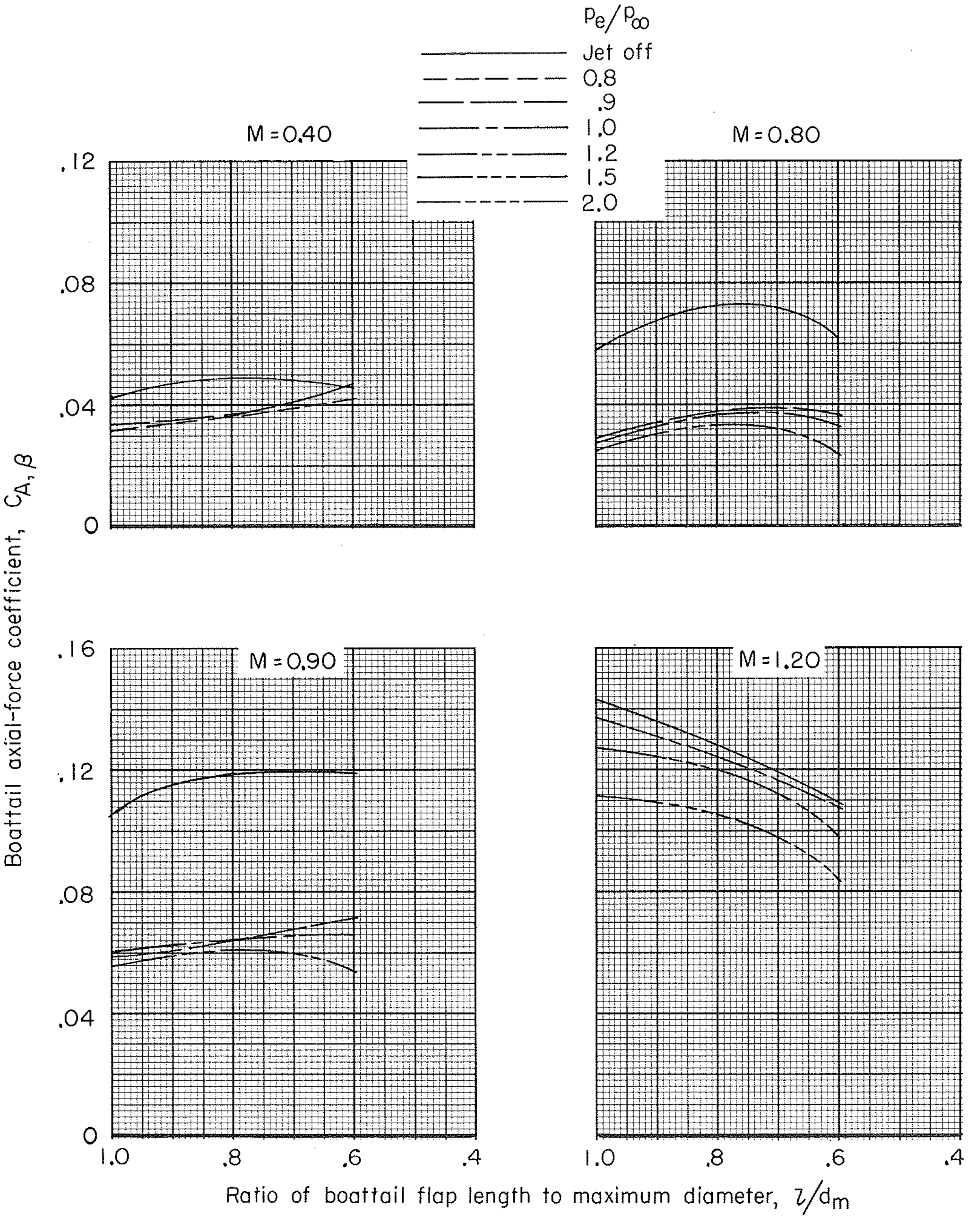

(c) $\beta = 10^0$.

Figure 16.- Continued.

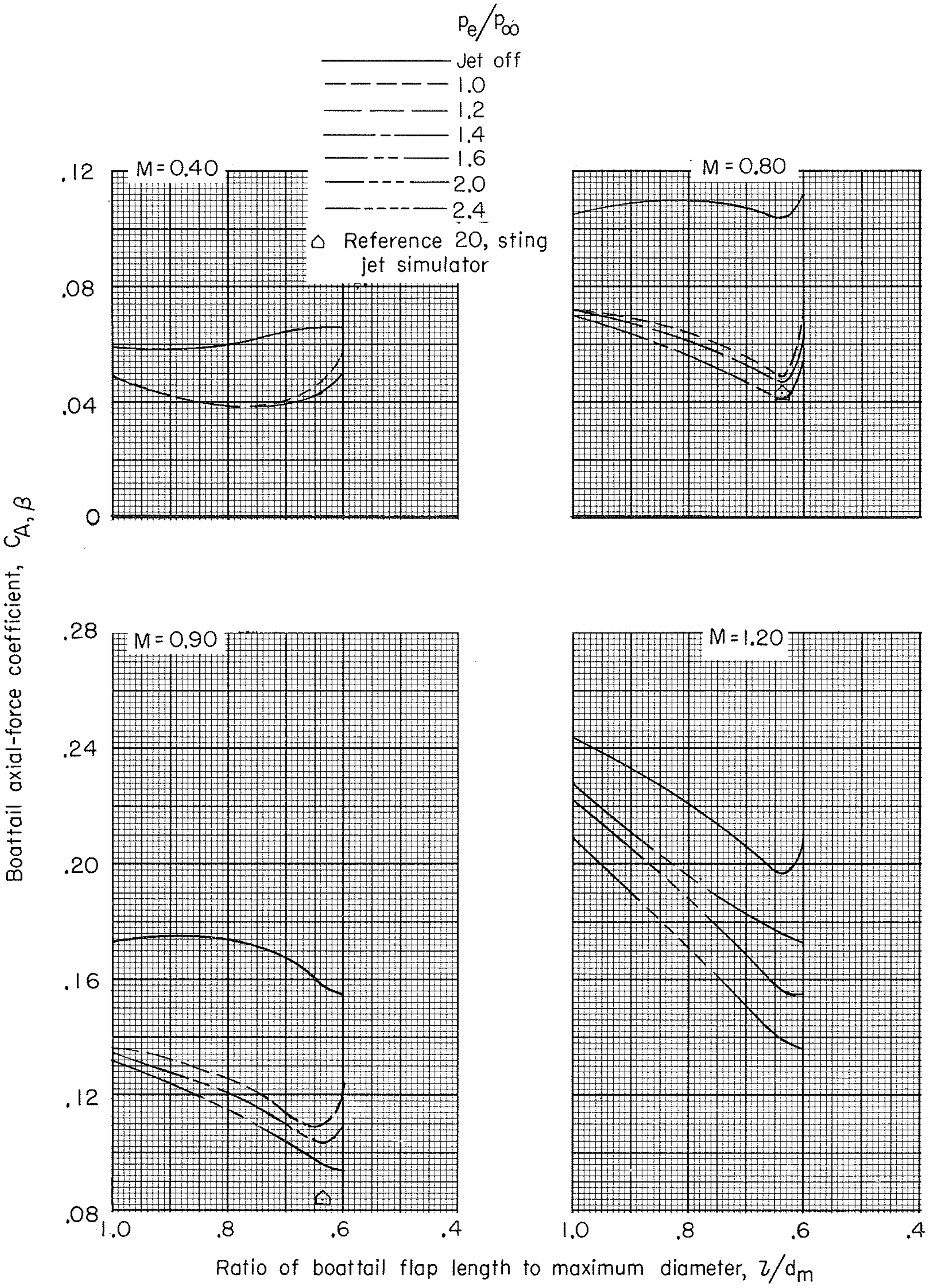

(d) $\beta = 15^0$.

Figure 16.- Concluded.

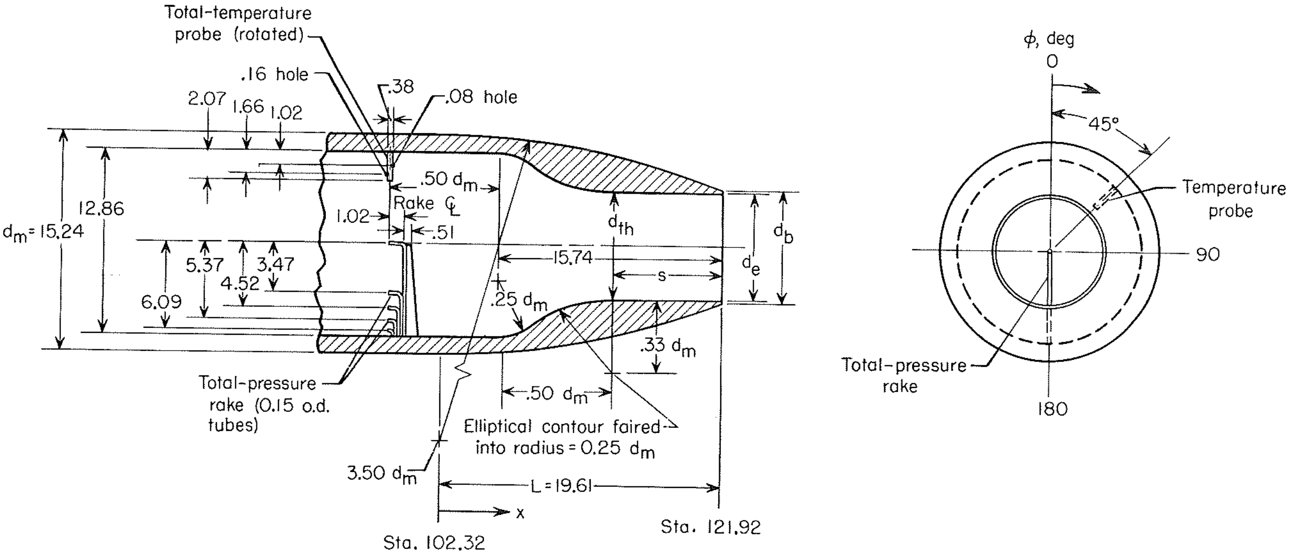

Static orifice locations					
External			Internal		
ϕ, deg	x/d_m	x/L	ϕ, deg	Axial location	x/L
0	-0.17	-0.13	0, 90, and 270	In plane of rake	-0.19
	0	0			
	.19	.15			
	.38	.29			
	.56	.44			
	.75	.58			
	.93	.72			
	1.11	.86			
	1.19	.93	315	3.81 cm from exit	0.81
	1.27	.99			
90 and 180	0	0		0.22 cm from exit (base pressure)	0.99
	.19	.15			
	.38	.29			
	.56	.44			
	.75	.58			
	.93	.72			
	1.11	.86			
	1.19	.93			
	1.27	1.27			

Dimensional and geometric parameters	
d_{th} = 7.62	d_b = 7.77
L/d_m = 1.286	d_b/d_m = 0.510
A_b/A_m = 0.260	A_e/A_b = 0.980
A_{th}/A_m = 0.250	s/d_{th} = 1.000
ϵ_e = 1.000	

Figure 17.- Sketch of reference nozzle showing geometry and orifice locations. (All dimensions are in centimeters unless otherwise noted.)

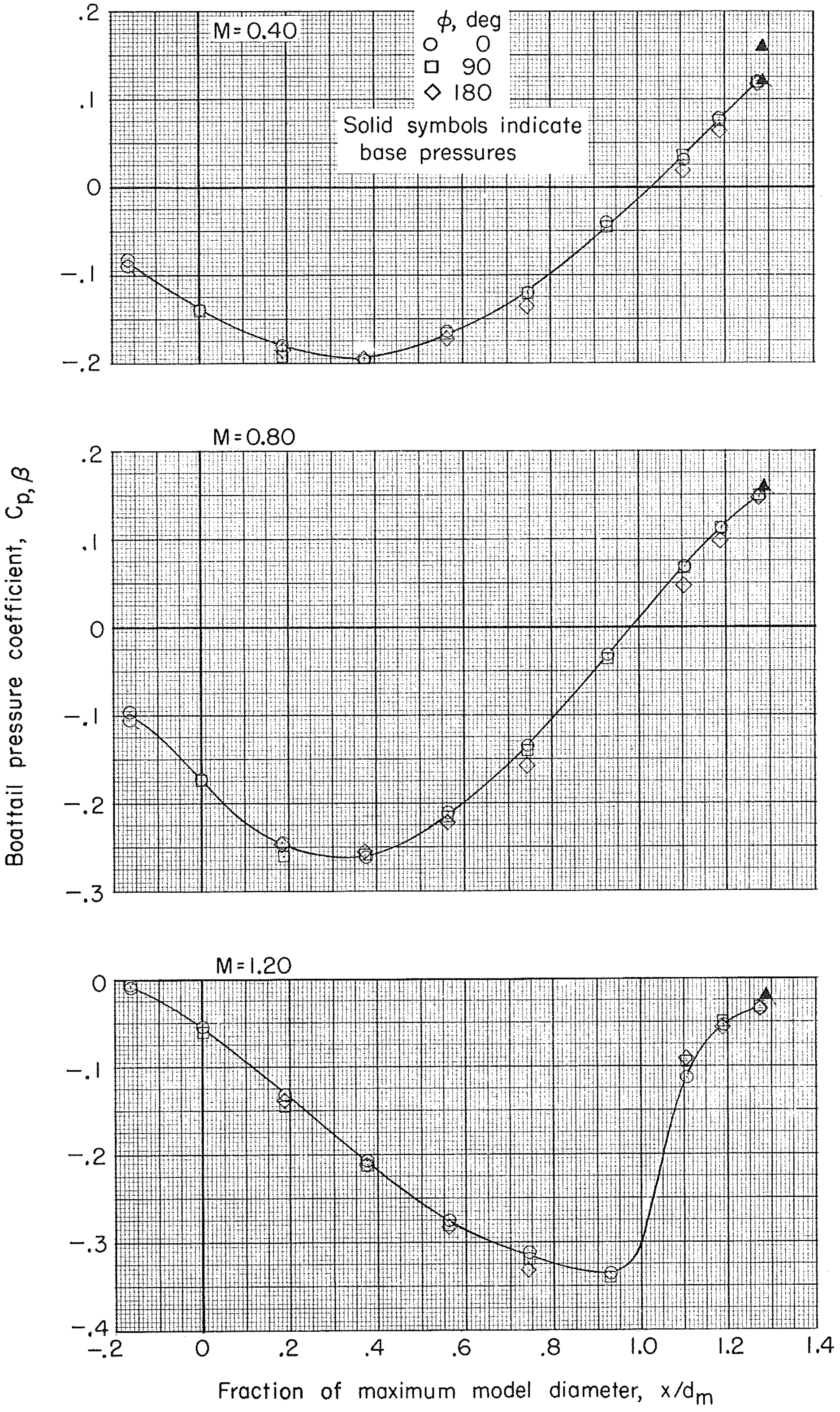

Figure 18.- Boattail pressure-coefficient distributions on reference nozzle for several values of Φ. Jet off.

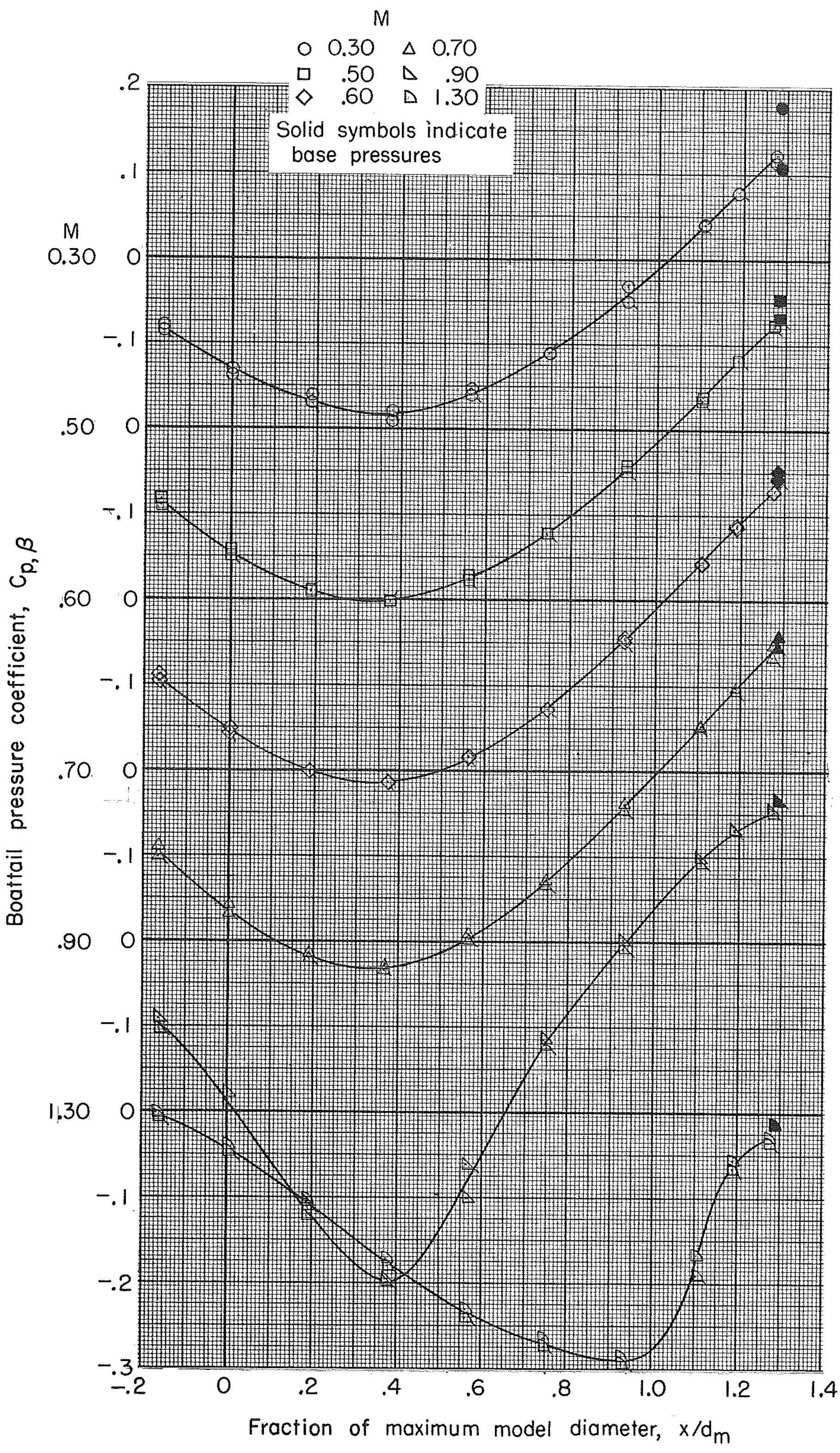

Figure 19.- Boattail pressure-coefficient distributions on reference nozzle at various free-stream Mach numbers. $\phi = 0^0$; jet off. (Flagged symbols indicate data taken as Mach number was decreased.)

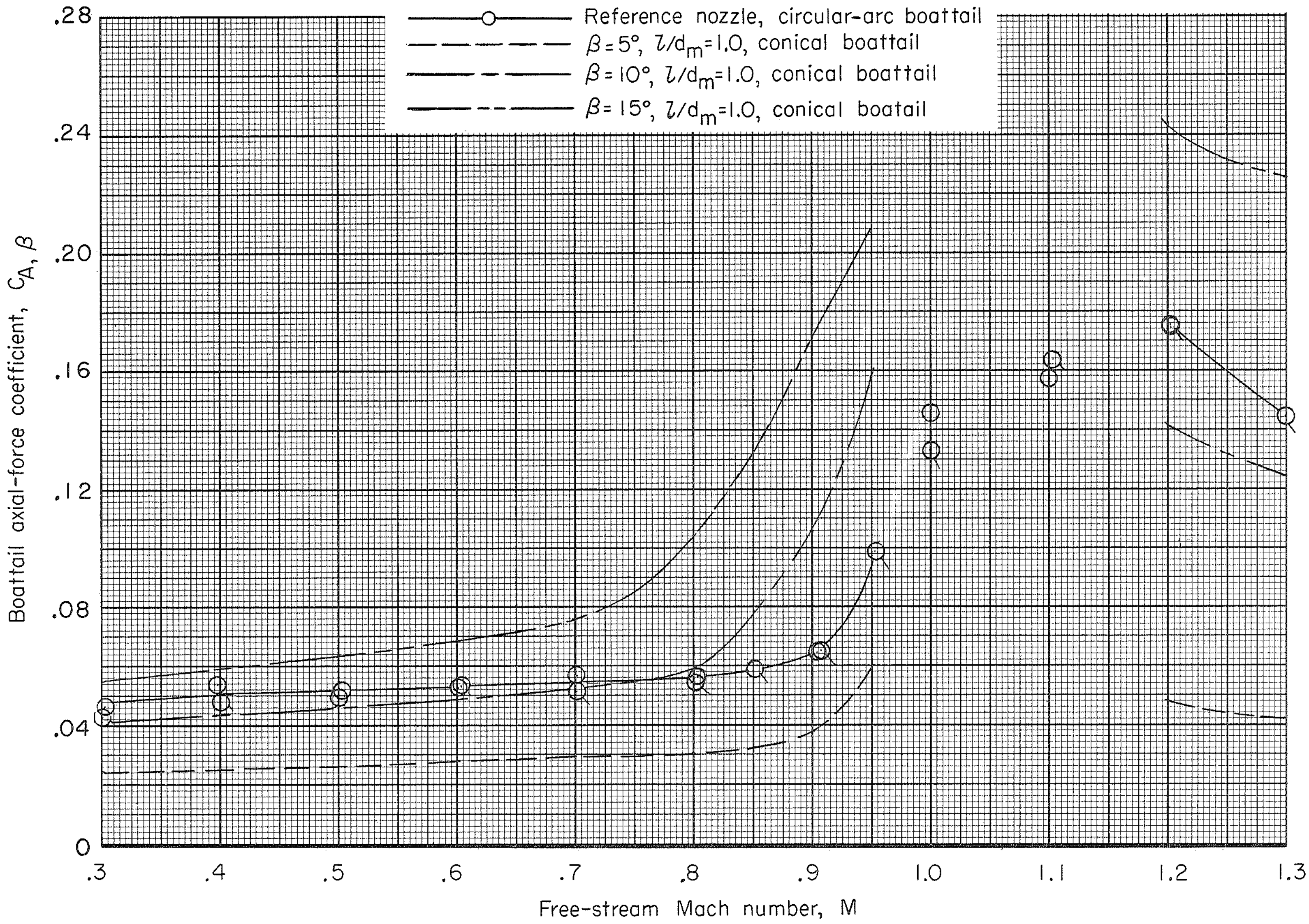

Figure 20.- Variation of boattail axial-force coefficient with free-stream Mach number for reference nozzle and selected conical boattails. Jet off. (Flagged symbols indicate data taken as Mach number was decreased.)

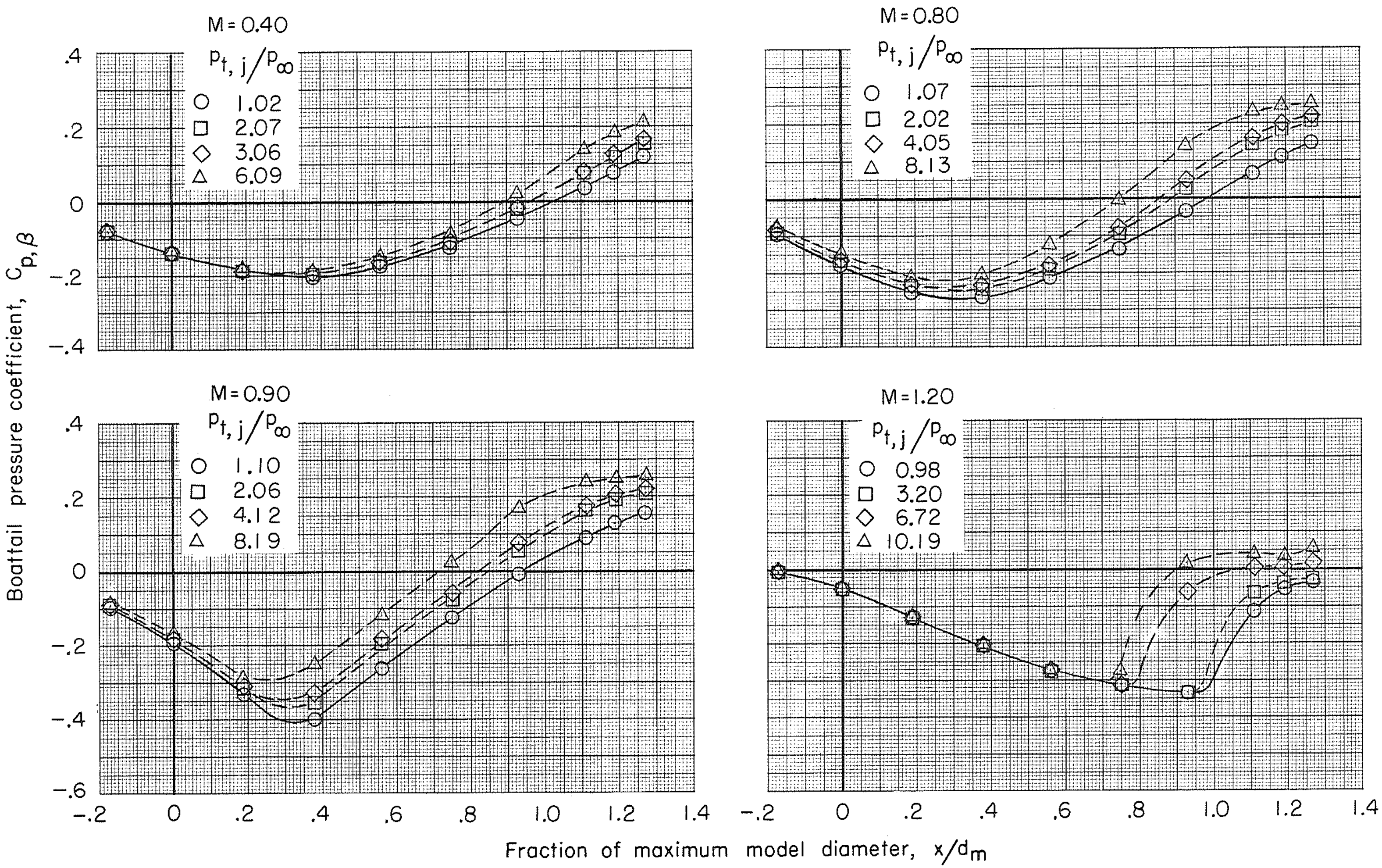

Figure 21.- Boattail pressure-coefficient distributions on reference nozzle at various free-stream Mach numbers and jet total-pressure ratios.

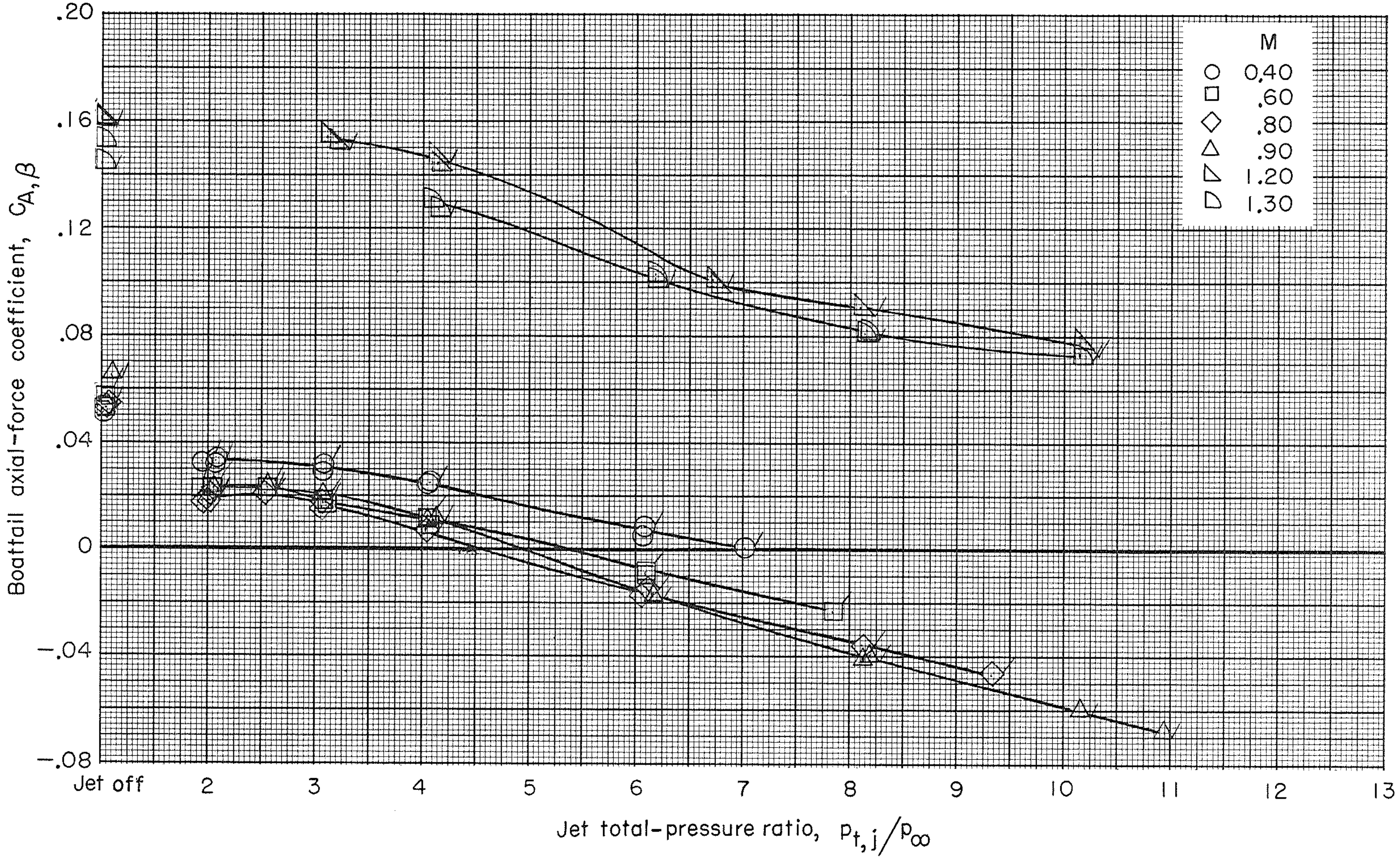

Figure 22.- Variation of boattail axial-force coefficient with jet total-pressure ratio for reference nozzle at various free-stream Mach numbers. (Flagged symbols indicate data taken as pressure ratio was increased.)

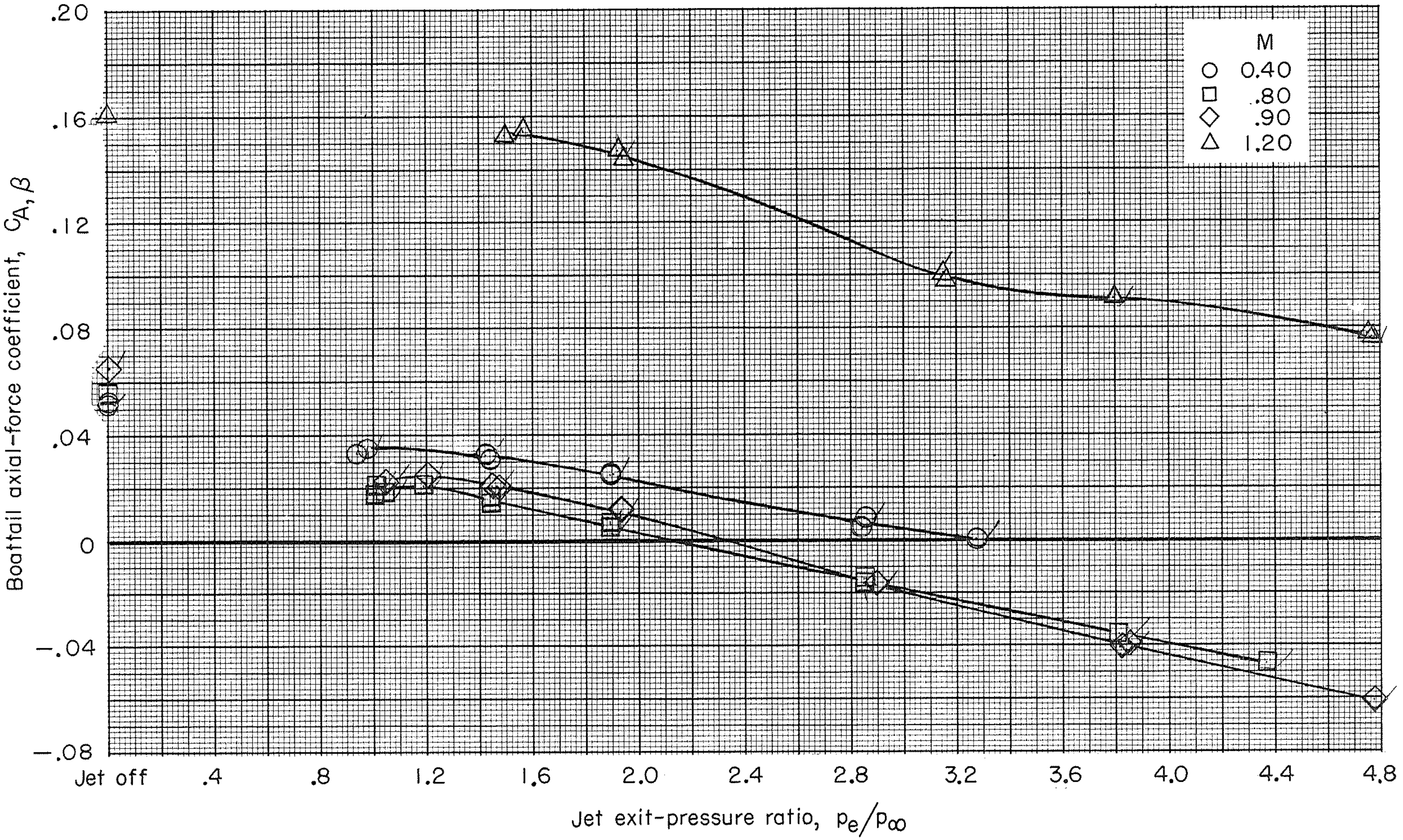

Figure 23.- Variation of boattail axial-force coefficient with jet exit-pressure ratio for reference nozzle at various free-stream Mach numbers. (Flagged symbols indicate data taken as pressure ratio was increased.)

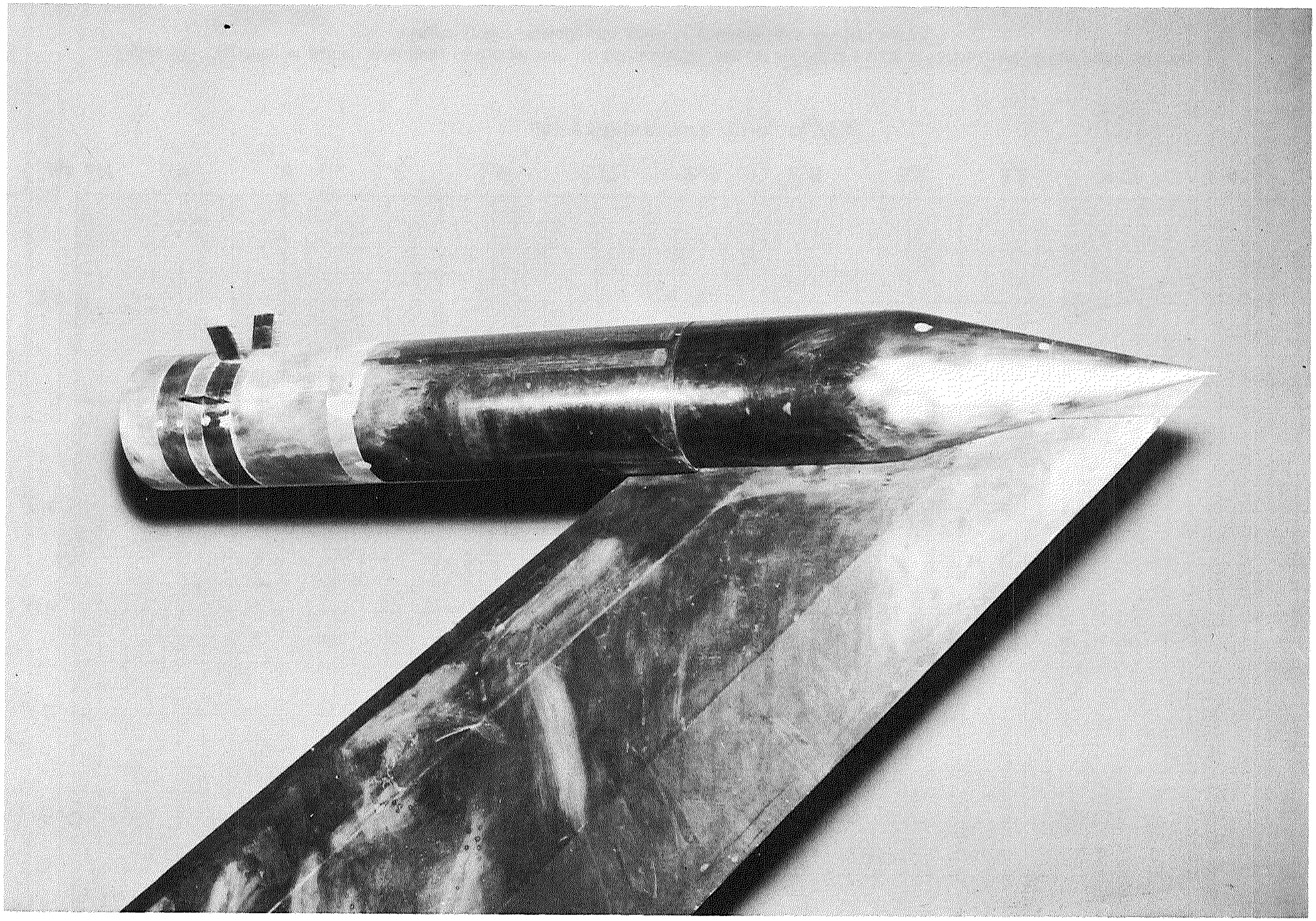

Figure 24.- Photograph of model with cylindrical calibration afterbody having boundary-layer rakes at 0°, 45°, and 90°. L-67-1985

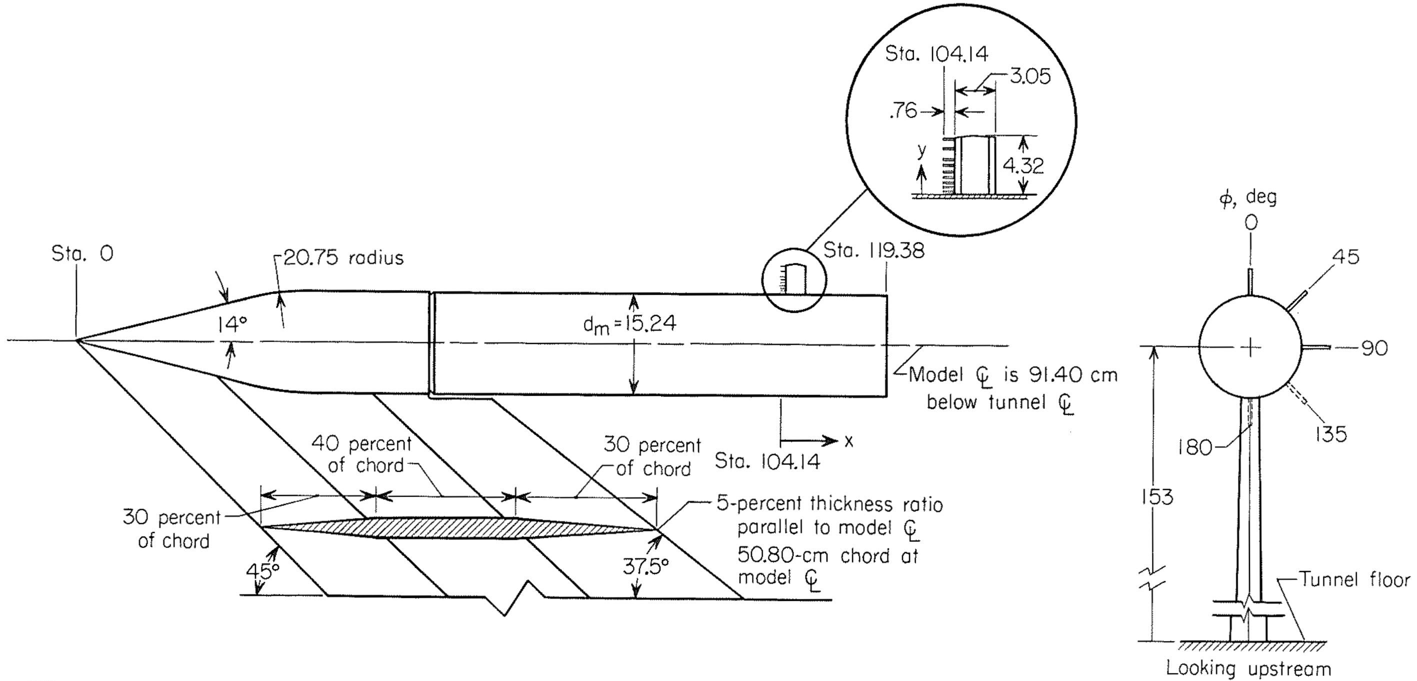

Configuration	Description
A	Cylindrical survey body
B	Cylindrical survey body with boundary-layer rakes at 0°, 45°, and 90°
C	Cylindrical survey body with boundary-layer rakes at 90°, 135°, and 180°

Note: Base pressure orifices located at $\phi = 0°$, 45°, 90°, and 180° at $r/R_m = 0$, 0.50, and 0.92.

Cylinder orifice locations			
Rake off		Rake on	
ϕ, deg	x/d_m	ϕ, deg	x/d_m
0, 90, and 180	−0.37 −0.20 −0.03 .13 .30 .47 .63 .80 .97	0, 90, 135 and 180	−0.75 −0.50 −0.25 0
45 and 135	−0.37 −0.20 −0.03 .13 .30 .47 .63	157.5	−0.75 −0.25

Boundary-layer rake tubes	
y	y/d_m
0.25	0.017
.51	.033
.76	.050
1.14	.075
1.52	.100
2.03	.133
2.54	.167
3.30	.217
4.06	.267

Figure 25.- Sketch of model with cylindrical calibration afterbody showing details of boundary-layer and flow-field survey instrumentation. (All dimensions are in centimeters unless otherwise noted.)

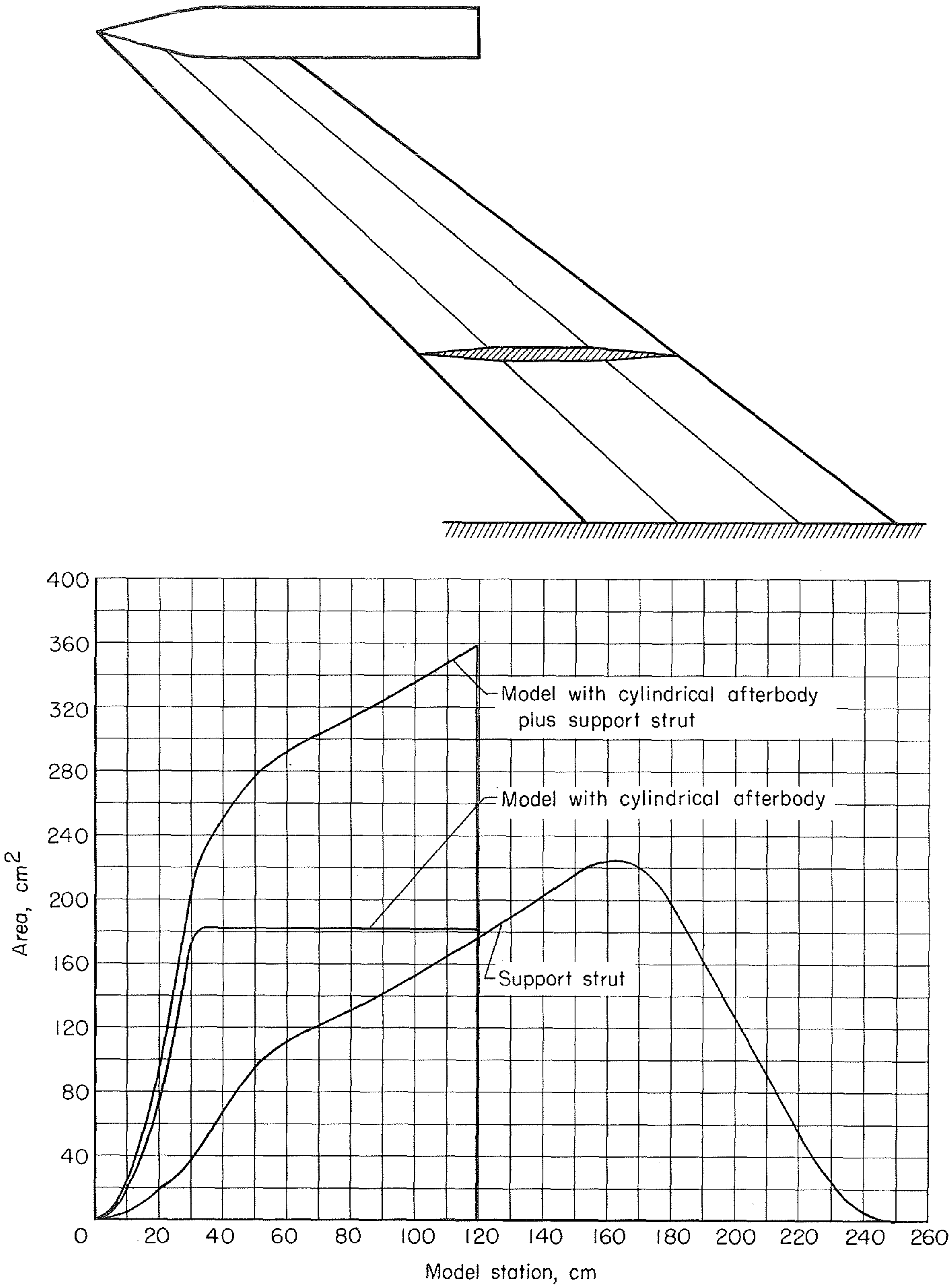

Figure 26.- Area distributions of support strut and model with cylindrical afterbody.

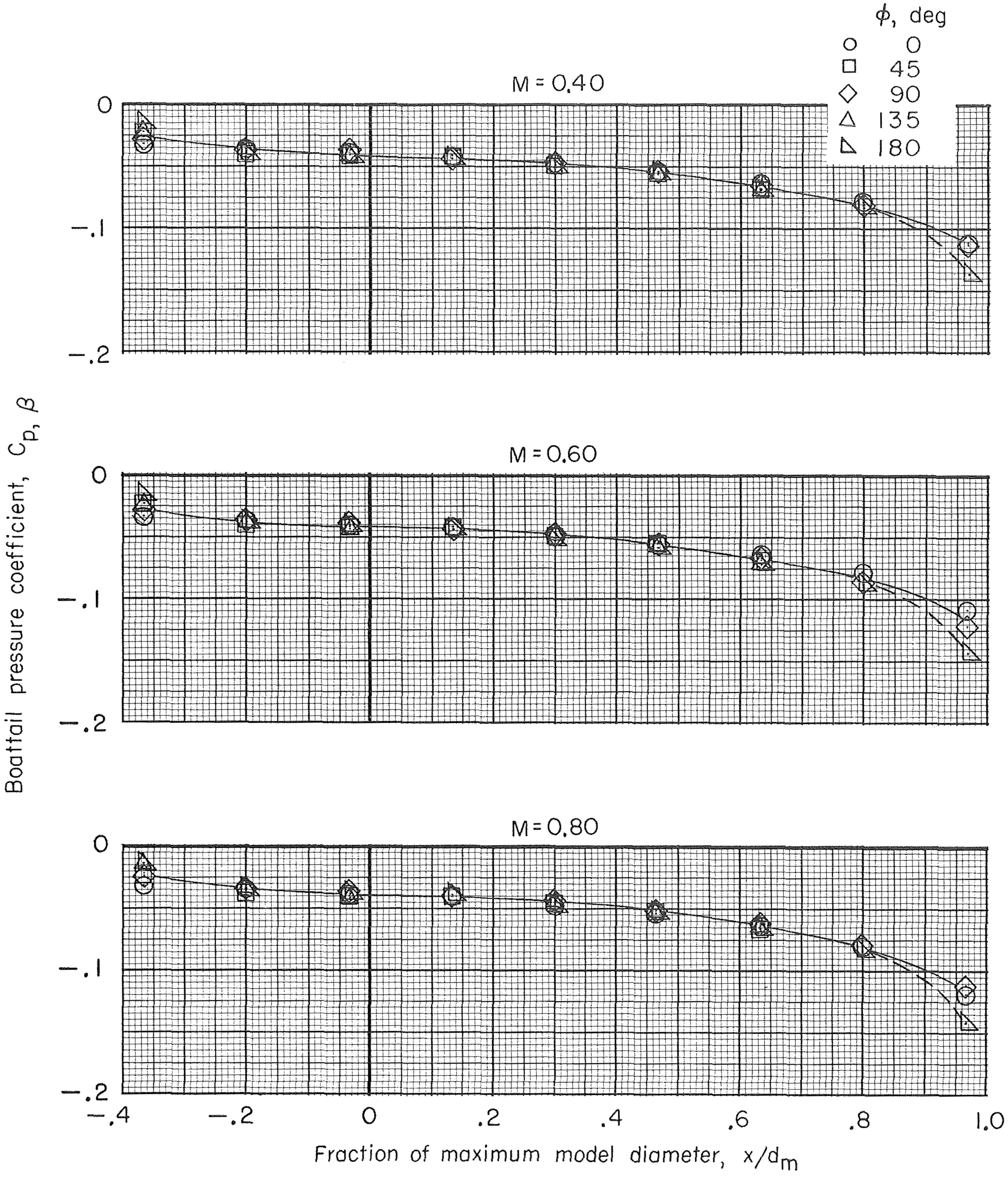

Figure 27.- Typical pressure-coefficient distributions on cylindrical calibration afterbody with a flat base for various free-stream Mach numbers and values of Φ. $\beta = 0^0$.

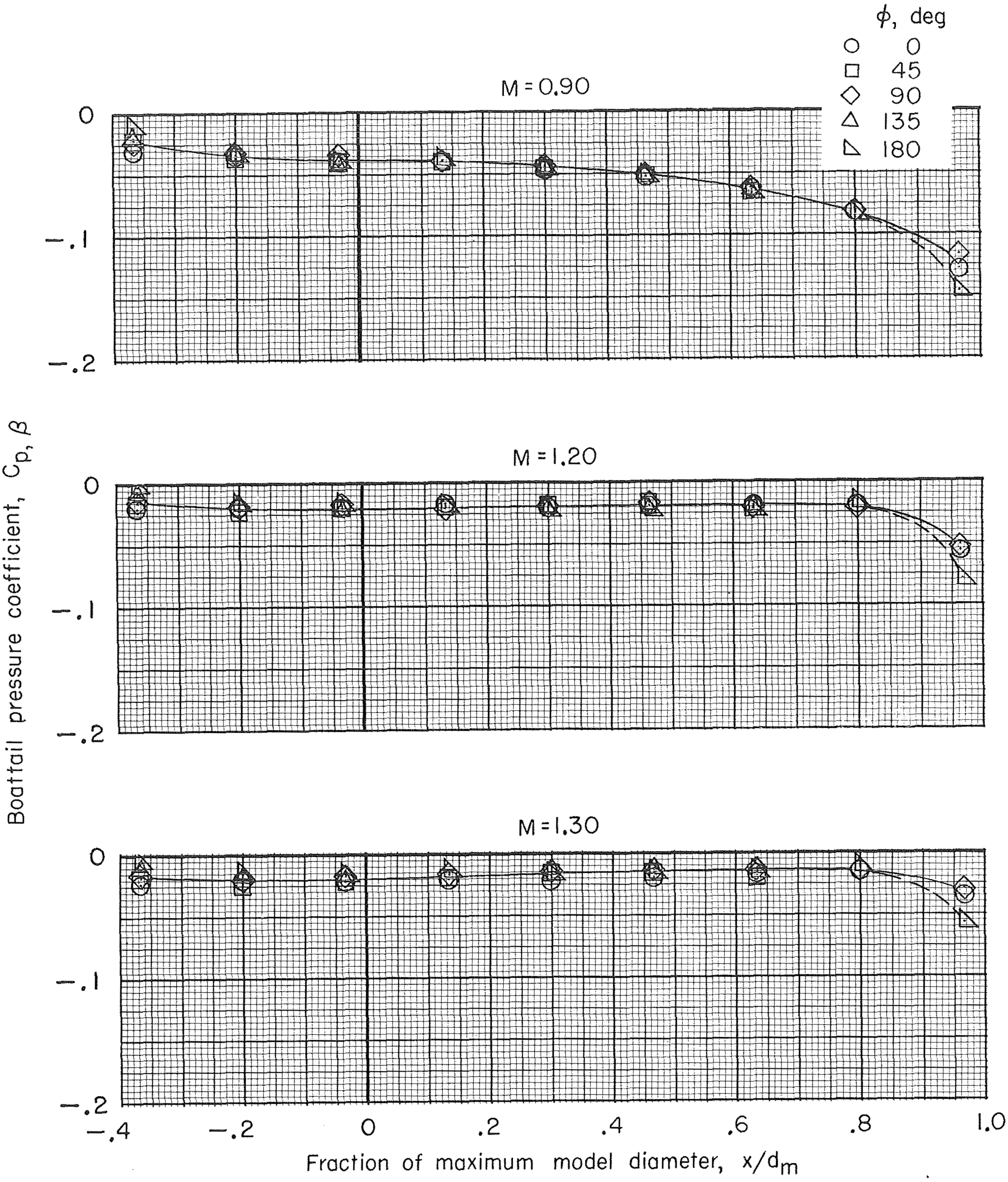

Figure 27.- Concluded.

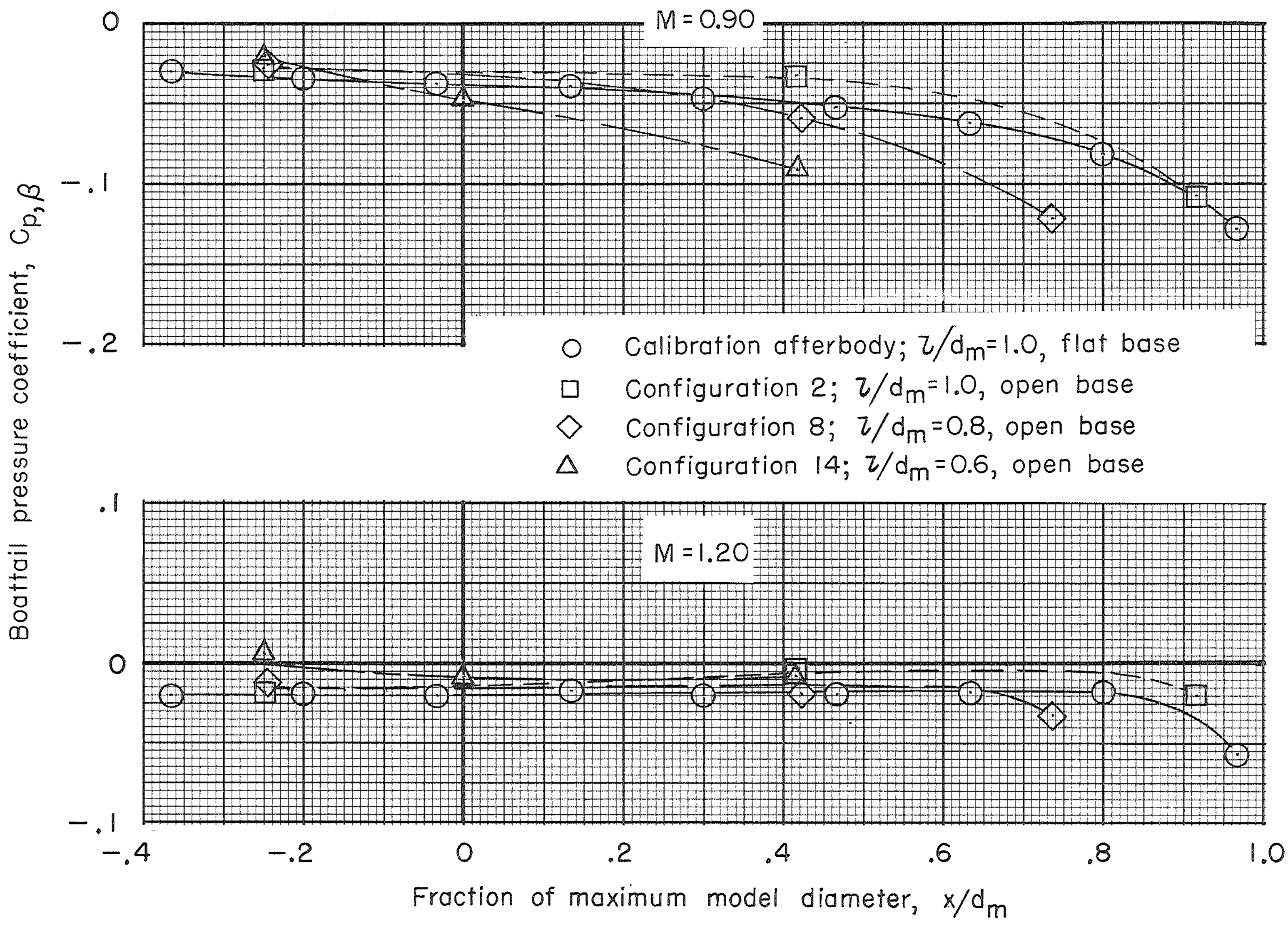

Figure 28.- Comparison of pressure-coefficient distributions on cylindrical afterbodies of several lengths with open and flat bases. $\Phi = 0^0$; $\beta = 0^0$.

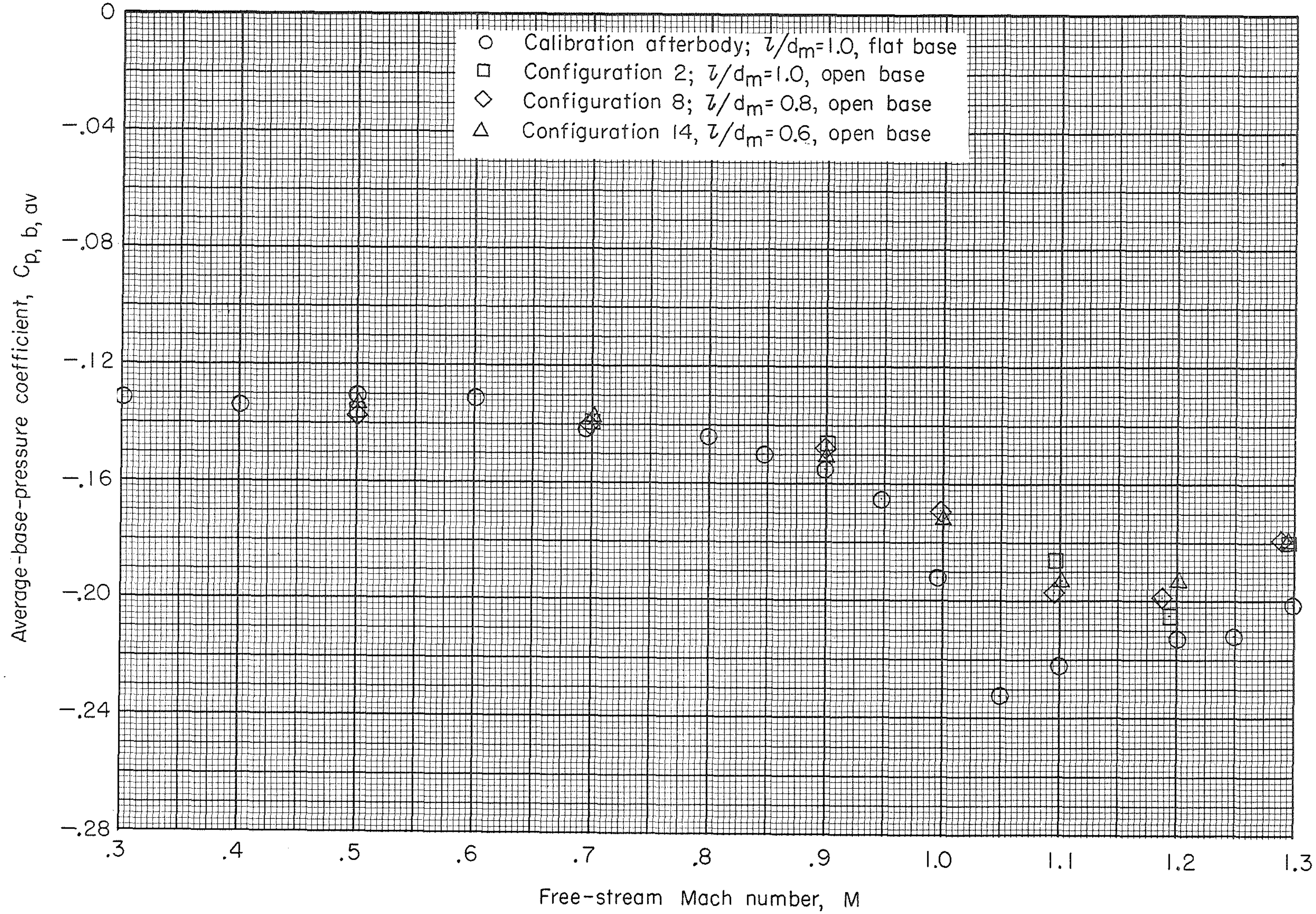

Figure 29.- Variation of average-base-pressure coefficient with free-stream Mach number for cylindrical afterbodies of several lengths with flat and open bases. $\beta = 0^0$.

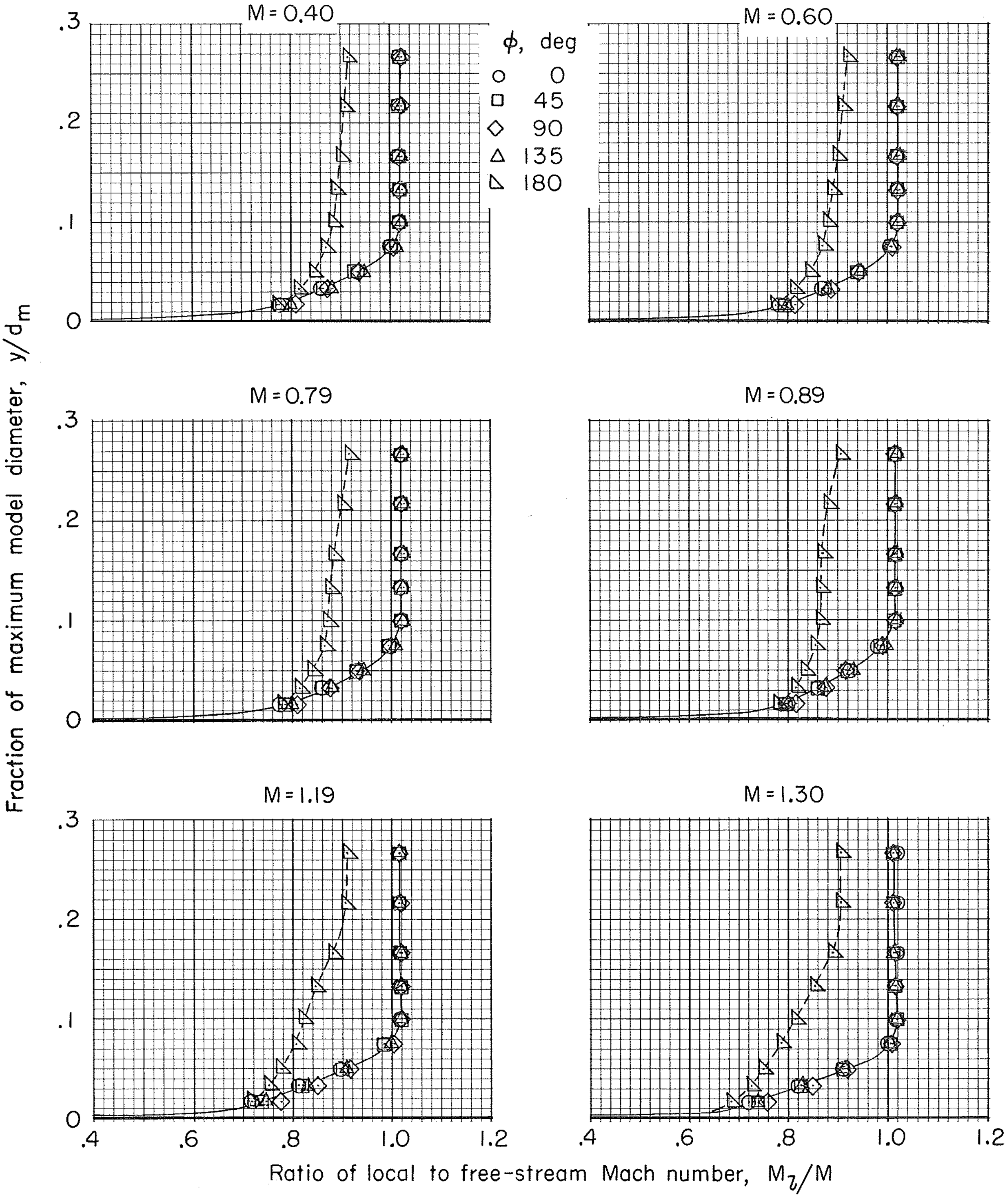

Figure 30.- Typical boundary-layer Mach number profiles for cylindrical calibration afterbody at various free-stream Mach numbers.

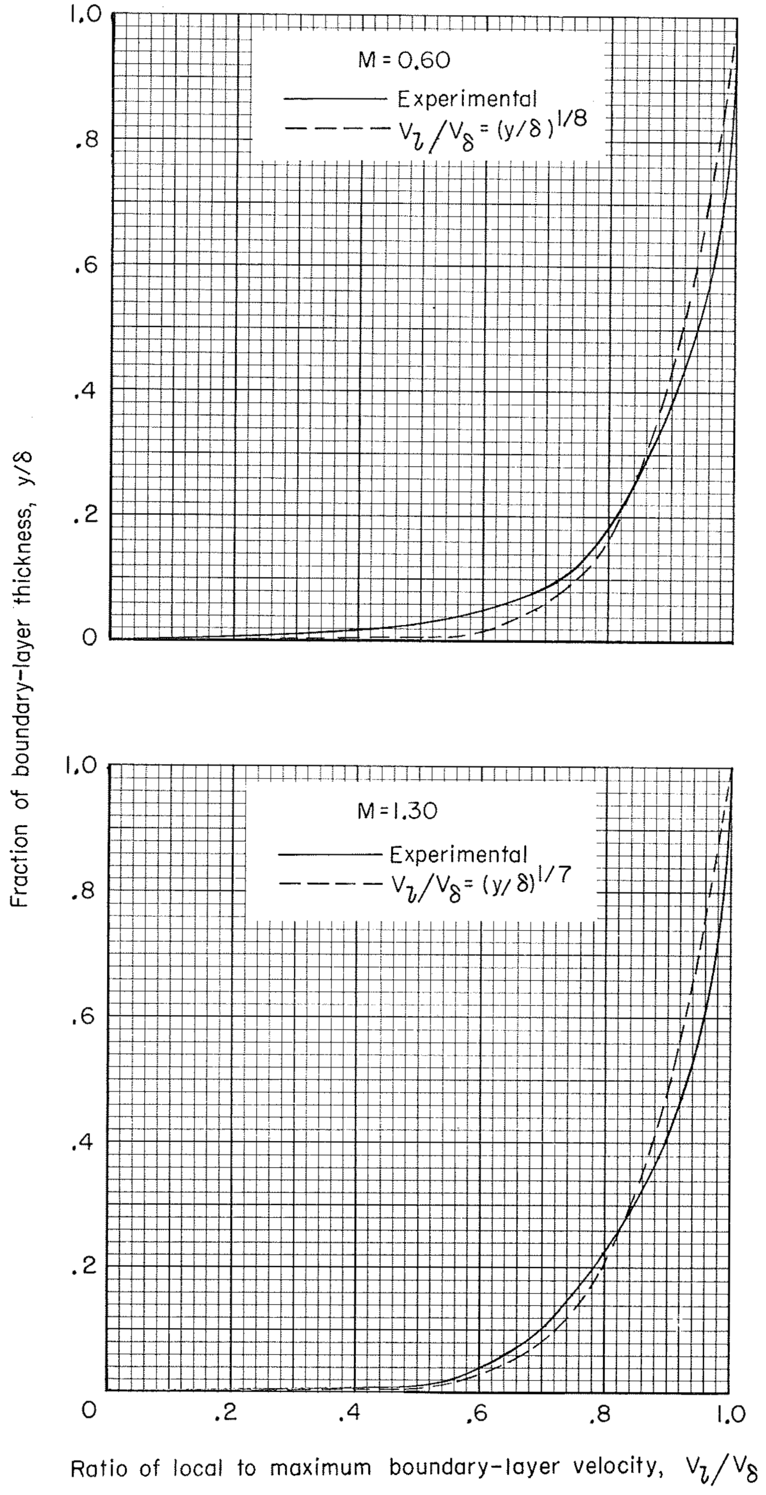

Figure 31.- Comparison of experimental and power-law-calculated boundary-layer profiles.

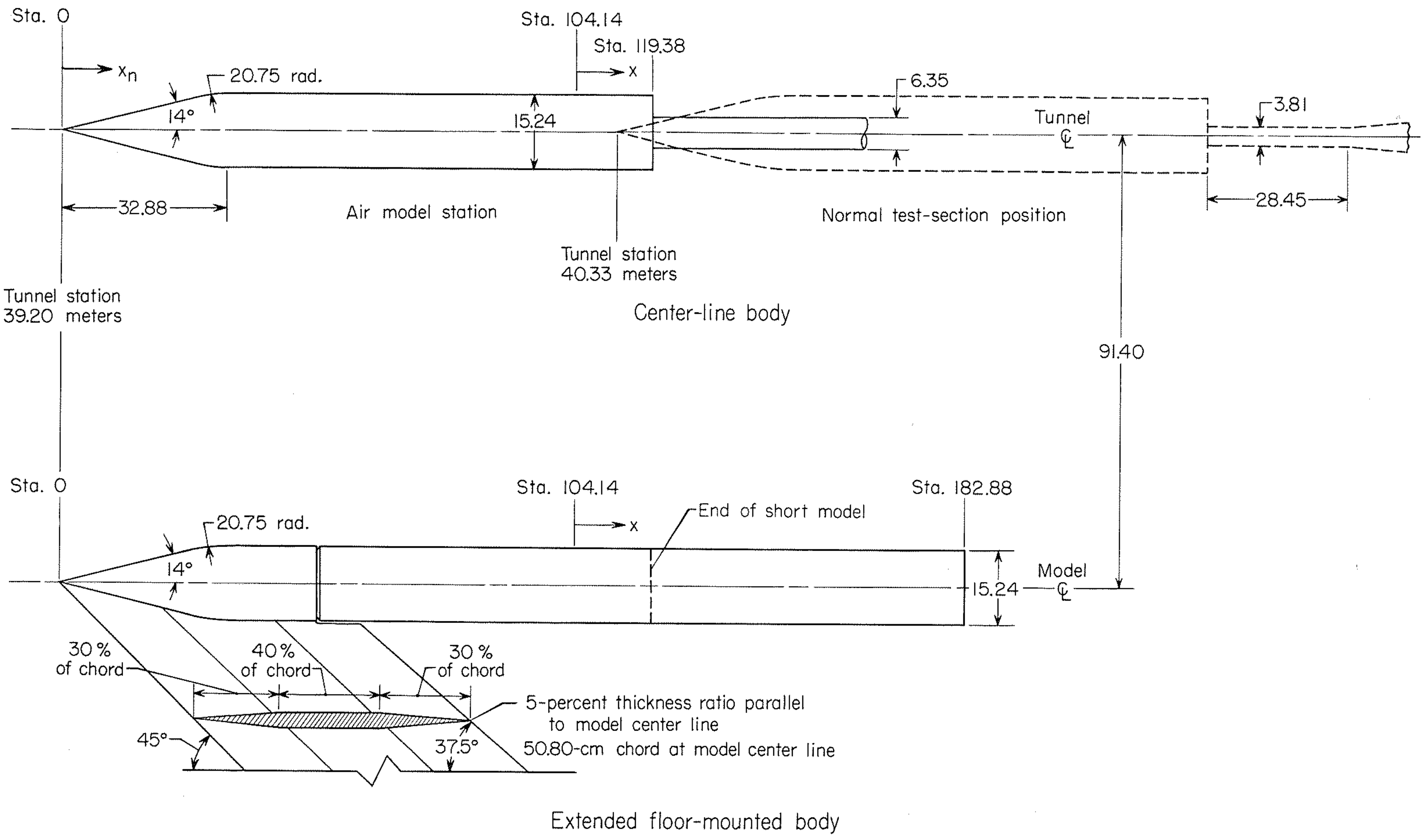

Figure 32.- Sketch of flow-field survey bodies. (All dimensions are in centimeters unless otherwise noted.)

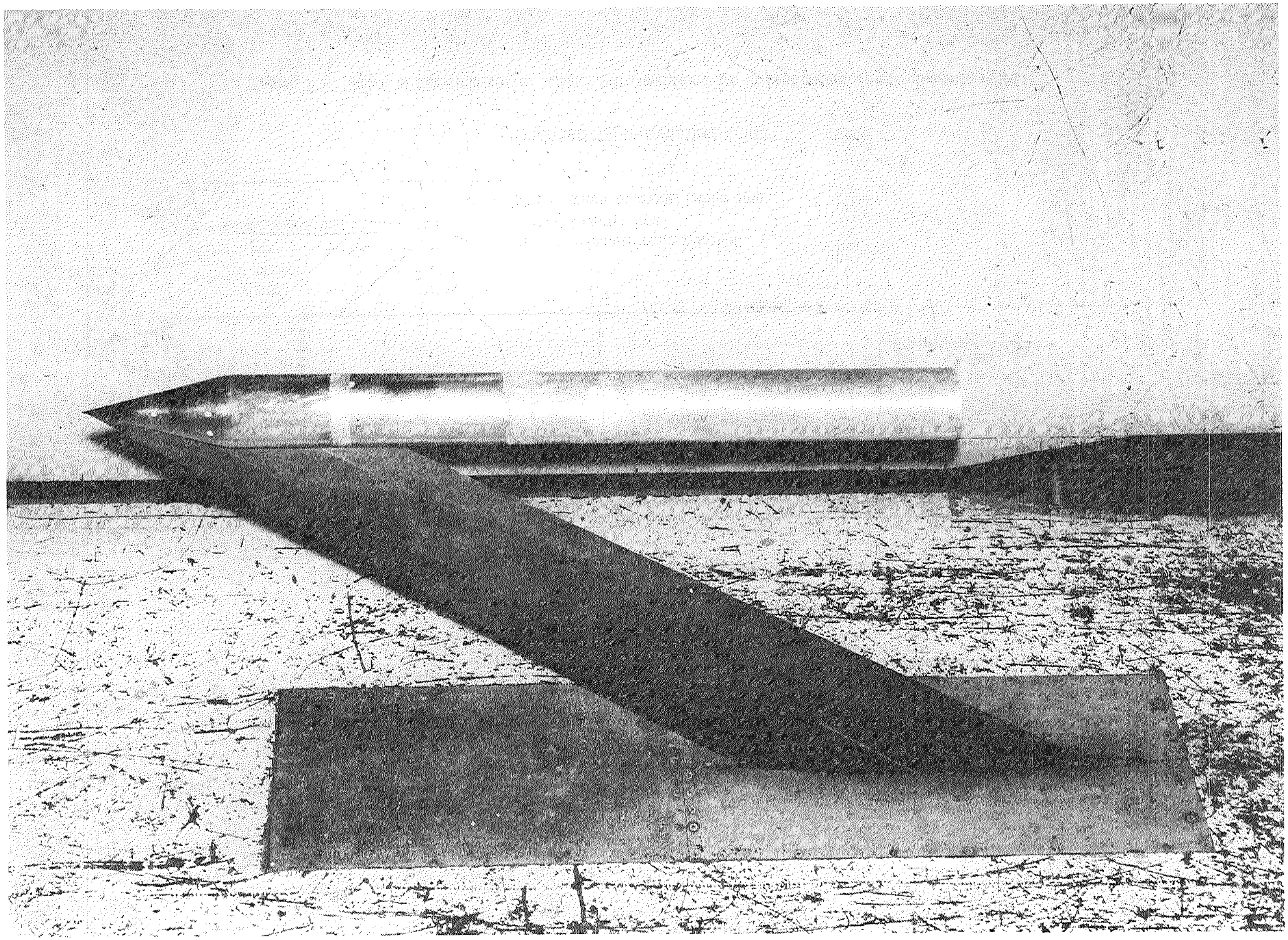

Figure 33.- Photograph of strut-mounted extended body.

L-67-3057

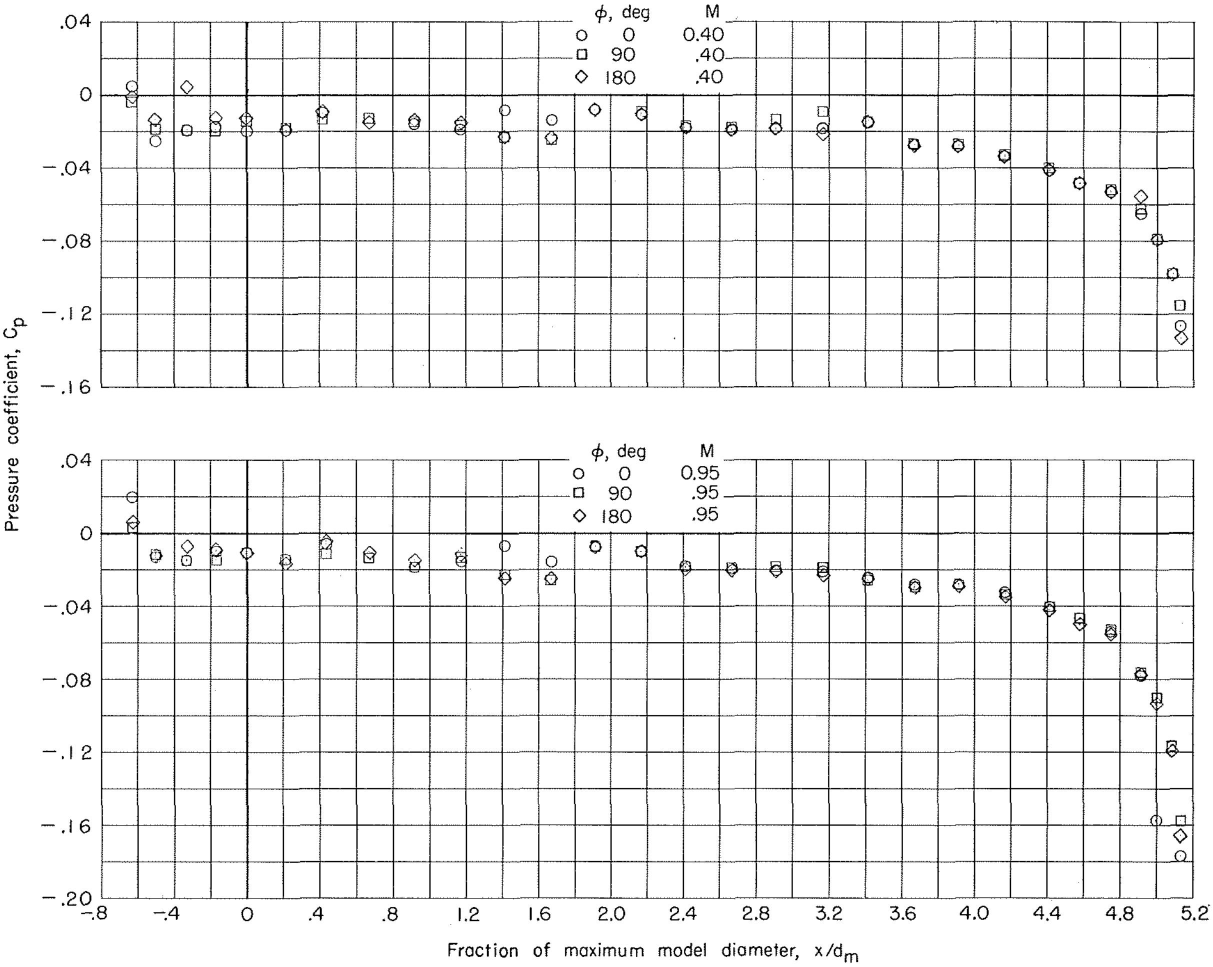

Figure 34.- Pressure-coefficient distributions on strut-mounted extended afterbody at various free-stream Mach numbers.

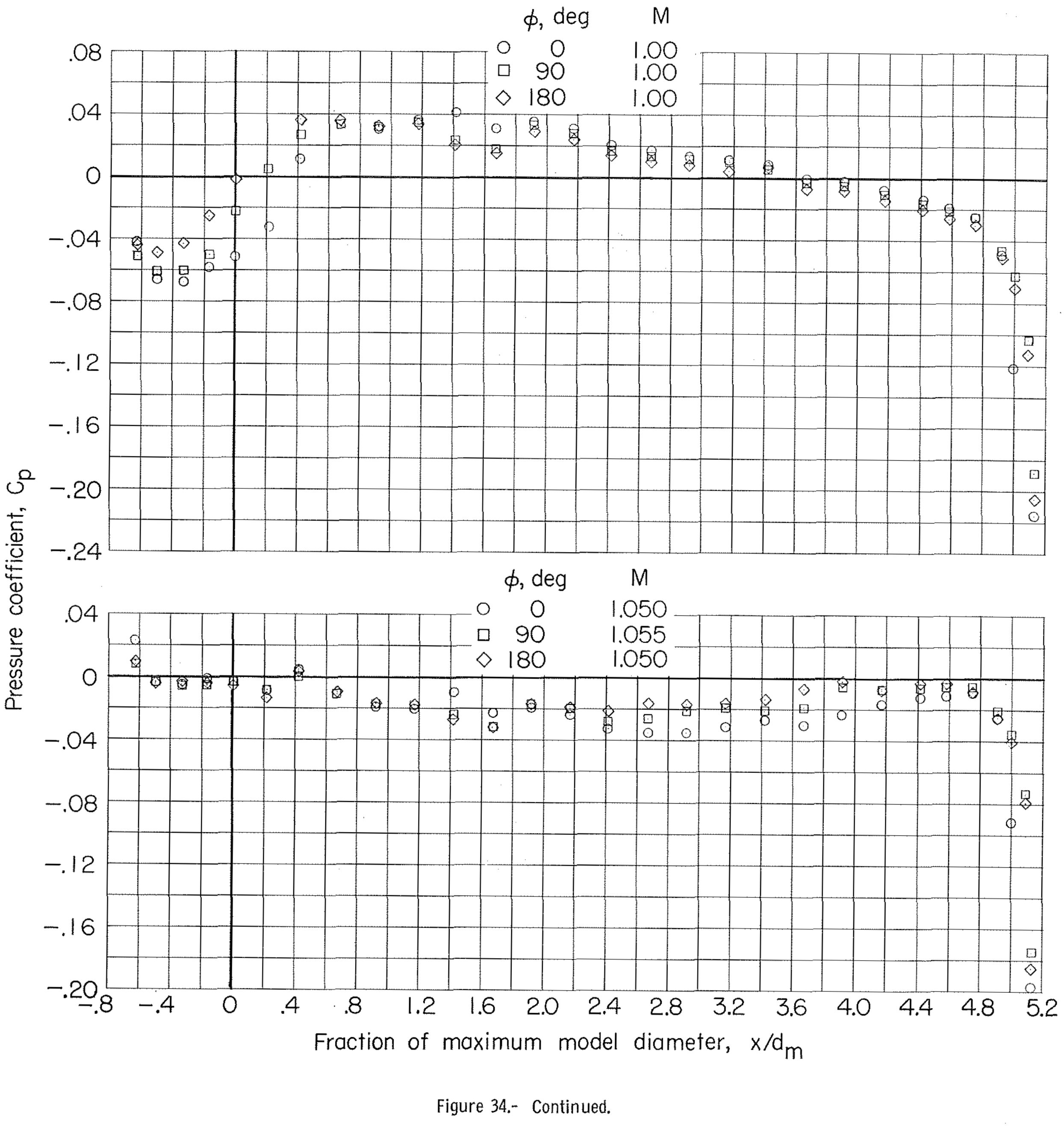

Figure 34.- Continued.

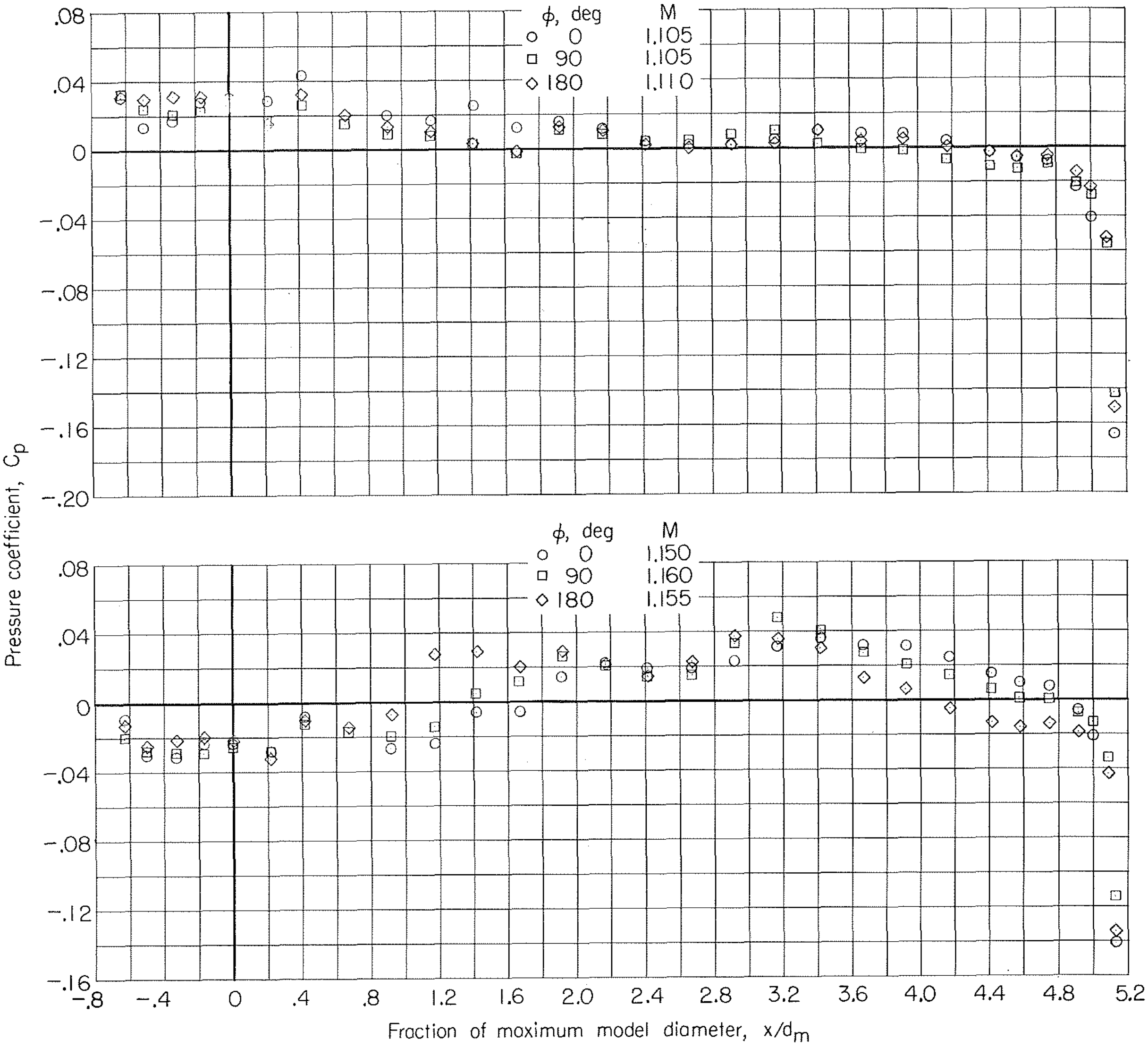

Figure 34.- Continued.

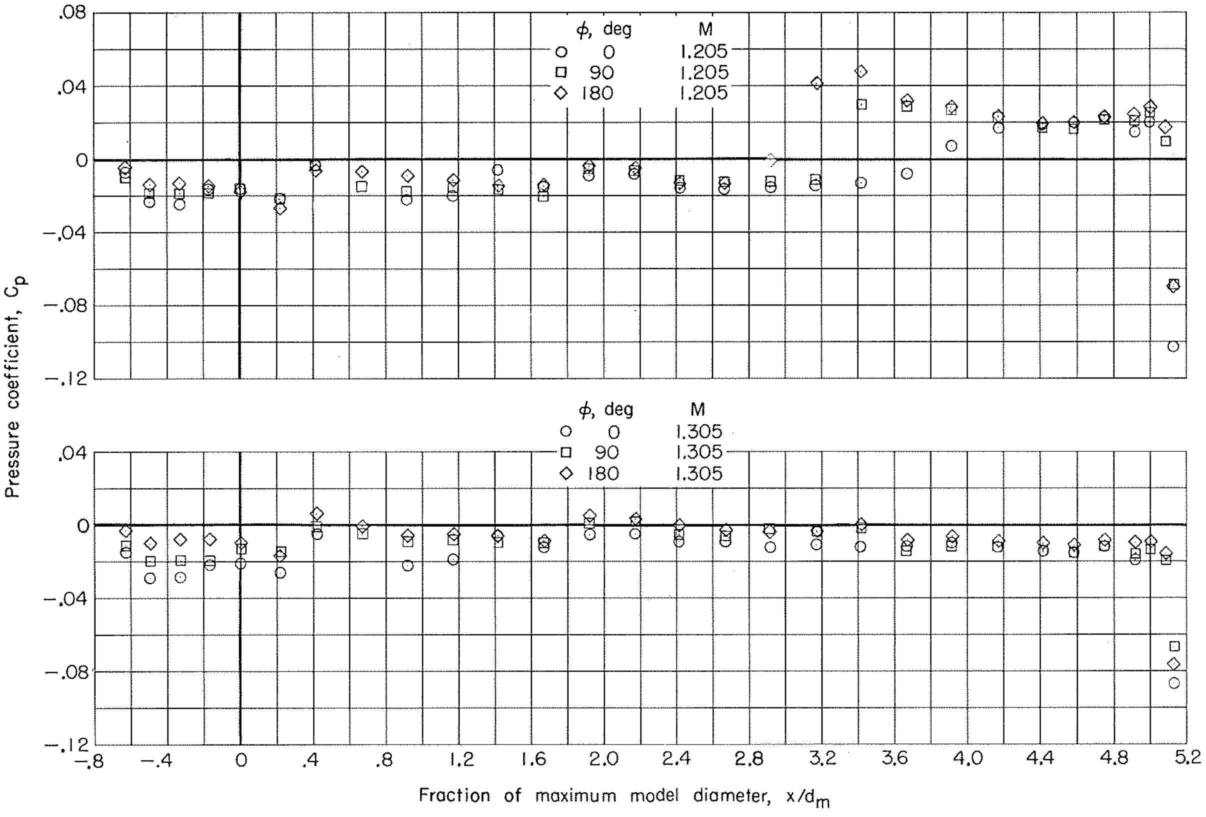

Figure 34.- Concluded.

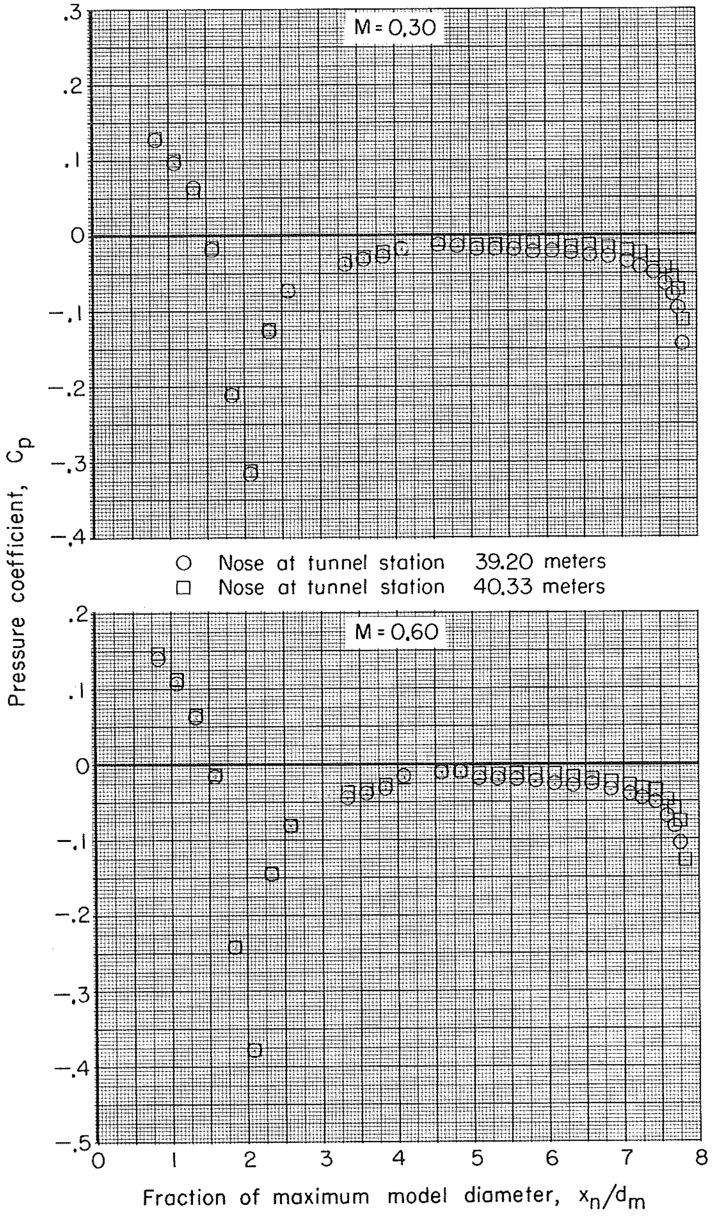

Figure 35.- Average-pressure-coefficient distributions on sting-mounted model at two axial locations.

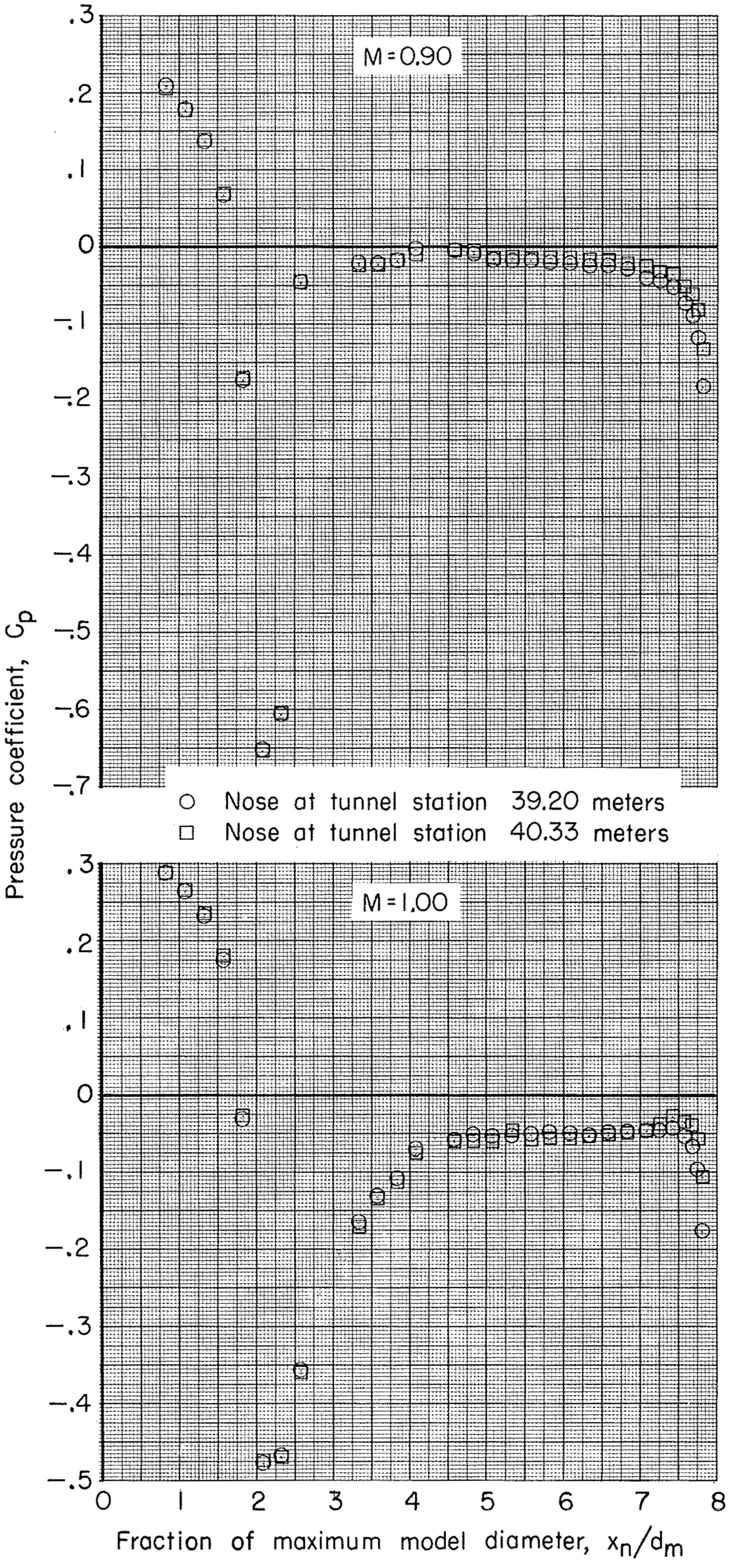

Figure 35.- Concluded.

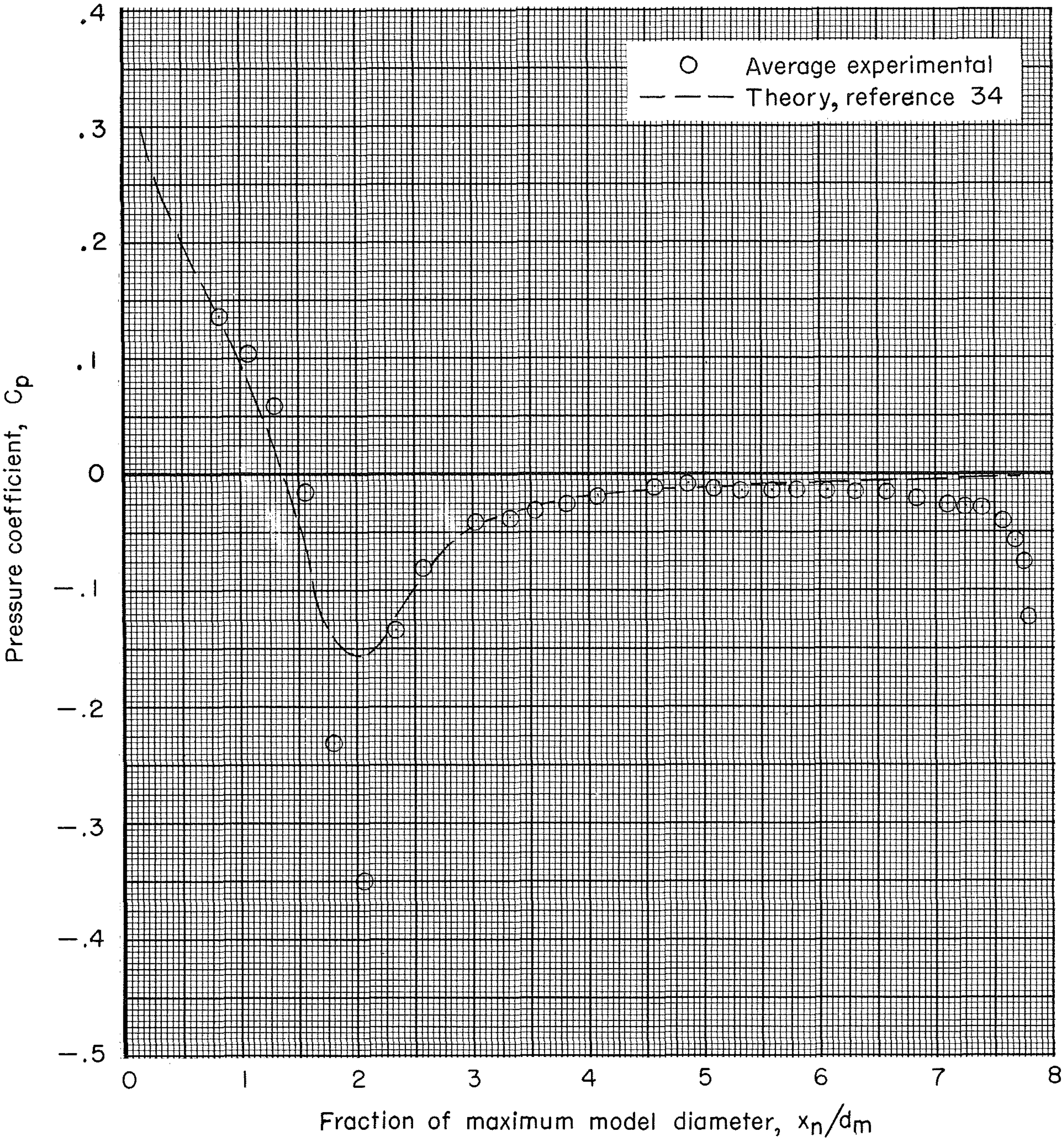

Figure 36.- Comparison of experimental pressure-coefficient distribution on sting-mounted model (nose at tunnel station 40.33 meters) with slender-body theory. $M = 0.50$.

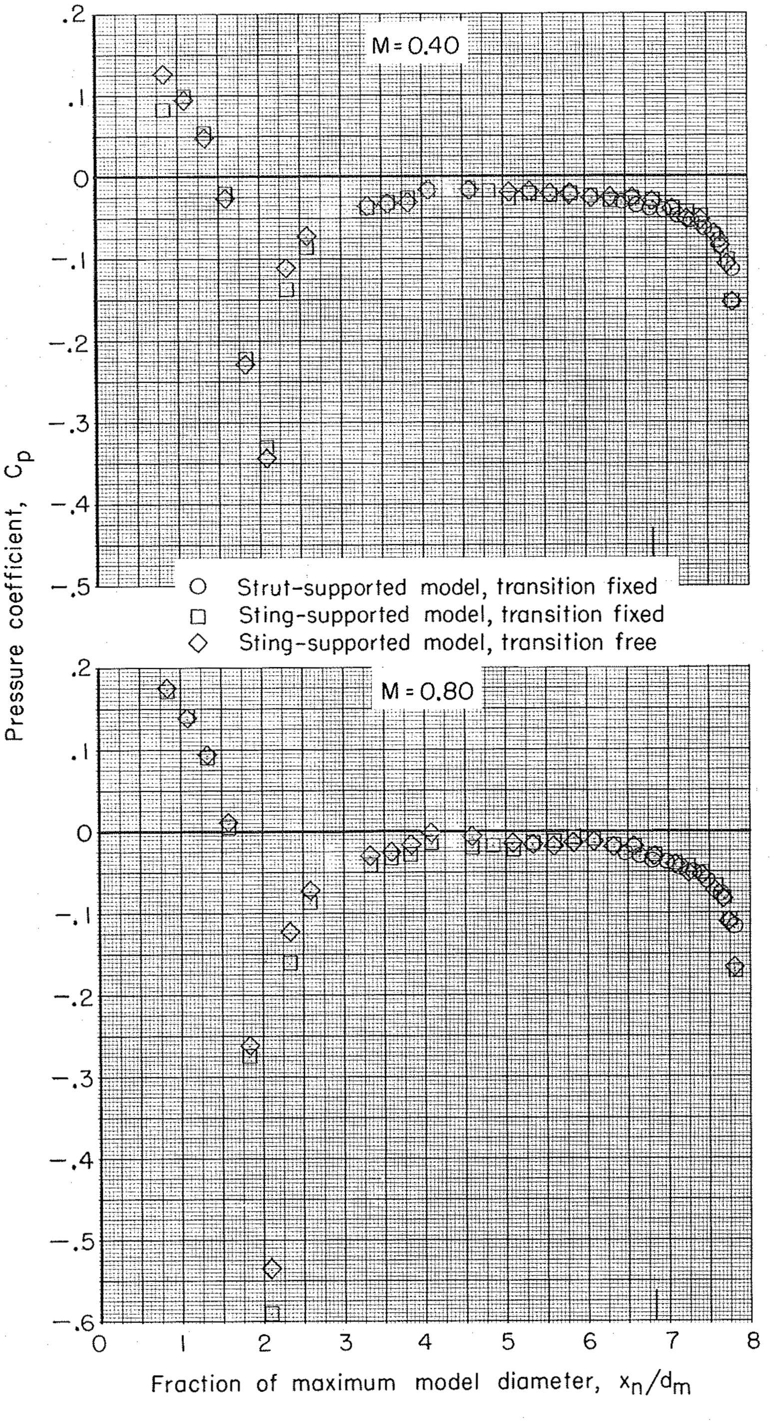

Figure 37.- Pressure-coefficient distributions on strut-mounted and sting-mounted models with noses at tunnel station 39.2 meters. $\phi = 0^o$. (Tick indicates model station 104.14.)

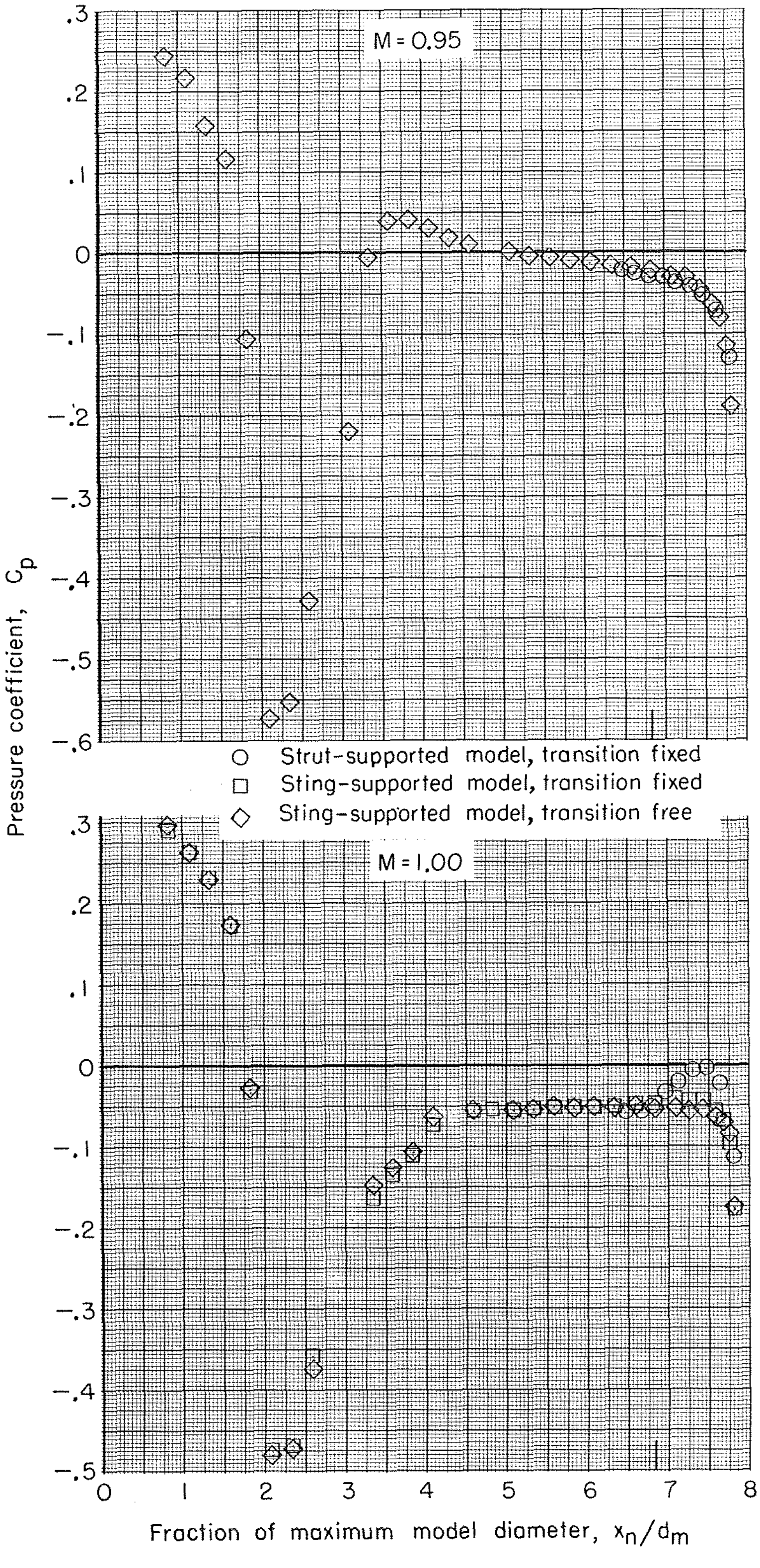

Figure 37.- Continued.

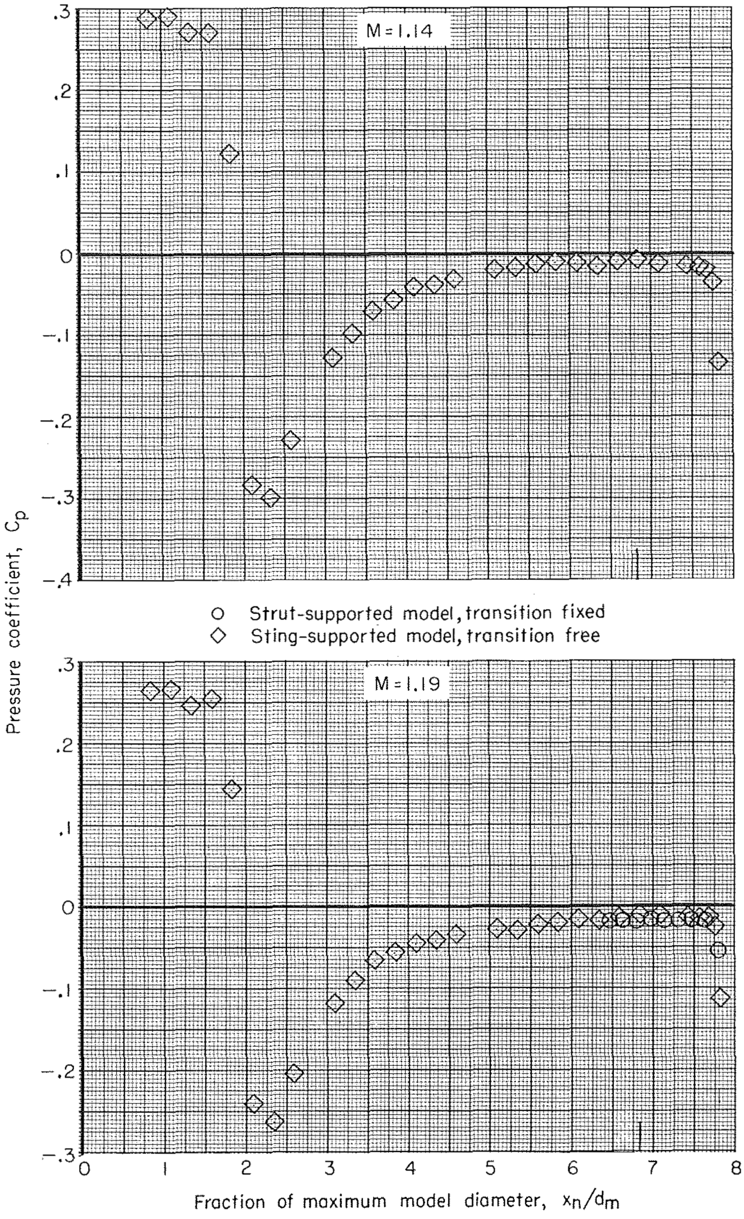

Figure 37.- Continued.